UNIVERSITÀ DEGLI STUDI DI MILANO
FACOLTÀ DI SCIENZE MATEMATICHE, FISICHE E NATURALI
DOTTORATO DI RICERCA IN FISICA, ASTROFISICA E FISICA APPLICATA

Laser system for Positronium excitation to Rydberg levels for Aegis experiment

Settore Scientifico disciplinare FIS/03

Coordinatore:
Prof. Marco R. F. **Bersanelli**
Tutor:
Dr. Fabrizio **Castelli**

Tesi di Dottorato di:
Fabio **Villa**
R08379
XXIV ciclo

Anno accademico 2010/2011

Contents

List of Figures

List of Tables

Chapter 1

An overview on Aegis antimatter experiment

A new generation of antimatter experiments has been opened after the first experiments of antihydrogen ($\bar{H}$) production in laboratory conditions at the CERN laboratory [1] and at Fermilab [2]. These experiments demonstrated the possibility of $\bar{H}$ synthesis, but produced hot $\bar{H}$ in small quantities not suited to precision studies. Therefore a program is underway at CERN to construct a facility dedicated to low energy $\bar{p}$ and $\bar{H}$ experiments.
After the first production of cold $\bar{H}$ by the ATHENA [3] and ATRAP [4] collaborations, second generation experiments are being performed for measuring the fundamental properties of this antiatom. Those experiments are AEGIS [5], ALPHA [6], ACE [7], ATRAP [4], ASACUSA [8]. My thesis's work is a part of the Aegis experiment.
Some fundamental questions of modern physics relevant to unification of gravity with the other fundamental interactions, models involving vector and scalar gravitons, matter-antimatter symmetry can be enlightened via experiments with antimatter [9]. A quantum theory of gravitation necessarily constitutes a departure from the Einstein view of gravity as a geometric phenomenon and could potentially constitute a violation of the Weak Equivalence Principle, that states that the trajectory of any falling test particles will be the same in a gravitational field, depending only on positions and velocities of the bodies and not on their internal composition. This principle is a foundation of General Relativity and a large experimental effort is placed in testing its consequences in all possible fields: this research activity includes tests about the equality of the inertial and gravitational mass, the universality of the free fall, the search for non Newtonian corrections to the gravitational law, the measurement of the gravitational red shift, the search for time variation of the fundamental constants. At present the best sensi-

tivity experiments done on Weak Equivalence Principle for ordinary matter came from state-of-the-art rotating torsion balances [10] and from tests of Moon and Earth acceleration in Solar System [11], that have a sensitivity in the range of 10^{-13}.
There are no direct measurements about the validity of the principle of equivalence for antimatter; the validity of the equivalence principle for antimatter is extrapolated from the matter results or it is inferred using indirect arguments. Particularly interesting is that some quantum gravity models leave room for possible violations of the equivalence principle for antimatter [12, 13]. Modern theories of gravity that attempt to unify gravity with the other forces of nature allow that, at least in principle, antimatter may fall differently from normal matter in the Earth's gravitational field. Specifically, as pointed out by Sherk [13], theories of supergravity guide to the possibility of a gravitational interaction which may lead to different couplings for matter and antimatter.
The recent production of copious amounts of cold antihydrogen $\bar{H}$ at CERN's Antiproton Decelerator (AD) [14, 15] has paved the way for high-precision gravity experiments with neutral antimatter. In this context, Aegis experiment proposal points directly to gravity acceleration measurement and towards spectroscopy studies on $\bar{H}$. In the first phase of the experiment, acceleration of $\bar{H}$ atoms in a controlled way by an electric field gradient (Stark effect) and subsequent measurement of free fall in a Moiré deflectometer will allow a test of the weak equivalence principle. In a second phase, the antihydrogen will be slowed, confined and laser-cooled to perform CPT studies and detailed spectroscopy. The experiment is now installing its apparatus at CERN. Figure 1.1 shows a schematic drawing of the basic experimental setup that should reach an accuracy of 1% in the measurement of the matter-antimatter gravitational acceleration. The experiment is designed to allow higher precision measurements through trapping and cooling of the antiproton ($\bar{p}$) beam [3].

1.1 The AEGIS experiment scheme

The essential steps leading to the production of antihydrogen ($\bar{H}$) and the measurement of its gravitational interaction in AEgIS with the use of CERN cold $\bar{p}$ are the following [16]:

- accumulation of positrons (e^+), from a radioactive ^{22}Na source, in a Surko-type source and trap;
- capture and accumulation of $\bar{p}$ from the AD in a cylindrical Penning

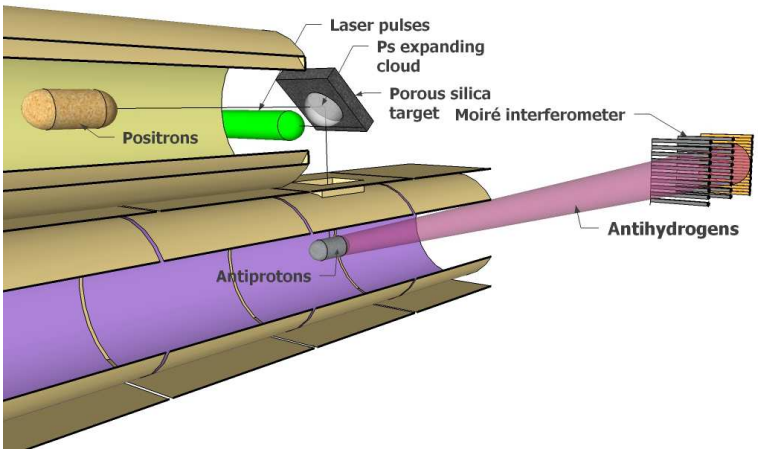

Figure 1.1: This is a scheme of Aegis apparatus.

trap;

- cooling of the $\bar{p}$ cloud to sub-K temperatures;
- production of cold positronium (Ps) by bombardment of a cryogenic nanoporous material with an intense e^+ pulse;
- two-steps laser excitation of Ps to a Rydberg state (Ps^*) with high principal quantum number;
- pulsed formation of cold Rydberg antihydrogen $\bar{H}^*$ by means of the resonant charge exchange interaction between Rydberg positronium and cold antiprotons with a residual electron: $Ps^* + \bar{p} \rightarrow \bar{H}^* + e^-$
- formation of a bunched $\bar{H}^*$ pulse by Stark acceleration with inhomogeneous electric fields;
- determination of g by two-grating Moiré deflectometer coupled with a position-sensitive detector.

I'll focalize in particular on positronium formation, excitation and the charge-exchange reaction, that are the reference frame in which my thesis work, devoted to the excitation laser system and the physics involved, is inserted.

1.1.1 Positronium formation

There are several models of Ps formation in different materials, which were reviewed in ref. [17]. Ground state Ps is formed for 75% as ortho-Ps (spin 1)

and for 25% as para-Ps (spin 0). Para-Ps annihilates in two γ rays with 511 keV each and ortho-Ps in vacuum is required to annihilate into three γ rays at least, with a maximum energy of 511 keV each and with a total energy of 1022 keV ($2m_0c^2$). We are interested only in Ps emitted by the converter as ortho-Ps with a characteristic lifetime in vacuum of 142 ns, since the lifetime of para-Ps is too short (125 ps) to allow the necessary laser excitation before annihilation. The ortho-Ps lifetime can be shortened by collisional pick-off annihilation and ortho-para conversion (both processes lead to annihilation in two gamma rays) in ranges typically from a fraction of nanosecond to tens of nanoseconds.

The presence of a superimposed magnetic field mixes the two substates of Ps with m = 0, the levels with m = 1 remaining unaltered due to Zeeman effect [18]. This leads to annihilation in two gamma rays of the m = 0 ortho-Ps state; the effect is normally called ortho-Ps *magnetic quenching*, since the lifetime of m = 0 ortho-Ps is decreased (quenched) by the magnetic field [19]. In our experiment the region of the Ps converter (Fig. 1.1) will be into a magnetic field of 1 T, thus leading to a 50% theoretical maximum efficiency in Ps generation, due to the annihilation of m=0 states.

A strategy to obtain Ps in vacuum is using porous materials with pores open to the surface. Porous materials are necessary not only to have a high yield of Ps atoms, but also to cool Ps through collisions with the inner walls of the pores. Ps atoms are emitted from the pore walls with high kinetic energy (1-2 eV). Low Ps kinetic energies are highly desirable for AEgIS. The velocity distribution of the Ps atoms coming out of the target should be the order of 10^4 m/s to allow Ps laser excitation to a Rydberg state (Ps^*) and for efficient $\bar{H}$ formation, which requires that the relative velocity of antiprotons and Ps^* must be not higher than the classical orbital velocity of the positron in the Rydberg Ps atom. Efficient formation of cooled Ps atoms is a fundamental requisite for the production of antihydrogen. The thermalization of Ps atoms is possible by means of hundreds of thousands of collisions with the walls of the pores. The collisions between Ps and the internal surface of the pores involve weak coupling to phonons or other surface modes. Ps formation and cooling has been extensively discussed in ref. [20]. A careful choice of the materials used to convert bare positrons in Ps atoms is required to provide the appropriate morphology for efficient cooling [21].

The AEgGIS experiment will be performed at cryogenic temperatures (100 mK). The low temperature of the sample contributes to Ps thermalization [22, 23]. As pointed out in ref [21], in silica-based materials the high Ps production does not depend on temperature. A similar result was found in silica films (ref. [23]). A negative aspect of the cryogenic environment is the formation of ice at the surface of the pores, as well in ultra high vacuum

condition [24]. An ice cap could avoid the Ps escape in the free space outside the target.

1.1.2 Positronium excitation

Antihydrogen production by charge exchange reaction between Ps atoms and antiprotons is the main process considered for antimatter production in AEgIS. Since the cross section for this reaction depends roughly on n^4 [25], an efficient excitation system has been developed to pump Ps atoms up to high-n levels (Rydberg levels). A cloud of Ps atoms will be produced by positrons hitting a porous silica target in a relatively strong uniform magnetic field (1 T). The experimental strategy involves exciting Ps into Rydberg states in two steps, one from $n = 1$ to $n = 3$, which involves radiation at 205 nm, and a second one from $n = 3$ to $n = 20-30$, involving radiation in the range from 1600 nm to 1700 nm. The theoretical framework as well as the experimental realization of the laser system are the core of this thesis and will be described in the subsequent chapters. The main features of this two-step excitation are the significant Doppler effect for the first transition and the modifications on the high-n sublevel structure due to Zeeman and motional Stark effects (described in sec. 3) The whole laser system is projected to be pumped whit a 650 mJ Q-switched Nd:YAG laser delivering a 4 ns pulse. The laser pulses needed by Ps excitation are produced through second-order polarization in optical crystals (whose functioning is described in sec. 2.1.2). The 205 nm radiation for the first transition is obtained by summing in a nonlinear BBO crystal the 266 nm fourth-harmonic of the 1064 nm Nd:YAG pulse and the 894 nm radiation generated in an optical parametric generator (OPG) by down-conversion of the second harmonic of the same laser (described in sec. 2.4). The other wavelength (around 1670 nm) is generated in a single step by an OPG starting from the same pump laser and then amplified by an optical parametric amplifier (OPA) system. (described in sec. 2.3) The optical transport line from laser table to the positronium atoms is presented in sec. 2.5.

1.1.3 Antihydrogen beam formation

Ps atoms emitted from the porous insulator material are excited to Rydberg states. They then traverse a Penning trap region in which about $10^5 \bar{p}$ have been accumulated, stored and cooled. The low temperature requirement on the antiprotons comes from the requirement that the antihydrogen atoms that will be formed must have a velocity very smaller compared to the velocity of several 100 m/s that they will achieve after acceleration. To reach such

a low temperature, the Penning trap is joined to a 50 mK dilution refrigerator, and the antiprotons are coupled to the low temperature environment by embedding them in an electron plasma. The latter will cool down through synchrotron radiation, as well as through a tuned circuit; furthermore, evaporative cooling of the pre-cooled antiprotons is being envisaged.
The charge exchange cross-section with excited Ps is very large about ($10^5 nm^2$ for n = 35) and reaches a maximum when the positrons and antiprotons relative velocities are matched. Taking into account the corresponding kinetic energy, as well as a smaller contribution due to converted internal energy, $\bar{H}$ will be created at velocities of 25-80 m/s. The neutral atoms are not sensitive (to first order) to constant electric fields, they do experience a force when their electric dipole moment is exposed to an electric-field gradient. Since the dipole moment scales approximately with the square of the principal quantum number, Rydberg atoms are especially amenable to being manipulated in this way [17]. Such so-called *Stark acceleration* (and deceleration) has been successfully demonstrated, among others, by one of the AEgIS groups with (ordinary) hydrogen after excitation to the $n = 22$, 23, 24 states [26]. We intend to use a similar field configuration, generated by axially split electrodes within the cylindrical geometry of a Penning trap, to accelerate the formed $\bar{H}$ atoms to some hundreds m/s in the direction of the deflectometer apparatus.

1.1.4 Gravity measurement

Consider a beam of antihydrogen which falls freely in the Earth's gravitational field. Given AEgIS realistic numbers, flight path length of 1 m, horizontal velocity of about 500 m/s, the vertical displacement of an antihydrogen atom due to gravity, assuming $g = 10\ m/s^2$, would be about 20 μm. However, the formed antihydrogen beam has a thermal velocity in all directions of a few tens of m/s (corresponding to the 100 mK at which the $\bar{H}$ production will take place). In other words, the beam has a large radial divergence. During the flight path, an antihydrogen atom can thus displace vertically up to 10 cm, and it is not possible, for each antiatom, to know its radial velocity. On top of that, the vertical position of the antihydrogens when leaving the Stark acceleration region is known with a precision of 1 mm. It is therefore clear that it is impossible to measure the gravitational acceleration g by simply measuring the vertical displacement.
The solution to such problem resides in the so called Moiré deflectometer that has been successfully used to measure the gravitational acceleration g with a beam of argon atoms [27]. This apparatus is purely classical, since it is based on geometric propagation of an (anti)atomic beam through a set of

identical gratings. In its original form it consisted of three material gratings, equally spaced and aligned parallel to each other, while in the AEgIS configuration the last grating is replaced by a position sensitive $\bar{H}$ annihilation detector. The first two gratings select propagation directions of an originally diverging atomic beam. Beyond such gratings the atoms are distributed in a shadow image forming sets of fringes at various distances from the second grating, multiples of the distance between the first two gratings. This device is non-dispersive, in the sense that atoms with a broad energy distribution and without collimation can be used. If the atomic beam is in accelerated motion, as in a gravitational field, a fringe shift of the shadow image equal to $d = -gT^2$ will be induced, where T is the time of flight between two adjacent gratings. This time can be calculated since both the starting time (Stark acceleration) and the stopping time (annihilation) are known with a precision much smaller than the typical time of flight of few ms. Since our beam will not be monochromatic, this time of flight is not constant but will be characterized by a given distribution. Nevertheless the antihydrogens can be grouped in bins of different velocities, and the corresponding d can be measured. A parabolic fit to d as a function of the averaged time of flight T^2 in each bin with a function of the type $d_0 + gT^2$, can deliver the measure of the acceleration constant g; the parameter d_0, which value is provided by the fit itself, accounts for possible geometrical misalignment between the gratings. We expect to achieve a precision of about 1% on g measurement [16].

Chapter 2

Design and experimental test of the laser system

2.1 Introduction

The detailed theory of Ps excitation to Rydberg states is presented in Refs. [28, 29, 30] and the theoretical studies we have done are reported in sec. 3; here we report the results relevant to the laser system discussion. The Ps excitation is performed by a two step transition: a resonant one from $n = 1$ to $n = 3$ and a near resonant one from $n = 3$ to high–n(fig. 2.1). The $1 \rightarrow 3$

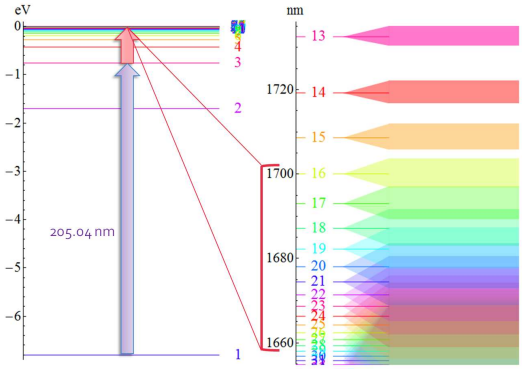

Figure 2.1: Schematic representation of the laser excitation to the Rydberg levels. On the left are plotted the unperturbed positronium levels as a function of the level energy, on the right are plotted the Rydberg levels with a qualitative width (equal to eq. 3.12). The goal levels are marked with a red bracket.

transition is characterized by the Doppler width, while the width of the $3 \rightarrow$ high-n transition is actually dominated by the motional Stark effect. The

Ps cloud, emerging nearly isotropically from the silica target (see Fig. 1.1), is assumed thermalized [31] with a theoretical Doppler broadening around $4.4 \cdot 10^{-2}$ nm FWHM for the first transition at the reference temperature of 100 K. However, the Ps atoms which are useful for $\bar{H}$ synthesis by charge exchange reaction, and therefore targets for laser excitation, are only those crossing the antiproton bunch in their fly. The trajectories of this group of atoms lie within the angular cone starting from the generating point and ending at the cigar-like shape antiproton cloud and theirs velocities are near perpendicular to laser propagation, thus reducing the Doppler broadening needed to be covered by the laser pulses; the line broadening of the first transition relative to these Ps atoms is estimated to be $\Delta\lambda_D = 4.5 \cdot 10^{-3}$ nm (32 GHz at 205 nm wavelength) [30]. We define the saturation fluence F_{sat} for laser pulse incoherent excitation in the frame of a closed two-level rate equations model. For this two levels system the excited population as a function of the laser fluence F is $\frac{1}{2}(1 - e^{-2F/F_{sat}})$ [28] and when the fluence F reaches the value F_{sat} we have 43% of the population on the excited level. For the first transition F_{sat} comes out to be

$$F_{sat}(1 \to 3) \simeq \frac{c^2}{B_{1\to 3}} \sqrt{\frac{2\,\pi^3}{\ln 2}} \cdot \frac{\Delta\lambda_D}{\lambda_{13}^2} \simeq 11\,\mu\mathrm{J/cm}^2 \tag{2.1}$$

where $B_{1\to 3}(\omega)$ is the absorption Einstein coefficient appropriate to the dipole–allowed transition. This equation gives the minimum pulse fluence needed for reaching saturation of the transition. The energy of the exciting laser pulse will depend on the laser spot-size, which must overlap the Ps cloud. The transverse pulse FWHM dimension of the laser, assuming a Gaussian profile for simplicity, is requested to be $\Phi = 3$ mm (according to the Ps cloud cross-section of 6 mm^2 of AEgIS proposal). In order to cover the whole FWHM of the cloud with a fluence higher or at least equal to the saturation value F_{sat}, the fluence F_0 at the intensity maximum is fixed to $F_0 = 2F_{sat}$; the laser pulse energy ($E = \pi(F_0/2)(\Phi/1.177)^2$ for a Gaussian transverse profile) then comes out to be $E_{13} = 2.2\,\mu$J. In relation to the second transition $n = 3 \to$ high–n, the motional Stark effect on Ps atoms at 100 K temperature and 1 Tesla magnetic field leads to the opening and mixing up of the originally near degenerate l, m sublevels belonging to a definite n and, moreover, to an interleaving of different sublevel manifolds for n equal to 16. The broadening of the sublevel structure, which can be considered as a quasi-continuum due to their huge number (a Rydberg level band), can be as high as 10 nm ($\sim$1 THz), overwhelming larger than the Doppler broadening of 0.4 nm. In the full mixing range $n > 16$ [32], the saturation fluence for the second transition results largely independent of n and of the laser linewidth and comes

out to be

$$F_{sat}(3 \to n) \simeq \frac{c \times 13.6\,\mathrm{eV}}{B_{3\to n}\,\hbar\, n^3} \simeq 0.98\,\mathrm{mJ/cm^2} \tag{2.2}$$

for the reference $n = 25$. The linewidth of the laser pulse can be chosen in the range of 1 to 4 nm, greater than the Doppler broadening and limited by the requirement of exciting a number of final n states sufficiently low. The total energy of the laser pulse required for saturating this Rydberg level, using the same cloud parameters of the previous transition, results in $E_{3n} = 174\ \mu$J.

2.1.1 Laser system scheme

The wavelengths of the two lasers are respectively $\lambda = 205.04$ nm for the excitation from ground to $n = 3$ state, and λ in the range [1650, 1700] nm for the in-cascade transition. The two lasers have to generate the wide spectral bandwidth matching the quasi-continuum level bandwidths of the two

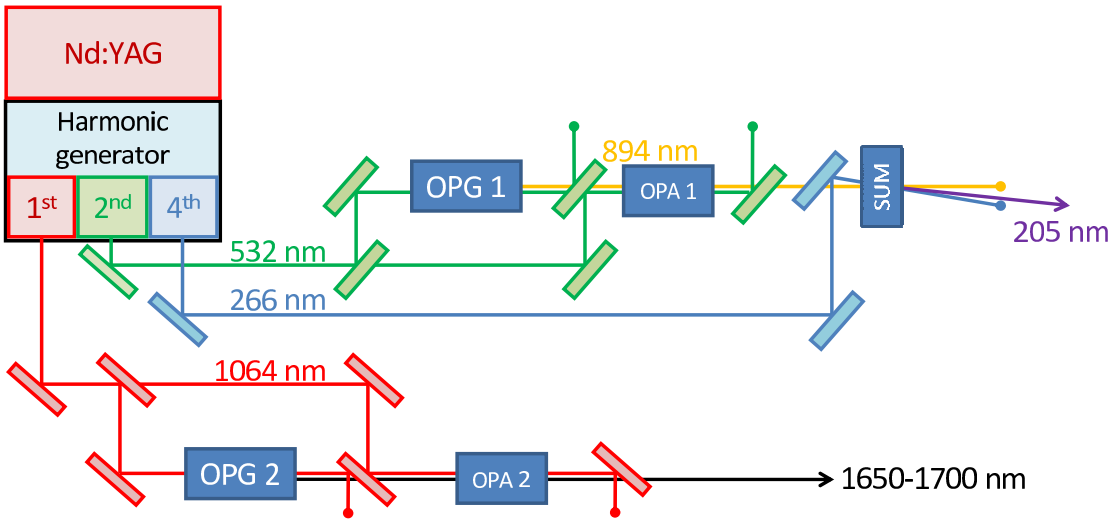

Figure 2.2: Schematic representation of the laser system for the Rydberg excitation of Ps

continuum spectrum necessary for efficient excitation, an essential goal in Aegis experiment, is that based on the optical parametric generation and amplification [33]. We consider the laser system schematized in Fig. 2.2. Both radiations are generated through second-order polarization in optical

crystals. The 205 nm radiation is obtained by summing up in a non-linear BBO crystal the 266 nm fourth-harmonic of the 1064 nm Nd:YAG radiation and the 894 nm radiation generated in an OPG (Optical Parametric Generator). This radiation is produced by means of a down conversion process from the 532 nm second-harmonic of the Nd:YAG, and further amplified with an OPA (Optical Parametric Amplifier), in order to fulfill the requirements about the acceptance region of the BBO crystal for greater energy production. The other wavelength is generated more directly in a single step by an OPG, and then amplified by an OPA. In this layout a Q-switched Nd:YAG laser delivering a maximum of 650 mJ in $4 \sim 6$ ns drives both laser systems. About half the energy of the Nd:YAG laser is conveyed along the first system (the upper part of Fig. 2.2), where it is frequency doubled to the 532 nm second harmonic for pumping the OPG1, the OPA1 and a second frequency doubling crystal producing the 266 nm radiation. The remainder of the 1064 nm radiation pumps both the OPG2 (a small fraction) and the OPA2. The laser system provides spectral bandwidths large enough to cover the Ps level broadenings as well as the power levels to meet the requirements as discussed before. The laser of the second transition has in addition the capability to operate at frequencies within $\sim$ 30 nm around the 1670 nm. This allows the selection of the final Ps excited energy (starting from $n = 16$ up to the ionization limit) and gives margin for possible unexpected problems in the excitation. The pulse duration cannot exceed a few nanoseconds in order to be consistent with the Ps flight time from the silica slab to the $\bar{p}$ cloud and, moreover, to minimize losses due to enhanced annihilation after spontaneous decay to the ground state due to sublevel magnetic mixing. The pulse energies and spectral bandwidth can satisfy the requirements for maximization of the Ps transition efficiency. We have the goal of generating pulses with an energy at ten times higher than the energy estimated by saturation fluence calculations, for having a large safety margin on the amount of energy at disposal.

2.1.2 Nonlinear optics

In order to make pulses with required wavelengths, we chose to use non linear optics to convert the laser pump at 1064 nm in its harmonics and to parametrically generate and amplify the remaining wavelengths cited in the previously subsection. Nonlinear optics is a well known effect [34].

Parametric nonlinear optical phenomena can be described by a Taylor series expansion of the dielectric Polarization density (dipole moment per

unit volume) P in terms of the electrical field E:

$$\begin{aligned} P_i &= \epsilon_0(\chi^{(1)}_{i,j}E_j + \chi^{(2)}_{i,j,k}E_j(t)E_k(t) + \chi^{(3)}_{i,j,k,l}E_j(t)E_k(t)E_l(t) + ...) \\ &= \epsilon_0\chi^{(1)}_{i,j}E_j + P_{i,NL} \end{aligned} \tag{2.3}$$

Here, the coefficients $\chi^{(n)}$ are the n-th order susceptibilities of the medium and the presence of such a term is generally referred to as an n-th order nonlinearity. In general $\chi^{(n)}$ is an n+1 order tensor representing both the polarization dependent nature of the parametric interaction as well as the symmetries (or lack thereof) of the nonlinear material. Linear effects in the electric field of 2.3 include refraction and absorption while nonlinear effect are used to generate the harmonics of the pump, to parametrically generation of wavelengths and to amplify these wavelengths . All these processes the second order of the electric field and was implemented for the realization of the laser system.
Considering the displacement field $D = \epsilon_0 E + P = \epsilon E + P_{NL}$ where $\epsilon = \epsilon_0(1 + \chi^{(1)})$, we can write the inhomogeneous Maxwell equation:

$$\nabla^2\vec{E}(\vec{x},t) - \epsilon\mu\frac{\partial^2\vec{E}(\vec{x},t)}{\partial t^2} = \mu\frac{\partial^2\vec{P_{NL}}(\vec{x},t)}{\partial t^2} \tag{2.4}$$

which describes wave propagation in a source-free, nonlinear medium of linear permittivity ϵ and permeability μ. For optically transparent media, $\mu \approx \mu_0$, where μ_0 is permeability of the vacuum. The nonlinear polarization term on the right-hand side of eq. 2.4 can be treated as a source term with sources distributed throughout the nonlinear medium. These sources radiate new waves which reach a given point in the medium with different phases. Because of this phase variation, the interference among the waves can lead to energy flowing back and forth among the nonlinearly generated and applied optical fields. For n optical fields of frequencies $\omega_1, \omega_2, ..., \omega_n$ entering the nonlinear medium and generating nonlinear polarization at frequency ω_{n+1}, we must solve (n+1) wave equations of the type

$$\nabla^2\vec{E}(\vec{x},t,\omega_i) - \epsilon(\omega_i)\mu\frac{\partial^2\vec{E}(\vec{x},t,\omega_i)}{\partial t^2} = \mu\frac{\partial^2\vec{P_{NL}}(\vec{x},t,\omega_i)}{\partial t^2} \tag{2.5}$$

where $\epsilon(\omega_i)$ is the linear permittivity of the medium at frequency ω_i. Considering the cases of second order nonlinearity, due to the importance on this thesis, we have a system of three equation concerning the wavelengths involved in sum frequency (for example 894 nm + 266 nm = 205 nm) or parametric generation and amplification (where the pump is separated in two

lower frequencies, as 1064 nm is decomposed in 1650 and 3000 nm pulses). Solving the system using standard approximations [34], we obtain:

$$\begin{aligned}
\frac{dE_i(z,\omega_1)}{dz} &= \frac{i\omega_1}{4cn_1}\sum_{j,k}\chi^{(2)}_{i,j,k}E^*_j(z,\omega_2)E_k(z,\omega_3)e^{i\Delta kz} \\
\frac{dE_j(z,\omega_2)}{dz} &= \frac{i\omega_2}{4cn_2}\sum_{k,i}\chi^{(2)}_{j,k,i}E_k(z,\omega_3)E^*_i(z,\omega_1)e^{i\Delta kz} \\
\frac{dE_k(z,\omega_3)}{dz} &= \frac{i\omega_3}{4cn_3}\sum_{i,j}\chi^{(2)}_{k,i,j}E_i(z,\omega_1)E_j(z,\omega_2)e^{-i\Delta kz}
\end{aligned} \tag{2.6}$$

where n_i are the linear refraction indexes of the medium and $\Delta k = k_3 - k_1 - k_2$ is the wave vector mismatch between nonlinear generated wave $E_k(z,\omega_3)$ and the nonlinear polarization $P^{(2)}_k(z,\omega_3)$ which sustain it. The term Δkz, thus, represents the phase mismatch. The nonlinear generation as a function of the phase mismatch Δk shows a maximum for $\Delta k = 0$ (called *phase matching*, that is analogue to a momentum conservation law). Since the sign of power flow from one wave to the other is determined by the relative phase between the waves, the continuous phase slip between these waves caused by their differing phase velocities leads to an alternation in the direction of the flow of power. The distance over which the relative phase of the waves changes by π is the *coherence length* $l_c = \pi/\Delta k$. It is impossible to satisfy $\Delta k = 0$ in singly refracting media [34] because of the monotonic increase in the index of refraction with frequency due to normal dispersion. However, index matching may be possible in birefringent media. In uniaxial crystals, the index of refraction experienced by the extraordinary wave polarized in the plane containing its direction of propagation and the optic axis of the crystal varies from the ordinary index n_o to the extraordinary index n_e as the direction of propagation changes from along to perpendicular to the optic axis. On the other hand, the ordinary wave polarized perpendicular to the plane of the optic axis and the direction of propagation experiences no refractive index variation. Therefore, a proper choice of the polarization directions of the waves in a birefringent medium may achieve index matching. Another way to compensate the phase mismatch Δk is *Quasi-phase matching* [35]. Quasi-phase matching is a technique for phase matching nonlinear optical interactions in which the relative phase is corrected at regular intervals using a structural periodicity built into the nonlinear medium. A particularly effective type of periodic structure is one in which the sign or magnitude of the nonlinear coefficient is modulated throughout the material. Using ferroelectric crystal it is possible to orientate the ferroelectric domains with a periodicity Λ function of the phase mismatch ($\Lambda = m(2\pi/\Delta k)$). With some

calculation [35], the quasi phase matching leads to the same conclusion of phase matching, with the difference on the value of nonlinear coefficient d: in case of quasi phase matching of the first order ($m = 1$) the resulting coefficient become $d_{eff} = 2d/\pi$ but it can be choose along any combination of wave polarization. For example, in Potassium Titanyl Phosphate (KTP) the nonlinearity used in phase matching has a value of 3.9 pm/V while the tensor element in which the polarization are the same for all the three waves, thus only employable with quasi phase matching, has a value of 15.3 pm/V, that becomes 9.7 pm/V using quasi phase matching. The limiting factor on quasi phase matching crystal are the smaller transverse area, due to the electric fields used to orientate the crystal domains, and a lower damage threshold. An useful approximation for analytical compute of 2.6 is to consider one of the waves constant over the process, this approximation is well suited for describing the processes of sum frequency and parametric amplification, when the nonlinear generated waves are small, i.e. less than 10%, of the pump wave(s). In this case, for the sum generation ($\omega_1 + \omega_2 = \omega_3$), the resulting intensity $I(\omega_3)$ become [34] (see fig 2.3):

$$I(\omega_3, z = L) = \frac{(\omega_1 + \omega_2)^2 I(\omega_1) I(\omega_2)}{2 n_1 n_2 n_3 \epsilon_0 c^3} L^2 (d^{(2)})^2 \mathrm{sinc}^2(0.5 \Delta k L) \qquad (2.7)$$

where $d^{(2)} = 0.5\chi^{(2)}$ is the effective nonlinear coefficient.

Another case used in the thesis's work is optical parametric amplification,

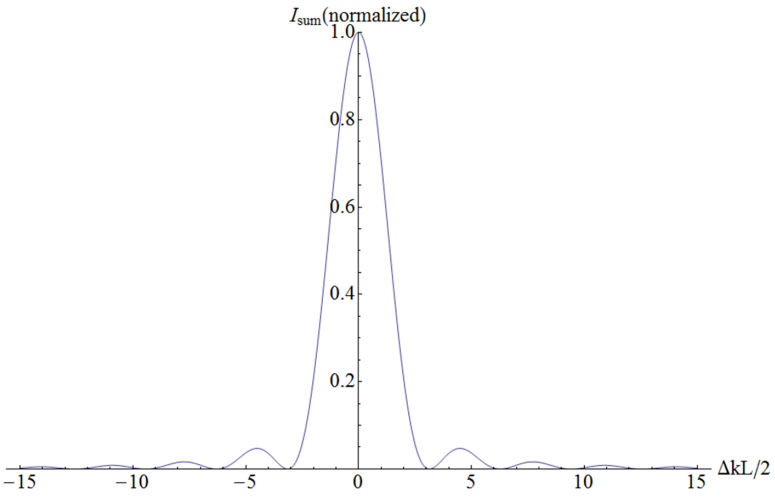

Figure 2.3: Phase matching function of sum generation process as a function of the phase mismatch Δk and crystal length L (eq. 2.7)

where a undepleted pump (ω_p) amplifies a small signal (ω_s) and, for energy conservation, generates a wave, called idler, at frequency $\omega_i = \omega_p - \omega_s$. The intensity of the signal becomes [34] (see fig 2.4):

$$I(\omega_s, z) = I(\omega_s, 0) \sinh^2 \left(\frac{z}{4c} \sqrt{\frac{\omega_p \omega_s}{n_p n_s}} \chi^{(2)}_{eff} |E(\omega_p)| \right) \tag{2.8}$$

where $|E(\omega_p)|$ is the undepleted pump field.
If the nonlinear generated field(s) intensity become comparable with pump(s)

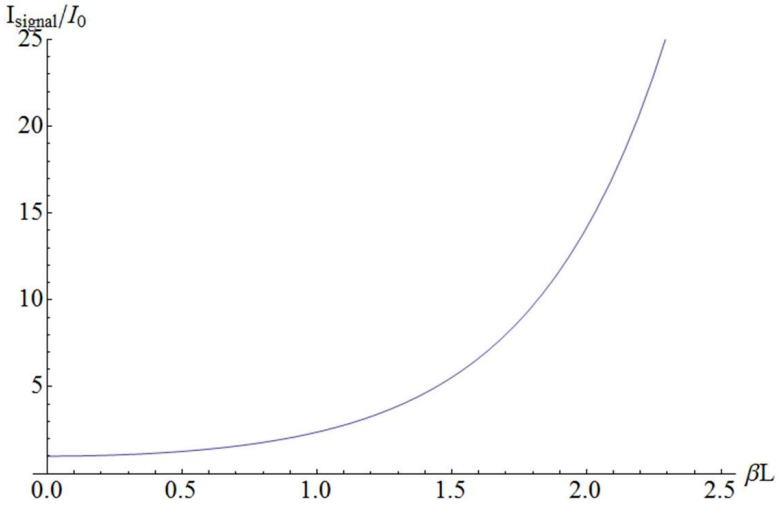

Figure 2.4: Intensity amplification as a function of crystal length $z = L$ and constants $\beta = \frac{1}{4c}\sqrt{\frac{\omega_p \omega_s}{n_p n_s}} \chi^{(2)}_{eff} |E(\omega_p)|$ for a undepleted (constant) pump intensity. (eq. 2.8)

intensity a numerical solution of 2.6 is required. We used SLNO [36] software to solve them and obtain values of phase matching angle, acceptance angle and spectrum, quasi phase matching periodicity and similar useful construction information as a function of the generated intensities in order to project the laser system and order the crystals to manufacturers.

2.2 Laser pumps

The laser system is pumped by a Q-switched Nd:YAG source. This laser is pumped by flash lamp or diodes and it emits 1064 nm wavelength with a typical spectrum up to 1 cm^{-1} and a duration of about 5-10 ns. The

pulses can be frequency doubled (532 nm), tripled (355 nm) or quadrupled (266 nm) outside the laser cavity using nonlinear crystal, in order to have new wavelengths in visible or ultraviolet range with high efficiency. From those wavelengths we can obtain new wavelengths using optical parametric generation, for example in a periodically crystal as done in sec. 2.3.1 and 2.4.1 or by sum of frequency as done in sec 2.4.3. Because of all those processes are pumped by Nd:YAG fundamental or harmonics, the pulse generated by the system strongly depend on Nd:YAG pump quality. The typical pulse has many longitudinal modes, in the order of hundreds, and a the transverse profile is characterized by a shape of concentric rings in the near field, that become near Gaussian in far field (as well as in a focused beam). The output pulse dimension, divergence and shape is strongly dependent on the actual dimension of the cavity, the curvature radius of cavity mirrors, the alignment of the optical elements inside the cavity and its quality, so if we need to change the laser pump, or modify a preexistent one, we need to check and adjust all the system components built after the source. During the thesis's work we used two laser sources, one in Florence and one in Milan. This last one has to be modified and realigned during the thesis, with the following work to refit the system previously built.

2.2.1 Florence pump

We worked in the laboratory of Chemist department of Universitá degli Studi di Firenze and in collaboration with LENS (reference person: dott. G. Ferrari). The laser pump used is a Quantel model CFR-200 GRM *Big Sky*, with repetition rate 20 Hz (fig. 2.5). It has an integrated second harmonic generator, that emits 110 mJ per pulse at 532 nm with 8 ns FWHM pulse duration and spectrum less than 2 cm^{-1}. It doesn't have an energy regulation, nor we had the possibility to externally change the pulse energy with continuity, so we used the lamp voltage to regulate the energy during measurements. Changing the laser lamp voltage has the consequence that the thermal focal length of the laser rod will slightly change, thus changing the laser output divergence. After the cavity we frequency doubled a part of the 532 nm pulse with a 6 mm long BBO (β-Barium Borate) nonlinear crystal. The typical energy output in function of the 532 nm pulse energy input is shown in fig 2.6.

2.2.2 Milan pump

We worked in the Quantum and nonlinear optics laboratory of Physics department of Universitá degli Studi di Milano (reference person: dott. S.

Figure 2.5: Laser pump used during tests in Florence

Cialdi). The Milan source is a modified Quanta System Handy YAG 101E (fig 2.7). This laser pump can emit up to 190 mJ in the fundamental 1064nm wavelength and can be externally doubled or quadrupled for 532 nm and 266 nm generation. This system was used both for the generation of 205 and 1650-1700 nm pulses, but it can't feed both simultaneously. We needed to realign it completely few times, due to the age of the pump and because we had to transfer the laser system from one room to another during the thesis. The procedure used for best alignment is described in appendix A.1.
We have studied extensively this laser source in order to gain expertise with the system as well as to improve its quality and stability, therefore improving the overall laser system effectiveness. Changing the Q-switch rate from 1 to 10 Hz, we have found that the best stability, in term of energy and dimension fluctuations, is obtained at 1 or 2 Hz, we chose 2 Hz in order to half the time needed to accumulate statistics during the alignments. For Aegis experiment this is not a critical value due to the very low rate at which antiprotons and positrons are accumulated (Aegis requires about one pulse every few hundred seconds). Another parameter useful to characterize the multimodal pulse transverse quality is the so called M^2 factor [37]. The propagation of a multimodal beam can be treated as a Gaussian beam with divergence $\theta(M)$ and waist $w_0(M)$ defined as:

$$\begin{aligned} w_0(M) &= w_0 \cdot M \\ \theta(M) &= \theta \cdot M^2 \\ w(x) &= \sqrt{w_0(M)^2 + (x - x_0)^2 \theta(M)^2} \end{aligned} \tag{2.9}$$

where w_0 and θ are respectively the waist and the divergence defined as for a Gaussian beam. Taking many transverse profiles around a waist obtained with a lens of focal $f = 300mm$, we can measure this factor fitting the FWHM of the pulse with eq. 2.9. For this pump we measured $M^2 = 1.4 \pm$

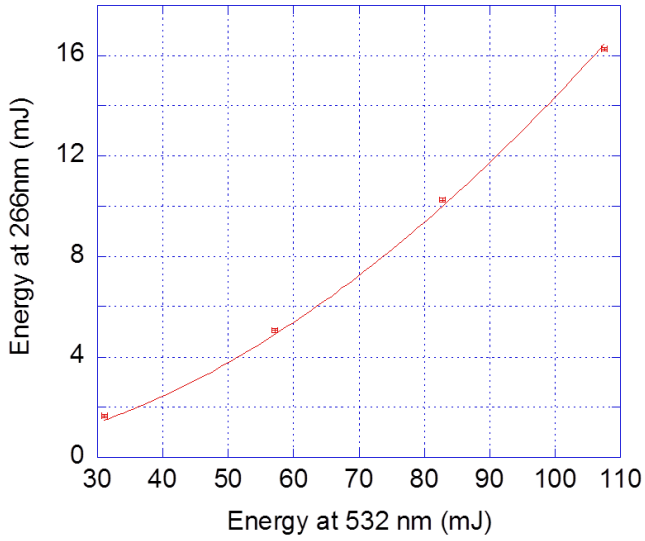

Figure 2.6: Fourth harmonic generation with 2.5 laser pump

0.5 when proper aligned.
Time profile can be measured with a fast photodiode and an oscilloscope. The laboratory oscilloscope had an acceptance band of 1 GHz, so we recorded images with a resolution of a bit less than 1 ns, thus smoothing the temporal pump profile. The time duration of the pulse depend on the cavity losses and on the inversion of population of the active medium [38], so it can change if the laser cavity is not properly aligned. A typical temporal shape of the pump pulse is presented in fig 2.15. From the oscilloscope we obtained the Fourier transformation of the intensity profile: it shows beats with longitudinal mode whose distance is the free spectral range of the cavity, i.e. the inverse of the time in which the light use to complete a round trip of the cavity. For this laser the free spectral range is 260 MHz.
The output dimension and divergence depend on thermal focal length of the rod, the alignment and the curvature radii of the cavity mirrors. We tried to change the M1 mirror radius, from 3m to 5m. The difference between the two cases is mainly the threshold value, around 700/1000 for 3 m and 750/1000 for 5 m, while energy, duration and output dimension are comparable. We chose the 3 m reflector in order to have lower threshold, that means more longitudinal mode inside the pulse. The output dimension and divergence is shaped with two lenses outside the cavity, in order to minimize divergence and have a pulse with sufficient small dimension to avoid the formation of

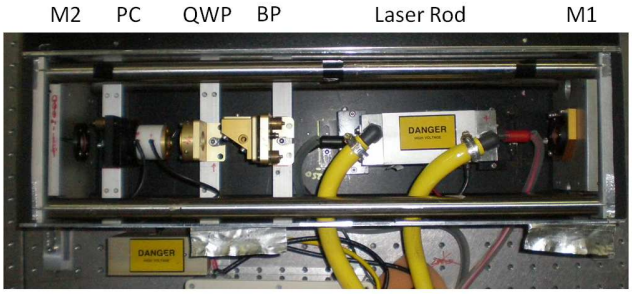

Figure 2.7: In the photo is shown the laser pump used in Milan tests. M1: rear mirror with a curvature radius of 3m and reflectivity > 99%, M2: output coupler, it is a gaussian mirror, PC: Pockel cell, QWP: quarter wave plate, BP: Brewster plate, Nd:YAG rod: ensemble of laser rod and pump lamp

complex ring structure in its transverse profile. Typical values of that features after the lenses system are 1 mm FWHM for the dimension and 0.5 mrad for the divergence.
The output energy in function of the lamp power (in a scale of 0-1000) is shown in fig 2.8. Near the threshold value the laser shows more instabilities than to the full power regime. In order to have a stable output in energy and dimension we usually have to wait about half an hour at 2 Hz repetition rate.

This pump was used for the generation of 1650 nm pulses and 205 nm

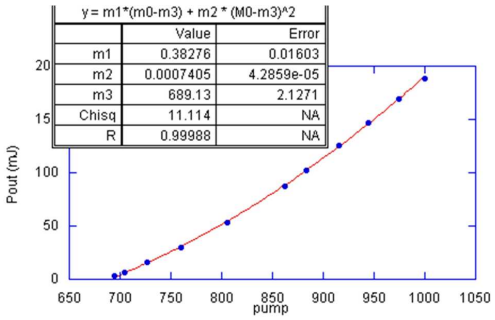

Figure 2.8: Output energy in fundamental harmonic for the Milan laser pump as a function of the lamp intensity (scaled from 0 to 1000). The fit is done with a quadratic polynomial function.

pulses. In the latter case the pulse are frequency doubled and quadrupled outside cavity, using LBO and BBO crystal. The typical energy level of the

second harmonic at 532 nm is shown in fig 2.9 and the fourth harmonic that can be subsequently generated is up to 30 mJ.

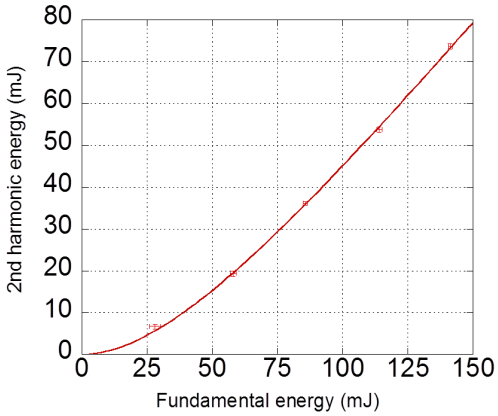

Figure 2.9: Maximum energy obtained from Milano pump laser in second harmonic as a function of fundamental energy pump for the LBO crystal.

2.3 Laser system for 3 to high-n excitation

In our experiment both the wavelength and the linewidth of the radiation of this laser pulse are not fixed in advance, therefore the laser system must have wavelength tunability with the required pulse energy and bandwidth. The system has to provide a radiation pulse with the following characteristics [30]:

1. tunable wavelength in the range $\lambda = 1650 - 1700$ nm
2. pulse length $\tau < 10$ ns
3. pulse energy equal or greater than 2 mJ
4. quasi-continuous spectrum with a spectrum FWHM $\Delta\lambda$ not broader than 4 nm, covering a Rydberg level band wide section.

These requirements cannot be satisfied simultaneously by commercial laser sources. The optical layout assembled in our lab is shown in Fig. 2.10.

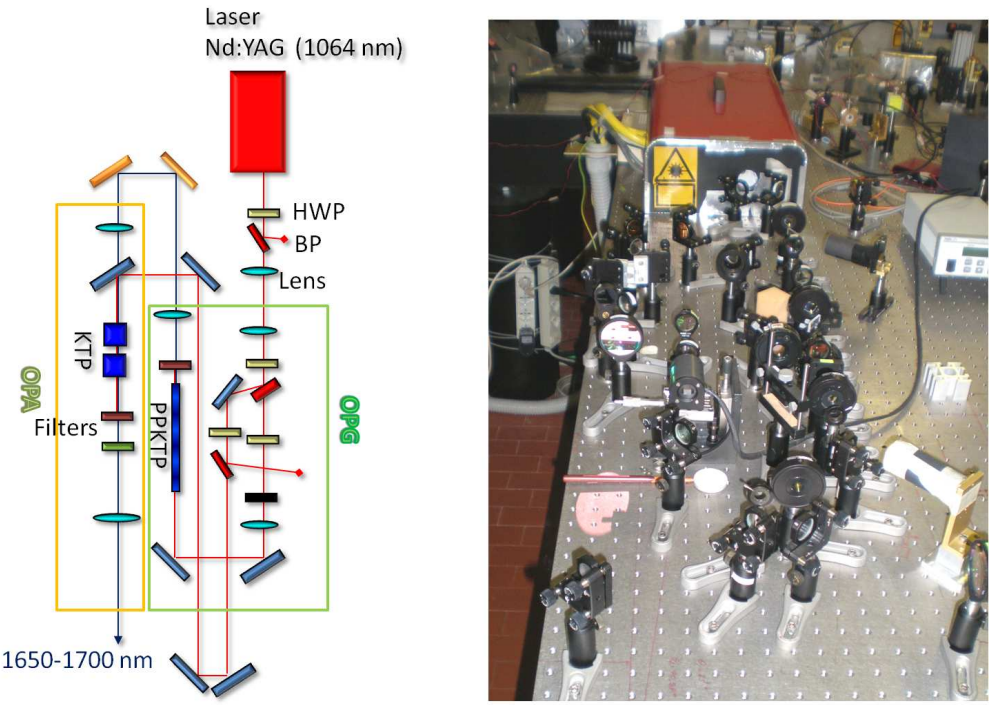

Figure 2.10: Experimental schematic: HWP, half-wave plate; BP, Brewster plate.

2.3.1 Opg for 1650-1700 nm generation

Following fig. 2.10, the laser pulses coming out form the pump are tightened by a telescope system from 4-6 mm to 1 mm FWHM and are collimated in order to compensate the small divergence, few mrad, of the emitted pulses. Then, with a couple of Brewster plate (BP) and half wave plate (HWP) the energy is directed partly in the opg and the opa arms, the exceeding part is taken apart from the system. When the BP are aligned (at Brewster angle [34]) the incoming vertical polarization is reflected, while the horizontal one not. Thus, when we use BP we first align it using an HWP to find the minimum of transmissivity, changing the polarization in order to have vertical polarization and to align BP at correct incidence angle. Rotating the HWP, we can choose continuously the laser polarization, thus the amount of horizontal polarized beam that the BP transmit. After the couple of HWP/BP we rotate the polarization coming from the BP with a HWP in order to make it vertical.
The beam must be calibrated to the dimension of the crystal channel to employ with maximum efficiency the whole crystal length. The divergence must be very low, up to a mrad, in order to avoid the generation of large spectral pulse due to the curvature of the beam that, in different point of the beam, sees different domain length due to wavefront curvature radius.

We used two different periodically poled crystals during the thesis: one of Lithium Niobate (PPLN) and one of Potassium Titanyl Phosphate (PPKTP). The former has greater nonlinear coefficient ($d_{eff,PPLN} = 14.8\ pm/V$, $d_{eff,PPKTP} = 9.4\ pm/V$ [36]) but its transverse dimension is lower (0.5 mm compared to 1.0 mm of PPKTP), due to the industrial capability of inducing domain orientation in crystal for the two different materials, and the damage threshold of PPLN is lower than PPKTP, thus we choose the latter for the final system. In this section we present the results for both crystal in order to justify the choice.
The first thing to do for OPG alignment is to choose the propagation direction and measure the dimension and divergence of the beam. For visible and near infrared measurements we used a CCD camera (Thorlabs DC 210) with 640 per 480 pixels resolution, each 7.4 μm long and height, and a color depth of 8 bit (fig. 2.11). The camera can be externally synchronized with the q-switch signal in order to lower signal to noise ratio acquiring data only when the pulse is emitted. The silicon pixel detector has a spectral range of about 350-1100 nm, thus it is almost blind for 1650-1700 nm pulse as well as for 205 nm, while it can see from the fundamental to (with some difficulty) the forth harmonic of Nd:YAG.

For the 0.5 mm height PPLN we reduced the pump beam to around 0.2 mm

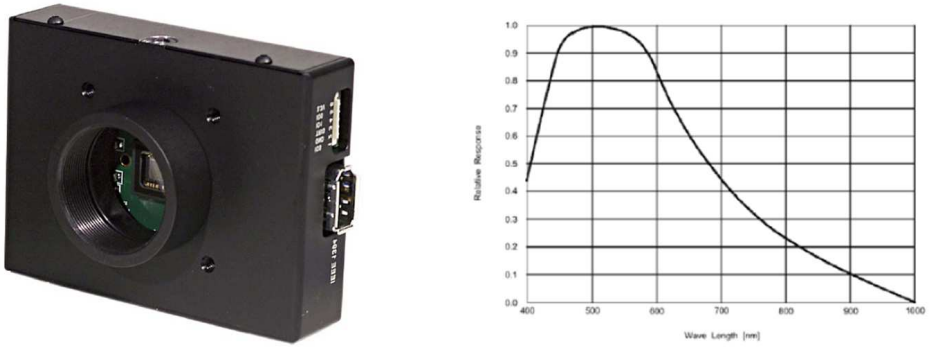

Figure 2.11: Image of the DC 210 CCD camera. On the screwed exit can be mounted neutral filters to lower the beam intensity, thus preventing image saturation. The second picture is the spectral response of the CCD camera, as tabulated in its manual.

FWHM with a 400 mm focal lens. The beam showed a small astigmatism, the foci of horizontal and vertical direction are not in the same position, so we had to work with a beam collimated in one direction and with a small divergence (or convergence) in the other. Another complication with beam transverse section is its transverse mode. It slowly change from a complex ring structure to a donut to a near Gaussian profile as the beam is focused and return to its complex structure far from focus. Those observations limit the position of a good profile for ours beam only to about 4-5 cm, that is of the same length of the PPLN crystal (40 mm). The resulting beam has a convergence of about 0.9 mrad in horizontal and 0.6 mrad in vertical direction, with a FWHM of about 0.26 per 0.21 mm.

For the larger height of PPKTP, of 1 mm, we chose to use a 1 m focal lens after the HWP/BP system. With such a long focal length, the beam is more collimated and the divergence for horizontal and vertical direction is 0.25 per 0.22 mrad, thus the longitudinal position of the crystal become less critical, while the FWHM dimension are 0.45 mm in horizontal and 0.36 mm in vertical direction. Dimensions below half the crystal height guarantee better output transverse profiles while larger dimensions allow to use more energy, thus increasing the energy output of the generated signal. The chosen dimensions are a compromise of spatial quality, dimension, divergence of the pump and maximum energy generation in the signal pulse.
Once we prepared the pump beam and found the best longitudinal distance

from the converging lens for the crystal, it needs to be inserted on the pulse path and aligned. The crystal is mounted inside an electrical driven oven (Thorlabs PV40) that stabilize the crystal temperature and allow to change it remotely up to 200 °C. The oven is mounted on a couple of micrometer driven stages that allow fine tuning in crystal position in the direction orthogonal to the pulse propagation. The alignment procedure we used is described in appendix A.2.
We have empirically found that the PPLN had an intensity damage threshold of about 70 MW/cm^2, due to the crystal composition and antireflection coating on the crystal surfaces. This threshold constrain us to limit the energy per pulse used in the parametric generation, that for the laser duration and the spot size used is up to about 400 μJ. PPKTP allow us to increase this energy value due to its larger transverse area and for the intrinsic material threshold that is higher, thus we limited energy to about 2 mJ in order to have 100 MW/cm^2 on the crystal.

The energy generated by the two crystal for pulse characteristics listed above are reported in fig. 2.12. The outcoming pump at 1064 nm is separated by signal and idler pulses, at 1670-1700 nm and 2840-2930 nm, using a mirror composed by a reflecting coating for 1064 nm and a bulk of 6 mm of BK7 glass, that has high transmissivity for signal and absorb almost all the idler (see fig. 2.13 for transmissivity curve). A small fraction, not measurable with ours energy meter, of the pump is converted in second harmonic (green at 532 nm) and, while it doesn't contribute to nonlinear processes, it is useful to find the downconverted pulse in first phases of subsequently alignments. This low energy green light can be separated from infrared using a high pass wavelength filter, usually in order to have a cleaner image of the infrared pulse on the CCD. The fraction of pump energy converted to signal we achieved is up to 12 %.
We have measured the spectrum produced by OPG for both crystal. The PPLN crystal has 9 channels with different periodicity in its domain lengths, ranging from 29.50 to 30.75 μm. We measured the center of the spectrum changing the channel and the crystal temperature and the data for useful wavelengths (for positronium excitation) are reported in fig. 2.14. We used for this measurement an homemade spectrometer made with a reflecting grating and a photodiode, finding an half maximum spectral width of 4 nm.

We measured the spectrum on PPKTP crystal varying its temperature. In order to use a commercial compact spectrometer (Thorlabs CCS 175) that is sensible in the range 500-1100 nm, we collimated the signal pulse and used a nonlinear crystal to double its frequency, resulting in a wavelength of 830-

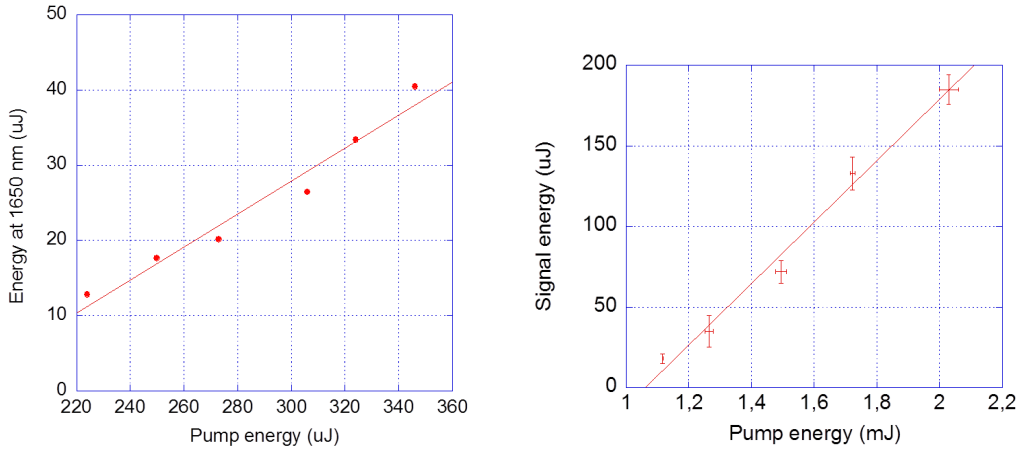

Figure 2.12: Energy output as a function of pump energy for PPLN and PPKTP with beam characteristics described in text. As the PPKTP has larger transverse area, it can withstand more pump energy thus producing more energy at the desired wavelength.

860 nm. Fig 2.14 shows the resulting temperature dependence of the signal wavelengths, reconstructed doubling the spectrometer output wavelength. The measured spectrum of the second harmonic is reduced in respect of the fundamental spectrum by a factor between 2 and $2\sqrt{2}$ as a function of how much the fundamental is converted to the second harmonic [34], thus having a spectrum on 1670-1700 nm of about 2-3 nm. The resulting positronium levels that this radiation can excite are between 16 and 21, for higher n levels a crystal with different periodicity is required, while the optics and the laser system don't require modification.

The time duration of the signal pulses, measured with a fast photodetector of InGaAs (Thorlabs D400 FC), is shorter than pump pulses, see fig. 2.15. This is due to the fact that the nonlinear process is more efficient when the intensity is higher, thus sharpening the time peaks of the pump dumping the tails of the pulses.

The output signal pulse is separated from pump and idler with a dichroic mirror and is collimated with a 100 mm focal length lens at its focal length from the crystal exit surface.

2.3.2 Opa for 1650-1700 nm amplification

The parametric amplification of the OPG2 radiation pulse is achieved with an Optical Parametric Amplifier (OPA) system based on a pair of KTP crystals

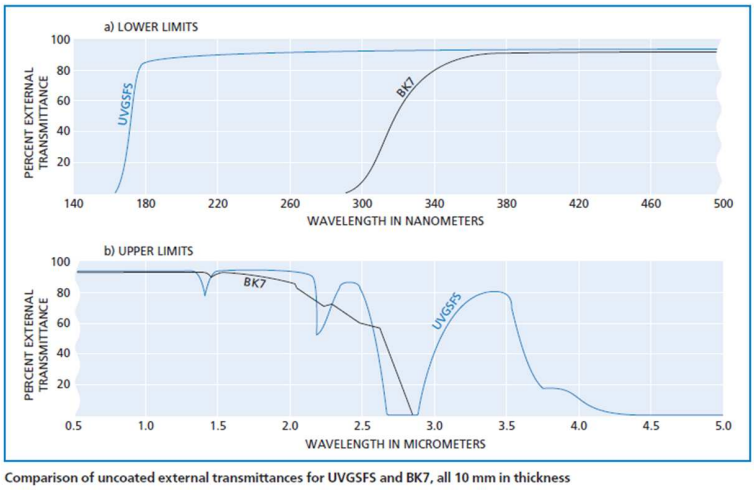

Figure 2.13: Comparison of uncoated external transmittances for UV Graded Synthetic Fused Silica and BK7, 10 mm in thickness (from CVI datasheet).

10 mm long and 5×5 mm^2 cross section. This device transforms Nd:YAG pump photons into signal photons by a stimulated down–conversion process described in sec. 2.1.2. The phase matching angle θ of those crystals are ranging from 70.1° at 1650 nm to 65.6° at 1700 nm, with $\phi = 0°$ [36]. The crystals we bought are cut at $\theta = 70.1°$.

The 1670 nm radiation coming from OPG2 is selected among other wavelengths by a dichroic mirror and a filter highly transmissive for wavelengths longer than 720 nm. The signal pulse must be collimated and overlapped with the pump on the crystal. In order to measure the dimension of the pulse, the CCD camera can't be used, its spectral sensitivity is too low at this wavelength (fig. 2.11). Nevertheless the CCD camera can see something when lighted with the signal pulse: considering the low intensity of the pulse on the CCD sensor, we think that the image we see isn't a two photon absorption of the sensor but the second harmonic at 830 nm that the PPKTP crystal emits at very low intensity (due to the fact that the process isn't phase matched) but the CCD has higher sensitivity at this wavelength than to the pump or signal ones. This consideration is supported by a test involving a mirror for a possible 1064 nm residual, a 10 nm pass band filter around 810 nm and tuning the OPG temperature to generate wavelength around 1620 nm: the CCD image appears when the second harmonic of the OPG signal match the filter band. The CCD camera can be used, thus, to check the alignment the signal pulse on the pump one but we can't measure

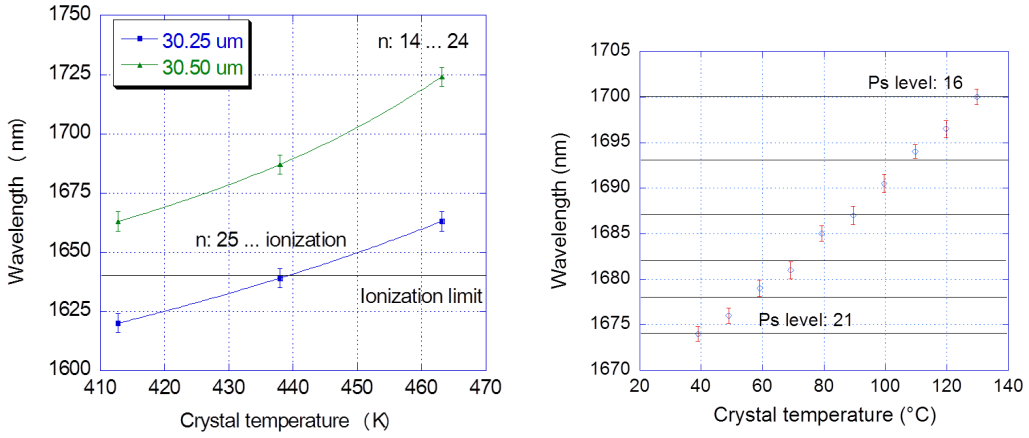

Figure 2.14: Spectrum of PPLN (a) and PPKTP (b) in function of the crystal temperature.

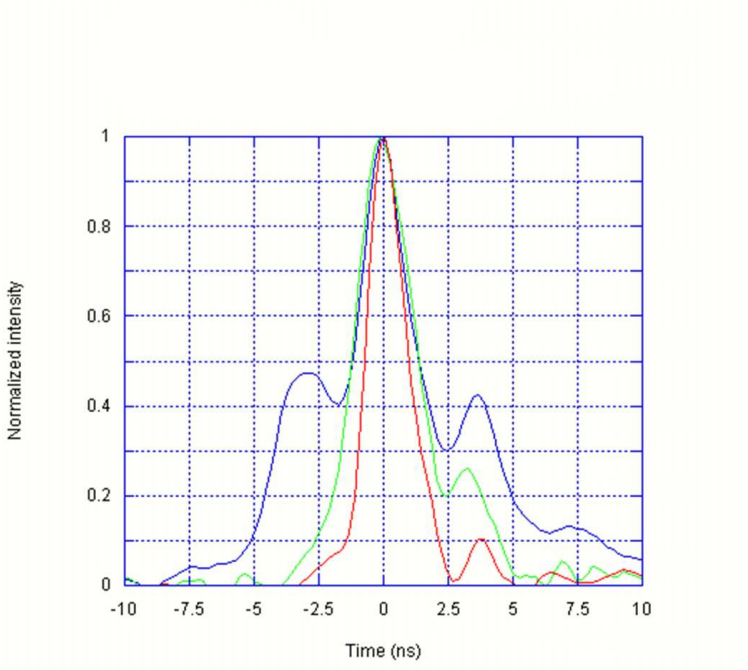

Figure 2.15: Temporal shape of the pump (Blue), OPG signal (Green), and OPA signal (Red) taken with a fast InGaAs photodiode and 2 GHz oscilloscope.

directly the OPG signal dimension and exact focal point (due to chromatic aberration of the lenses). To perform such a measurement, we used the knife edge method: we registered the energy of the pulse moving an edge in front of it and extrapolating the dimension via a fit with an integration of a Gaussian intensity function:

$$E(x_k) = \int_{-\infty}^{x_k} \sqrt{\frac{2}{\pi}} \frac{E_0}{\sigma} e^{-2(x-x_0)^2/\sigma^2} dx \tag{2.10}$$

taking different positions of the edge (x_k). An example of this measurement is shown in fig. 2.16.

The FWHM of the pulses must be tailored to crystals characteristics: they

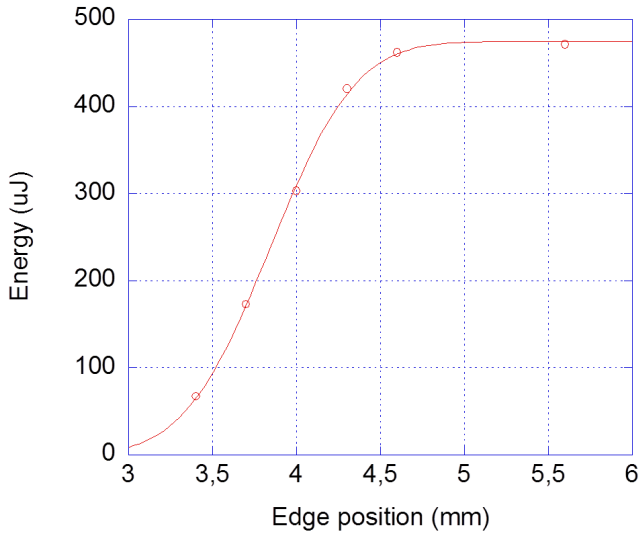

Figure 2.16: This graph shows the energy of the pulse as a function of the edge position. The resulting function is a integral function of a Gaussian function, that is fitted in order to find the FWHM of the dimension.

have a damage threshold of about 15 J/cm^2 for 1064 nm pulses of 10 ns and a antireflection coating with a slightly lower threshold, while the parametric amplification will increase with the pump and signal intensity. Another important point is the pulses stability in dimension: if the pulses fluctuate in its dimension and shape the resulting amplified signal is even more fluctuating in energy and dimension. We planned the laser system, in particular mirrors and lenses system, to have the signal and pump fluctuation correlated in the same direction; a poor choice of the number of mirror or lenses can lead to an increase in OPA fluctuation due to the anticorrelated fluctuation of the

pump and signal pulses. Larger transverse area pulses suffer less of this effect. Thus, we chose to work with a 550 μm waist FWHM signal superimposed to a 750 μm FWHM pump pulse. The alignment procedure is described in appendix A.3.

The polarization of the two pulses are both vertical, in the ordinary propagation direction inside the crystals as required by a type II phase matching scheme. To find the correct angle to phase match the pulses we tilted the crystals on the horizontal plane. We inserted the second crystal with its crystal axis rotated by 180 in respect of the first to compensate the walk–off of the idler inside the crystal (it propagates extraordinarily). The absolute maximum of the amplification is usual very critical in crystal angular alignment, so it is important to align very precisely the crystal in order to achieve the maximum value of the amplification.
OPA performance was investigated as function of the pump energy. In Fig. 2.17 the output energy versus the input energy is shown.
We remark that the point-to-point (natural) instability ($\sim 50\,\mu$rad) of the

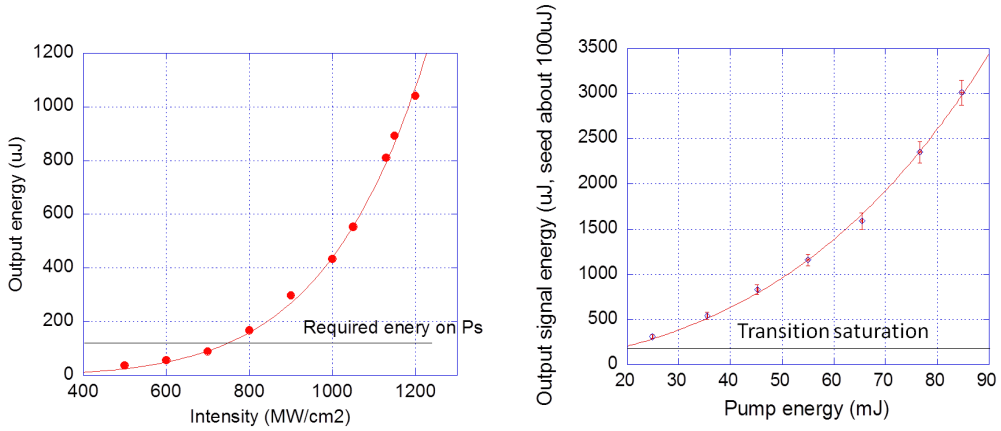

Figure 2.17: Graph of energy output as function of the pump energy for PPLN (a) and PPKTP (b) seed.

pump constrained to compact the design as much as possible, willing to minimize the jittering in the signal-pump overlap, in order to minimize the output energy-jitter. A further contribution to the observed jitter is due to the waist dimension jitter of the pump beam.

Attention had to be paid, in operation above threshold, to pump energy and alignment to avoid emission of broadband unseeded generation from the second stage. This effect, common for all the amplifier with high gain, is

analogous of the OPG process used in the previous section. There are two great disadvantage in this generation, however: the spectrum is broader due to the smaller length of the OPA crystals and the energy per pulse of this process fluctuate dramatically because the process is in an exponential gain regime rather than in a saturated one as done in our OPG. Thus we chose to operate with a pump intensity low enough to do not trigger our energy meter, i.e. measuring an energy lower than 15 μJ for the unseeded pulses (we checked the OPA for at least many tens of pulses, more at higher pump level) compared to the maximum of about 3 mJ of seeded operation.

We found that the spectrum of OPA is compatible with those of OPG (fig. 2.14), while when the crystals are not properly phase matched, in addition to a lower gain, the OPA will amplify a spectrum tail of the OPG signal, thus deforming its spectrum with a total effect of an increase in its width. We checked that the OPA crystals we used can be phase matched for all the wavelength produced by OPG, while the crystals surface become tilted with a not so small angle for 1700 nm and longer wavelengths, thus reducing the useful crystal area in which the pulses can travel without hitting the crystal walls. In order to generate wavelengths greater than 1720 nm (thus exciting positronium to levels lower than n =14) we need to change the crystals cutting angle to phase match them.
Another factor that depend on phase matching, as well as on the superposition of the pulses, is the pulse transverse quality. The resulting M^2 is 3 - 4 on the maximum of amplification and increase with the phase detuning and pulses divergence. This effect must be accounted in the following transport line design.
In conclusion we can obtain a maximum of about 3 mJ, many times the saturation energy, so we can operate with a safety margin useful for unseen future problems as discussed in section 2.1.

2.4 Laser system for 1 to 3 transition

Summarizing the discussion presented in sec. 3.3.2 and 2.1, on the laser system at 205 nm responsible for the excitation ($n = 1 \rightarrow n = 3$) we have the following requirements:

1. spectral bandwidth larger than 30 GHz RMS, mainly accounting for the Doppler broadening,

2. a pulse duration shorter than 10 ns,

3. an integrated energy many times larger than 2.2 μJ .

The requirements on the spectral properties and the pulse duration are easily fulfilled by using an optical parametric converter (OPG1) pumped by a Q-switched pump laser and amplified in a bulk crystal (OPA1). Hence this approach is in fact preferred over others schemes, like tripling of 615 nm suggested in [39] and proposed in a former Ps excitation scheme [16]. On the other hand the requirements on the wavelength and the energy per pulse are not as trivial to be fulfilled. In fact producing 205 nm photons by direct parametric down-conversion is not realistic because of the lack of suitable pump lasers at wavelengths shorter than 205 nm. Alternative approaches based on harmonic generation, such as frequency doubling or tripling, on down-converted photons at longer wavelength are not viable mainly because of the limited efficiency reachable in the harmonic process.

Given these constraints, we have considered a different approach based both

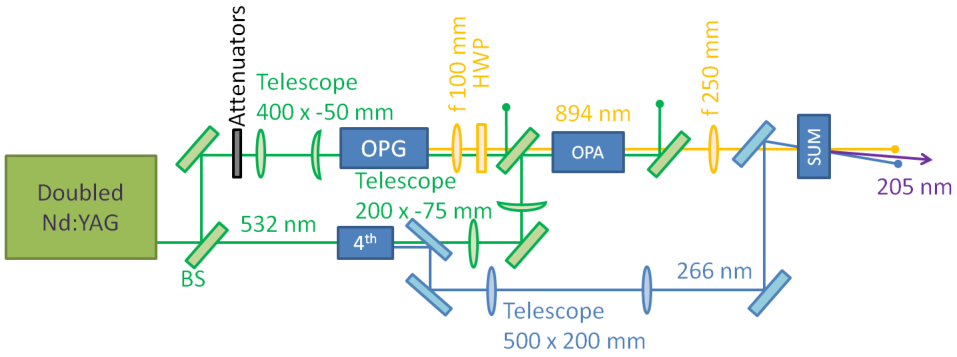

Figure 2.18: Scheme of the laser system for 205 nm generation. HWP: half-wave plate; BS, beam splitter.

on parametric down-conversion and frequency summing processes [40, 41]. Here the first requirement is satisfied by generating radiation at 894 nm with an OPG pumped by a nanosecond laser at 532 nm. Subsequently the 894 nm light is frequency summed to the second harmonic of the same pump laser, at a wavelength of 266 nm, finally generating 205 nm radiation. Compared to the case of direct harmonic generation of the OPG radiation, with our approach the conversion process towards 205 nm is considerably more effective because of the large amount of energy available at 266 nm with nanosecond lasers which boosts the nonlinear conversion towards the deep UV.

A sketch of the experimental layout for the test of this laser system is depicted in Fig. 2.18. The pump, described in section 2.2.1, is a 6-ns pulsed

Nd:YAG doubled to 532 nm, giving an energy of up to 75 mJ per pulse. A beam splitter sends one tenth of the 532 nm pulse to the OPG1 generating 894 nm radiation. The remainder is used for pumping the OPA1 crystal after traversing a second frequency doubling stage, based on a BBO nonlinear crystal, which can convert up to 13 mJ of the energy into a 266 nm pulse. The OPG1 is based on a 30 mm PPKTP crystal. The crystal is pumped with pulses up to 3 mJ, resulting in pulses of energy up to 500 μJ in the infrared [41]. In order to have more energy on the spectral acceptance band of the sum frequency crystal we used an OPA composed by two 12-mm long BBO crystals (OPA1 in Fig. 2.18) in a type-I phase matching condition, pumped by the 532 nm pulse not converted to 266 nm. The amplified signal energy at 894 nm in this optimized operative condition is within 3 and 4 mJ. Finally, the frequency summing stage is composed by a dichroic mirror superposing the radiations at 894 nm and 266 nm, followed by a BBO crystal (labelled SUM in Fig. 2.18) cut to satisfy the type-I phase matching condition for the process 894 nm + 266 nm $\rightarrow$ 205 nm. The two pulses cross the crystal in a noncollinear configuration, with an angle of 5° between the 894 nm pulse and the 266 nm pulse, in order to separate the 205 nm from the more intense 266 nm. The results of this system are presented below.

2.4.1 Opg for 894 nm generation

The first stage of the generation of 205 nm wavelength is the generation of the pulse at 894 nm to be summed with the fourth harmonic of the Nd:YAG pump at 266 nm. We used a PPKTP crystal with a periodicity of 9.05 μm, 30 mm long and with a transverse section of 1×2 mm^2 inserted initially in an homemade oven with a feedback temperature control, then in a Thorlabs oven (same model used in the previous OPG section) with dedicated commercial electronics. The pump wavelength of 532 nm is down converted in a pulse at 894 nm and another at 1313 nm, all of them with vertical polarization.

The pump pulse at 532 nm is split in two branches by a beam splitter 10/90, the smaller part is then attenuated using neutral absorption filters and collimated and tightened by a telescope system. The pulses dimensions are compatible with those used in the previously OPG, of about 0.5 mm FWHM. The alignment is done following the procedure described in appendix.
The energy produced at 894 nm as a function of the pump energy is shown in graph 2.19. The pump, signal and idler pulses are decoupled using a

dichroic mirror for green light, with high transmittance to signal and idler infrareds. The dichroic doesn't absorb energy in infrared spectrum, thus the output pulse energy is composed by 532/894 = 0.595 of 894 nm signal and the remaining 1313/894 = 0.405 of 1313 nm idler. We verified this value with broadband infrared mirror coating (Thorlabs BB1-E03 mirrors) that have low (about 44% compared to more than 99% for 895 nm) reflectivity to 1313 nm radiation, using 3 of them to reduce the idler concentration to low values. Those mirrors, however, have low energy damage threshold, so we use signal and idler superimposed for the subsequent OPA stage, having a better amplification due to the fact that the idler is present at the starting of the crystal, aiding the amplification process. During the thesis works we had to cut the crystal to 28 mm because of a surface damage done exposing the crystal to a laser pulse energy too high. The result of this operation is barely visible on energy production, due to the saturation level of the process, but the spectrum is slightly increased.

We have measured the spectrum with a commercial compact spectrometer

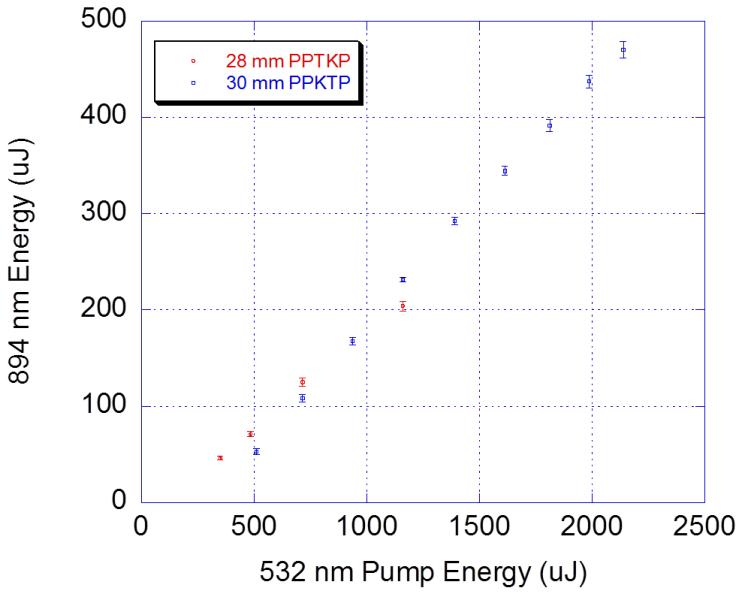

Figure 2.19: Plot of energy production at 894 nm as a function of the pump energy. The two set of data are referring to the OPG before and after the cutting of the crystal

(Thorlabs CCS 175, with a grating of 830 lines/mm, 800 nm blaze, a spectral range of 500-1100 nm and a FWHM resolution of 0.6 nm at 633 nm). The

laser spectrum as a function of pump intensity and crystal temperature is presented in fig. 2.20. We optimized the crystal temperature in order to generate a pulse spectrum centered at the desired wavelength of 894 nm required to generate 205 nm summed with 266 nm fourth harmonic of Nd:YAG.
The spectrum width is large, about 3-5 nm, and is a function of the input pump energy: we saw that an increase of pump energy lead to a small increase of the energy at 894 nm and a more pronounced increase in spectrum tails. This behavior is mainly due to two factors: pump spatial quality and crystal characteristics. The pump used (sec. 2.2.1) was aged, slightly elliptical and with a greater divergence than what we used to generate 1650-1700 nm pulses, thus we have a worse spatial quality of the pump pulses. The alignment was done without one of the slits used in previously section, thus requiring more accurate manual positioning and allowing for a small increase in misalignment, mitigated by the use of CCD camera that can see both the pump and the signal, improving the alignment seeing the shape of the pulses out coming from the crystal. The crystal itself, however, has a smaller periodicity than the PPKTP used in sec. 2.3.1, so if we consider that the poling of the crystal, in both case KTP, will lead to comparable errors in the length of each domain, the smaller period of this crystal will result in an increase of fractional error in periodicity, thus we expect to see an increasing spectral width.

While in a first test we used directly the energy produced by the OPG in

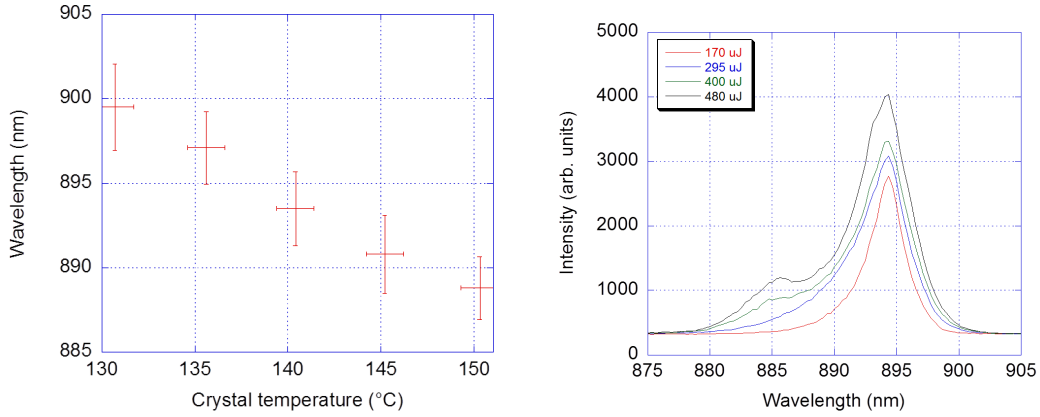

Figure 2.20: Plot of the spectrum of the OPG as a function of the crystal temperature, normalized to 1. The second plot is taken at fixed temperature and with a progressive increase in pump energy without normalization.

sum with the fourth harmonic to generate 205 nm, the low energy production of this approach require an amplification stage similar to what we used in

sec. 2.3.2.

2.4.2 Opa for 894 nm amplification

We chose to increase the energy at 894 nm using an Optical Parametric Amplifier, as done for 1650-1700 nm pulses. The crystal are two BBO with dimensions of $5 \times 5 \times 12$ mm^3, with a cut angle of $\theta = 22.6°$, $\phi = 0°$ with optical axis and type I phase matching.
In firsts measurements we used a *4f* system to select a smaller OPG spectrum to be amplified. This system is composed by a diffraction grating (of 1800 lines/mm), a focalizing lens with focal length 200 mm, a mirror for 894 nm and an iris right before the mirror (fig. 2.21). The lens is at its focal length from both the mirror and the grating, thus obtaining a Fourier transform of the spectrum in the focal plane on the mirror where the iris can select a fraction of the spectrum. This iris must be carefully aligned to the center of the pulse on mirror in order to maximize the energy transmitted on desired wavelength. The mirror is slightly tilted on vertical plane in order to separate enough the incoming and outcoming pulses on grating. Using a mirror it is possible to redirect the outcoming pulse to the OPA stage. The resulting resolution for this system is about 0.9 nm. In fig. 2.21 is shown the pulse spectrum after the *4f* spectral selection as a function of the iris aperture.

The energy coming out from the *4f* system is reduced by the diffraction efficiency of the grating, that we measured to be 55 ± 5 % for 894 nm, and it doesn't diffract 1313 nm. The measured efficiency for the whole *4f* system is 31 ± 3 % for a fully open iris. The energy and spectrum output of the system as a function of the iris aperture is reported in fig 2.22. The system result effective up to 1.5 nm of spectrum, obtained with a 2 mm diameter iris. Some difficulties arise in tightening more the iris due to the manual alignment of the iris we had to do and for the intrinsic resolution of the system, close to the value obtained at 2 mm diameter.

We built a delay line for the OPA pump pulse using 532 nm mirrors, due to the length of the *4f* system of 80 cm and few more tens cm to have the pulses coming in and out of the system separated enough to carry away the output using a mirror, without covering the incoming pulses. The pump and the signal are superimposed and collimated to a dimension of about 1.7 mm FWHM. At this dimension, the pump is clearly elliptical, due to an astigmatism of the pulse, while the signal is quite round so the resulting pulse from OPA won't exploit the maximum amplifier capability but with a careful alignment we can have high amplification. The results of maximum amplification, using one crystal, is reported in table 2.1. In this table is considered

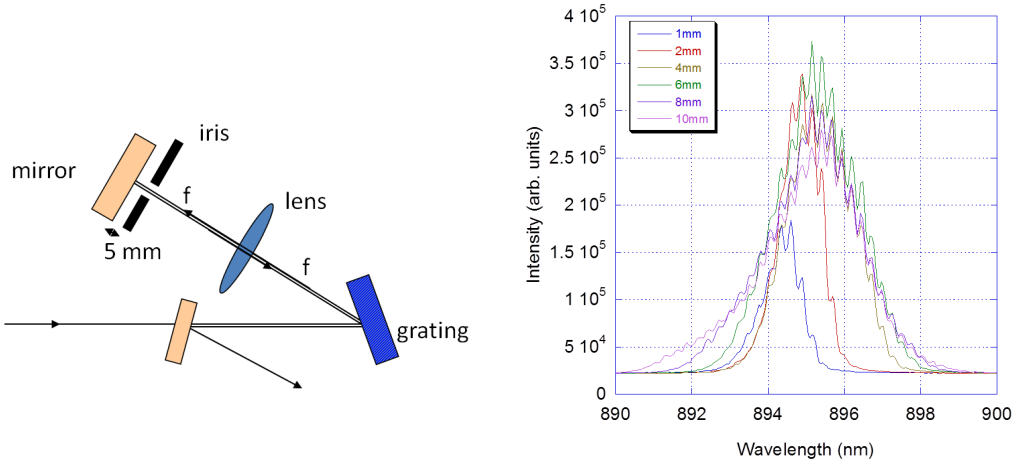

Figure 2.21: Scheme of *4f* system and output spectrum for 160 uJ of 894 nm pulse as a function of the iris diameter. The image of the pulse on a infrared viewing card is large, few cm, and saturated so it is difficult to center the iris on the maximum of the spectrum, doing so the registered value is near the same also for a 1 mm diameter iris.

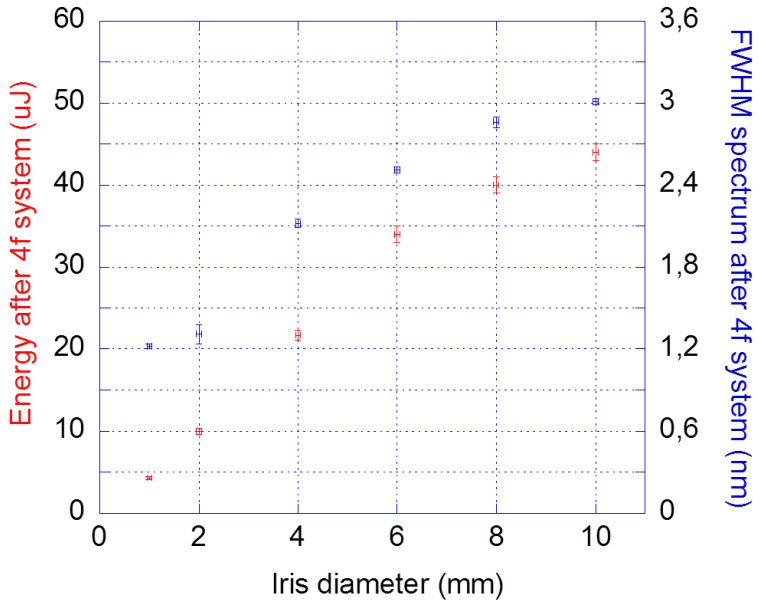

Figure 2.22: Energy and spectrum output of *4f* system as a function of the iris diameter.

4f output energy (μJ)	OPA output energy (μJ)	Gain	Spectrum FWHM (nm)	Energy on 0.27 (0.45) nm band (μJ)
39	160	4.2	3	15 (24)
20	89	4.5	2	12 (20)
11	67	6.1	1.5	12 (20)
6.6	71	11	1	19 (32)
87	240	2.8	3	22 (36)
29	110	3.8	2	15 (25)
16	66	4.2	1	18 (30)

Table 2.1: Maximum of the values obtained by the *4f* and OPA systems for 36 mJ of 532 nm pump and 140 (firsts data set) or 350 (second data set) μJ 894 nm OPG output. The bandwidths indicated in the last column are referred to the acceptance band of a 5 (3) mm long BBO for sum frequency to 205 nm

the accepted infrared band for 205 nm pulse generation, showing that the results are quite independent from iris opening, thus allowing us to reduce the infrared spectrum in order to guarantee the exact wavelength generation in the ultraviolet via a spectroscopic measurement of infrared spectrum.

We also tried to use the OPG output without the spectral selection of *4f* system, the value for amplification in the same configuration as for *4f* system output is used. The results are that for a 3 nm spectrum OPG signal at 140 μJ (of which only 71 μJ come out from the OPA system without pumping due to optical losses) and 42 mJ of pump we obtained 1.5 mJ of signal, with a gain of 21 and 140 (230) μJ on sum crystal acceptance band. This spectral selection system, thus, introduce more losses than the effective gain in bandwidth reduction, resulting in less energy on the acceptance bandwidth of the sum crystal. Therefore we discarded the *4f* system, using a direct scheme of generation/amplification of the 894 nm. Using two crystal (one with a 180 optical axis rotation respect to the other to compensate walk-off) and increasing the pump pulse energy we obtained up to 7 mJ of 894 nm (fig. 2.23)

The OPA crystals, two BBO 12 mm long, are long enough to reduce the 894 nm spectrum to their acceptance band (that is 48.3 cm^{-1} per centimeter or 1.6 nm for the couple of crystal at 894 nm), amplifying only a band of the input signal, thus working as a spectral selector. It is possible to finely tune the phase matching to center the OPA spectrum inside the OPG signal wider band. This bandwidth selection, moreover, make an increase in OPG signal energy less effective because of the increase in spectrum width. A doubling

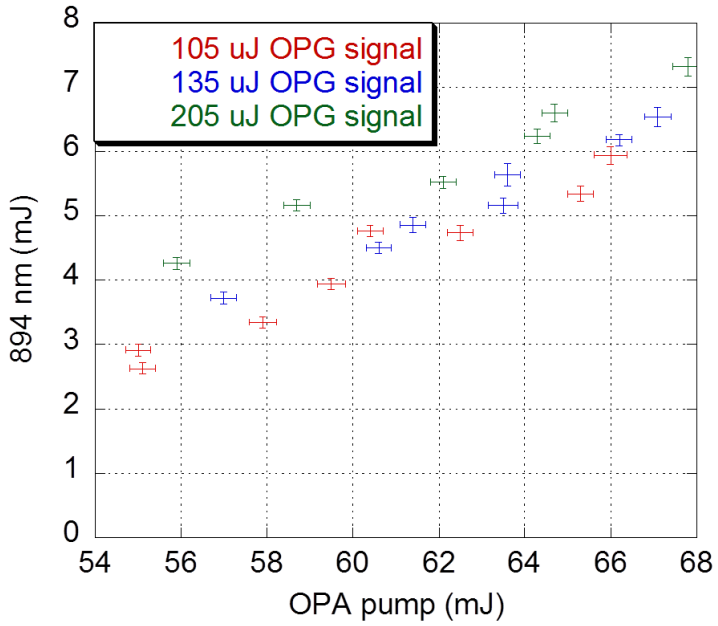

Figure 2.23: Energy per pulse at 894 nm coming out from OPA as a function of 532 nm pump energy and 894 nm seed energy.

in OPG energy, for example, results in a mere 10% increase in OPA energy (fig 2.23).

2.4.3 Frequency sum system for 205 nm generation

Having enough energy at 894 nm and 266 nm, we used a BBO crystal ($4\times4\times3$ or 5 mm^3 cut at $\theta = 58.7°$) to sum the frequencies to generate a 205 nm pulse in a type I noncollinear phase matching.
We chose a noncollinear configuration in order to separate the 205 nm ultraviolet from the more intense 266 nm pulse without dichroic mirrors, that are costly at this frequencies. Using a small angle between infrared and ultraviolet pumps, in the plane perpendicular to the phase matching, the sum frequency pulse is generated within this angle for moment conservation. For the wavelength we used and an angle between them of θ =5° (87 mrad), the resulting 205 nm pulse is at 1° 9' (20 mrad = $\theta \cdot 205/894$) from 266 nm pulse. The phase matching angle is slightly shifted due to crystal refraction, the angle is shifted by about a quarter degree for 2° angle between 205 and 266 nm pulses, so there is only a small tune in phase matching as long as the

angle between the pulses is small. The noncollinear configuration, however, can be used only for short crystal, else the two pulses won't be superimposed for the crystal length. For our case, the maximum separation of the pulses due to this angle is about 0.1-0.2 mm over a FWHM dimension of the pulses of 2 mm. The signal at 205 nm is separated, outside the crystal, by the others wavelengths by distance; 500 mm can separate the center of 266 and 205 nm pulses by 10 mm.

In a first configuration, we used the OPG signal directly with the fourth harmonic of the Nd:YAG. The 266 nm pulse is generated by a 6 mm BBO crystal from the 532 nm pump, with horizontal polarization and up to 14 mJ of energy per pulse. The 894 nm pulse come from the OPG, is separated by the green pump with dichroic mirrors collimated with lenses and the polarization is rotated from vertical to horizontal with a half wave plate. Using pulses well collimated and superimposed in a noncollinear way as stated before, we tuned the crystal angle, in vertical plane, to phase match the pulses and generate 205 nm radiation. This radiation can be seen, using common paper, as a light blue spot that appears few mm after the 266 nm fluorescence. The 205 nm energy per pulse we obtained was 15±5 μJ.
Splitting this radiation from the generated signal, we measured the wavelength produced, in order to investigate if the spot we saw was truly the sum frequency or it was a ghost image of the fourth harmonic from the previously optics, using a 1800 lines/mm grating. We obtained 206±6 nm of wavelength, clearly compatible with the expected 205 nm. The low resolution is due to the fact that we can't measure efficiently the spot size of the 205 nm radiation. The CCD silicon detector is blind at this low wavelength and human eye can't measure the fluorescence from the paper whit a submillimetric precision. We tried to measure 205 nm dimension in two way: the first is via the burning over a blacked paper, the other via an imaging with magnification equal to 1 of the fluorescence of the paper on the CCD camera. In both cases the result is of a two mm of diameter, but with some error margin.

Using the OPA system with the OPG and fourth harmonic generation, we produced more intense infrared pulses. Because, in our testing system, the green pump for OPA come out from the fourth harmonic generation, when we have the maximum of ultraviolet we have the minimum of amplified infrared and vice versa. Fig. 2.24 shows how many green pump can be used for OPA amplification as a function of the ultraviolet fourth harmonic produced.

We have used different conditions to find maximum 205 nm generation, varying the OPG pump and the energy in fourth harmonic and OPA pump. The results are reported in fig. 2.25. The maximum of the energy can be

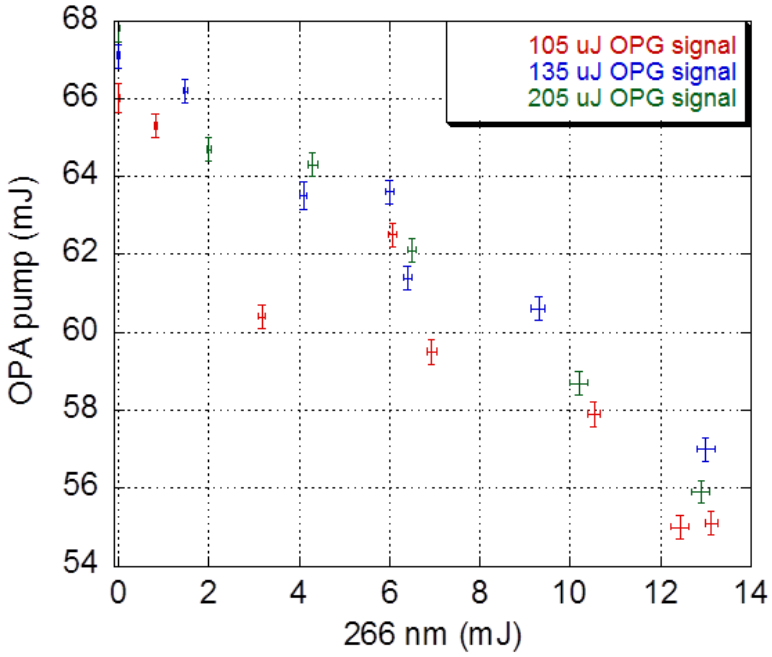

Figure 2.24: Energy per pulse at 532 nm coming out from fourth harmonic generation as a function of 266 nm energy produced.

obtained using a 5 mm long BBO and maximizing the ultraviolet production, obtaining about 300 μJ of energy per pulse at 205 nm. Using a 3 mm long crystal the results are 10% lower than what we measured for the longer crystal.

We thus can achieve energy well over the saturation energy required, of

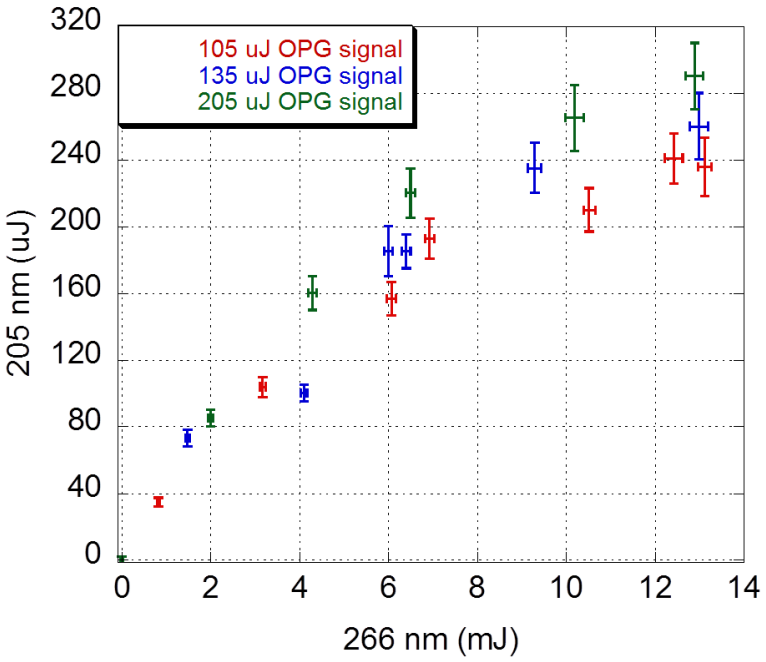

Figure 2.25: Energy per pulse at 205 nm as a function of 266 nm energy. The different set of data are for different pump energy for OPG crystal, the OPA output can be seen looking at fig 2.24 and to the corresponding value of fig 2.23

about 2 μJ per pulse. Using a laser pump with a separate channel to generate the maximum of infrared and ultraviolet simultaneously, using an higher energy per pulse pump on fundamental harmonic, can further increase the energy per pulse at 205 nm.

We haven't a spectrometer with a resolution high enough to measure the pulse spectrum. However, it can be simulated via SLNO [36] or esteemed with the spectrum of the summed pulses. The infrared pulse has a spectrum larger than the acceptance band of the sum crystal, thus the spectrum will be effectively reduced to crystal band. The spectral acceptance band of the BBO sum crystal is 51 GHz per cm, thus the infrared spectrum useful for

205 nm generation is 102 GHz for a 5 mm long crystal or 170 GHz for a 3 mm crystal ($\Delta\nu_{IR}$). The typical spectral band of the fourth harmonic of the Nd:YAG has a band of about ($\Delta\nu_{UV} = 60$ GHz); thus the 205 nm expected band should be $\sqrt{(\Delta\nu_{IR})^2 + (\Delta\nu_{UV})^2} \sim 120 - 180$ GHz (0.017-0.025 nm at 205 nm central wavelength) for 5 or 3 mm BBO. This value is larger than the foreseen transverse velocity Doppler effect on positronium, but the energy is far more higher. From a simulation of the excitation process (detailed in the section 3.3.2) the saturation energy of this larger spectrum pulse should be around 10 μJ, thus the energy we have is well over the saturation level, to overcome possible issues with transport line.

2.5 Study on optical transport line

After the realization of the two system for positronium laser excitation, we start to study how we can transfer the laser pulses from the laser table inside the Aegis apparatus to excite positronium. This optical transfer line must match some requirements of the Aegis apparatus:

- It must carry the laser pulse from standard pressure and temperature to ultrahigh vacuum (10^{-13} mbar) and cold (from 4 to 0.1 K), thus it must withstand very cold temperature and it must be done with components that can have low degassing in order to maintain the high vacuum level required.

- It must be insert in a very intense magnetic field (1 Tesla) and it mustn't perturb this field or increase the electric field, because this perturbation can severely compromise the particles manipulation done in the apparatus.

- It must carry on enough energy to excite positronium inside the apparatus, thus having moderate or low losses.

- It must be robust to withstand long usage times, because substituting frequently some of its component will require the opening of the Aegis cryostat, with long dead times on measurements required to evacuate it to ultrahigh vacuum.

- It must account for possible misalignments when the Aegis apparatus, composed by many types of materials, will be lowered in temperature, with different thermal compression of its internal components.

- It may be user friendly in order to lower the technical competence required to the shifters on a measurements campaign, allowing trained, but maybe not expert, in laser systems to operate with.

There are two main way to transport light in the apparatus: using mirrors and windows or using optical fibers.

2.5.1 Mirrors based optical transport line

The first way we tried was a mirror transport line. It is based on the simple propagation of the pulses in air or vacuum, with glass windows to insert the light inside the apparatus and some mirrors to drive it to the positronium atoms. In fig. 2.26 is shown the scheme of this transport line and a photo of its realization.

We plan to use two identical system, as described, for the two different

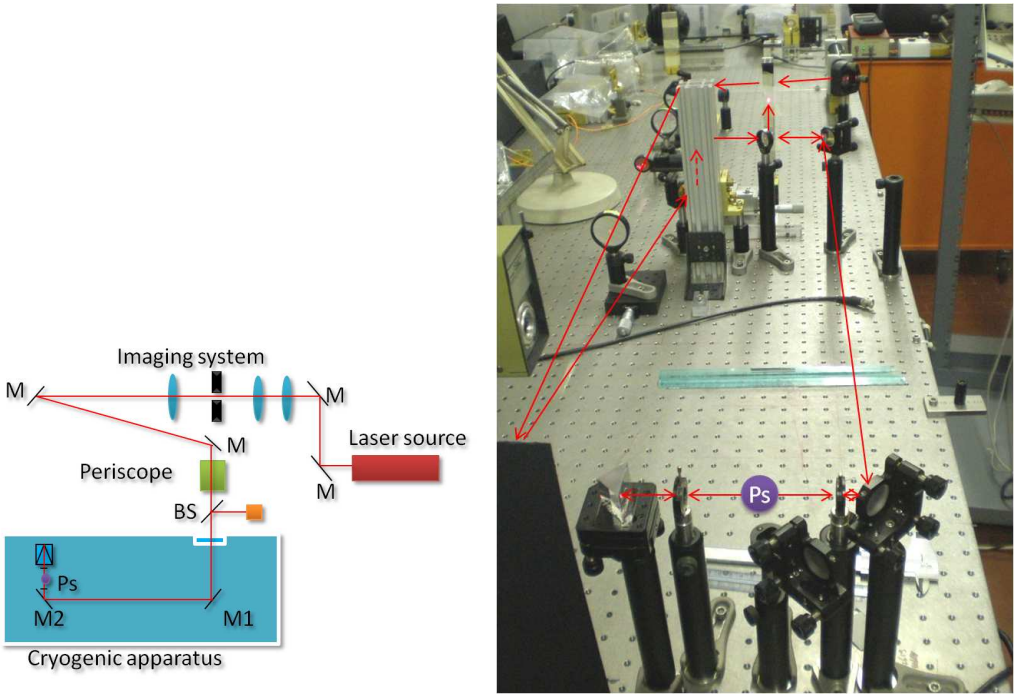

Figure 2.26: Scheme and a photo of the transport line described in this section.

wavelengths because the coatings required by the optics are very expensive if we require that they must be tailored for the two radiation simultaneously, rather than only one. The principle of functioning of the system, however, is

the same for both, thus we tested only one to understand its features.

The first element is a imaging system composed by three lenses and an iris with a 0.3 mm diameter. The focal lengths and distance of the lenses and iris were designed to have a magnification factor of 10 at the distance corresponding to the positronium cloud, realizing a magnified image of the beam that pass through the iris, thus having an hard edge on the transverse dimension, compared to the smoother quasi Gaussian tails of the pulses produced at 205 and 1650-1700 nm. This system reduce also the fluctuation in the pulse dimension and position, having an effect of stabilization on the whole system.
After the imaging lenses we used some mirror to fold and drive the laser pulses toward the Aegis apparatus. It is important to have at least two mirrors outside the apparatus with three dimensional and two angular degree of freedom to compensate possible misalignments occurring in the cooling of the apparatus.
We planned to use a beam splitter to have a feedback of the pulse after a round trip inside the apparatus. Using glass windows with antireflection coatings, mounted on ultrahigh vacuum flanges, we can carry the pulses inside the apparatus. Inside the vacuum chamber are present two mirrors and a corner cube. This last element will reflect backward the pulses on their paths, from all the direction they arrive and not only from the perpendicular to the surface as common mirrors. The back reflected pulse will exit from the same enter windows and, with the beam splitter, is redirect to a ruler to account for misalignments.

The losses for this system are due to reflection and absorption of the glass windows and for possible misalignments on the cooling of the apparatus. While the windows losses can be very low, using fused silica windows and an antireflection coating for the two wavelengths, it isn't easy to account for the alignment losses. Using standard 25 mm diameter mirrors and windows, accounting for a distance between the two mirrors inside the Aegis apparatus of about 750 mm and 200 mm for mirror to windows, we have a geometrical limitation on the mirrors misalignments that can be externally compensate. Looking at fig. 2.27, a misalignment on M1 can be corrected up to an angle of 32 mrad, while a misalignment of M2 can be corrected up to an angle of 6 mrad.
While an hot alignment can be made, the cooling of an apparatus composed by many different type of materials, with different thermal compressions, prevent to account a reasonable value of possible maximum misalignment for mirrors. Another issue of this system is the long and complex tech-

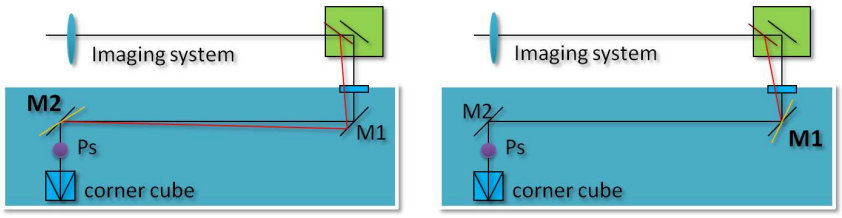

Figure 2.27: Scheme of the correction needed by misalignments of the mirrors inside Aegis apparatus. Using external mirrors we can compensate the misalignment of the mirrors (in orange) in a way that allow the pulses to travel in the same path around Ps cloud, tilting the input beam and centering the pulses on peripheral rather than central section of the mirrors

nique to maintain the alignment during the cooling process: we won't know what mirror is turning, so it is needed much time to check the system and a quick modification in angle, such of a thermal relaxation of some part of the apparatus, can perturb the alignment more than what the mirror can allow to have a feedback beam outside the apparatus, thus requiring a blind alignment that may ask many hours or even few days of very skilled people. Some of this issues can be solved using actuators inside the apparatus, but such devices must fulfill all the requirement described in the previously section, the most important are the vacuum compatibility of their components, the capability of be turned off during measurements to lower the heating in the very cold section of the apparatus and the capability to withstand the strong magnetic field of 1 Tesla without perturb it during the measurements. Nevertheless, such devices exist, AttoCube produces piezoelectric ceramic goniometers with a 90 mrad angular travel length, that withstand 5 Tesla fields, are ultrahigh vacuum compatible, can be remotely controlled and hold their position without electric consumption, however they are extremely expensive, few tents thousand euro each.

We decided to find another way to carry on the laser pulses, mainly because of the system capability to react to angular misalignments during the cooling down of Aegis apparatus, the requirement of very expert people to use it and for economical reason (dedicated mirrors and windows are expensive and a possible correction with goniometers is even more expensive).

2.5.2 Fibers based optical transport line

Another way to transfer the laser pulses from table to the Aegis apparatus is using optical fibers. This technique is analogue to what used by another antimatter experiment, Atrap [39], that excite cesium to perform a charge exchange with positrons to form positronium and subsequently use positronium to form antihydrogen with an antiprotons cloud.
We studied multimode fiber with a numerical aperture of 0.22. While the silica core and cladding of the fiber are usually vacuum compatible, the coating of the fiber, needed to bend it, is plastic, that usually has an high degassing rate. We thus opted for low degassing coatings, such as Tefzel or Kapton. Those plastics are hard and impervious to all but the strongest acid attacks, thus when we need to remove it we either scratch it mechanically or burn it. We used two different kind of fibers: one for infrared transmission and one for the ultraviolet. The infrared fiber has a low concentration of OH^- ion in its core, while ultraviolet has an high one. Ultraviolet transmission has also another issue with radiation around 214 nm, where center of color are forming. This effect is called *solarization* and will be described later. The fiber scheme is represented in fig. 2.28. We use an imaging system with

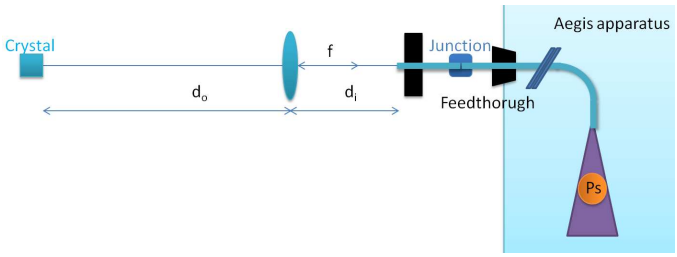

Figure 2.28: Scheme of the transport line from nonlinear crystals to the positronium using optical fibers.d_o is the distance between crystal and lens, d_i the distance between lens and fiber end, f the focal length of the lens. The magnification factor is d_i/d_o and the image is formed when $1/d_i + 1/d_o = 1/f$.

demagnification factor of 0.1 – 0.5 to couple the pulses to the fiber. Both the fiber and the lens are mounted on micrometer translational stages and the fiber end is mounted on a two axis rotational mount to better regulate the distance and direction of the fiber as a function of the pulses. The total fiber length we plan to use is about 10 cm outside the Aegis cryostat and about 1.6 m inside, accounting for some compensation on thermal compression of the apparatus when cooled. The fibers are coupled to the Aegis cryostat with feedthrough composed by a Teflon ferrule and a screwed nut. Inside

the apparatus, the fibers arrive in front of the recombination chamber to excite positronium, using the fiber output divergence to cover the expanding positronium cloud.

The fiber losses have different causes:

- Coupling losses: that losses are caused by reflection from the surface, due to the refraction index difference between air and fiber, and by coupling misalignment, due to beam too large, thus not fully coupled inside the fiber, or too small, with a divergence higher than the numerical aperture of the fiber. Another source of losses are the cut quality, a poorly cut fiber end reduce the coupling and increase the output divergence.

- Intrinsic material losses: it depends on the constituent material of the silica core, can be slightly changed with doping with high or low concentration of OH ions. An example of this can be found in fig. 2.30 for the fiber we used.

- Junction losses: we planned to use two section of fiber, one inside the apparatus and a smaller one just outside, for possible damage of the input end of the fiber during the Aegis working time. This action allow us to change only a small section of the fiber in a relatively easy way instead of requiring an opening and substitution of the whole fiber. Using two fiber allow us, also, to have small section of the fiber cut from manufacturer, thus with a very precise cut so with low coupling losses. The disadvantage of this technique is a loss due to the coupling of the two fiber. Using good quality coupler this loss is about 1 dB.

- Laser induced losses: that losses are caused by exposing the silica to a ultraviolet radiation around 214 nm. Such wavelength case the formation of center of color, that dissipate radiation along the fiber, increasing its losses per meter. This formation begin at the defect of crystalline lattice of the material or in presence of impurity. Some special technique exist to reduce this losses and special fiber can be purchased to operate with ultraviolet. One of this technique is to enrich the fiber with H_2 gas, when the ultraviolet light pass through the fiber the molecule dissociate and bind with defect, preventing the formation of color center. Such a technique, however, shows a degradation of transmission in time, due to the losses of hydrogen, and seems to

be not compatible with an experiment in ultrahigh vacuum for antihydrogen production. Other techniques involve the working of the core material in order to greatly reduce the defect in lattice and lower the impurity to reduce the induced losses.

The ends of the fiber must be cut with an high degree of precision. This operation can be done with specialized cutter, as done by fiber manufacturers, but this instruments are very specialized for one fiber diameter and usually very expensive. Thus we try to use the manufacturer's cut unless we need to re-cut the fiber. In this case we perform a manual cut with a diamond plated knife. This process require expertise and many cut may be done in order to have one good profile. To perform the cut we used a soft metal platform and paid attention to the knife positioning, perpendicular to the fiber and with a perpendicular inclination referred to the platform. We removed the coating using the flame from a common lighter because those coatings are resistant to standard chemical attacks, acetone for example. We fixed the fiber with tape or finger in order to don't move it during the cut, that must be neat. Even after many try, we can have one correct cut every about 10 tries. To verify the goodness of the cut we illuminate one end of the fiber with intense light and see the output of the other end: it must be circular and neat, with high intensity and without filaments or smears. We also checked it with a microscope to see eventual smearing on the edge of the cut, that frequently appeared in hand made cuts.
We used an imaging system to couple the laser pulses with the fibers. The pulses FWHM must be reduced to about 80% of the core diameter, thus the imaging system has a typical demagnification of 2-3 and a focal length of 100 mm or less for the infrared pulses in order to compress the imaging system. However, this relatively short focal length, combined with the small dimension of the fiber core, require an accurate system of translational stages with micrometer drivers to accurately align the transverse position and the angular direction to match the fiber end. We looked at the pulse shape after the fiber transport to tune the coupling alignment: the output beam must be rounded and uniform. With an energy meter is possible to maximize the output by a fine tuning of the coupling, reaching about 70-80 % of coupling with a very good alignment.
The output pulses from a multimodal fiber are characterized by a speckle energy distribution, as can be seen on a CCD camera with 1064 nm fundamental harmonic of the laser pump or with a second harmonic of the generated signal at 1650-1700 nm. With 1064 nm pulses we gain expertise on alignment quality of the output, the best alignment is done when the intensity profile is near circular with a relatively hard edge. When we looked at the second harmonic

of the signal, we measured a visibility, defined as $(I_{max} - I_{min})/(I_{max} + I_{min})$ of 0.14 for the 1650-1700 nm pulse. As reference, an image with the same visibility and feature of the real shape, obtained with computer graphic from second harmonic and 1064 nm images, is shown in fig. 2.29. The smoothed speckles are due to the large spectrum of the pulses, while a small spectrum pulse shows an higher visibility, i.e. a greater difference between maxima and minima.

The fiber we tested to transfer the infrared pulse is a IQinc. FG273LEC. It is

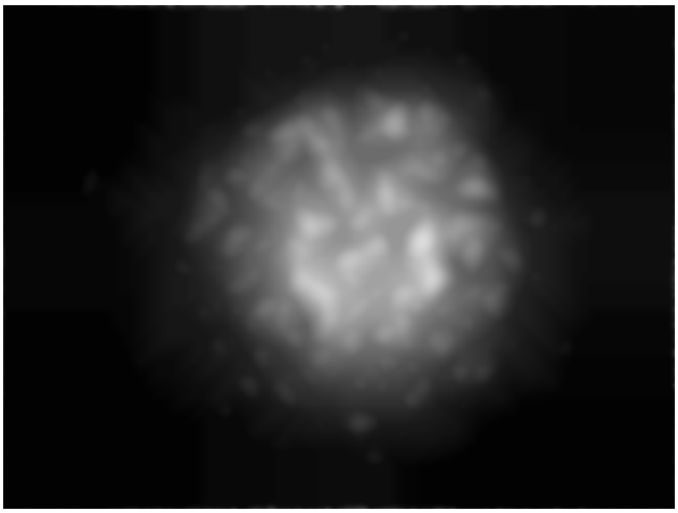

Figure 2.29: Computer reconstructed image of the 1650-1700 nm pulse profile using second harmonic of that pulse and 1064 nm pulse images. The final result is similar to the expected image of the signal.

composed by a silica core, a fluorine doped cladding, a secondary TESQ hard polymer cladding to improve its bending radius and a Tefzel buffer. Its core diameter is 273 μm, it has a numerical aperture of 0.22 and a core-cladding ratio of 1.1. We measured that a section of this fiber has a transmission of about 75% and this value is largely independent of the length of the fiber used, as long as the length is of some meter. This loss is due to coupling.

We performed a test with a bending radius of the stated value, 22 mm, without seeing losses in transmission and a bit smaller than it, up to 15 mm, with a small losses up to 15% of the unbent value.

We used a liquid nitrogen bath to test the fiber with a small, 2 cm, bending radius and at 77 K (the temperature of boiling liquid nitrogen), see fig. 2.31. Paying attention to the energy meter sensor, that is pyroelectric and thus it sees the environment cooling of liquid nitrogen as a reduction of the signal energy if the instrument head is posed too close to the cooling bath, the es-

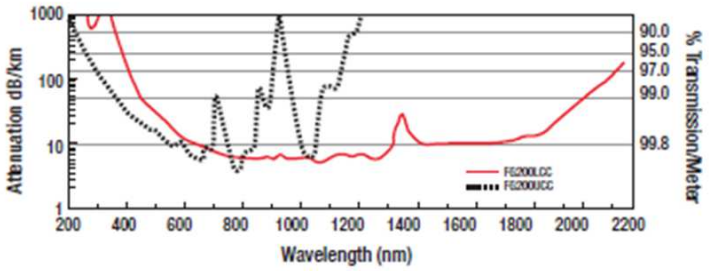

Figure 2.30: Intrinsic losses for the IQinc. silica fiber we tested for infrared and ultraviolet.

timated losses for the cold bath are less than 5% (the instrument precision). We tested the fiber head to repeated cycles of cooling and heating form room temperature to liquid nitrogen while the laser pulses are transmitted to the fiber without seeing an attenuation or a deterioration of the signal. We exposed a section of the fiber to a cold finger from a liquid helium vessel in a vacuum chamber, noting that even at very low temperature, about 6-8 K, the fiber maintain its integrity even with the vibration of the cryo and vacuum pumps.

We realized, in collaboration with the Politecnico di Milano group of R.

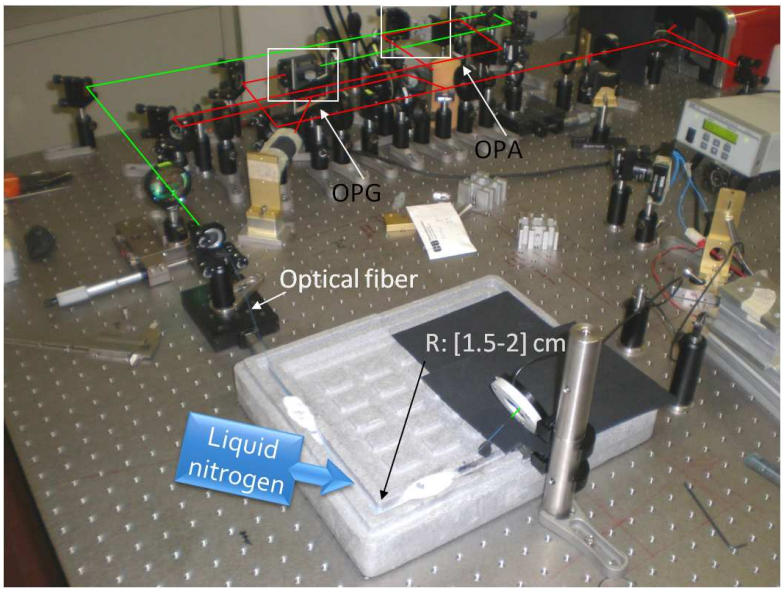

Figure 2.31: Photo of the experimental setup for generation and transmission of 1650-1700 nm throughout a fiber in a liquid nitrogen bath, bended to a small angle.

Ferragut, a feedthrough for the fiber with a Teflon ferrule, as demonstrated in [42]. We performed a hole in a Teflon ferrule and used it in a standard vacuum feedthrough, screwing the nut on the flange it is possible to ensure a good vacuum inside a chamber, our measurements state that the vacuum, up to 10^{-7} mbar, is not changed or compromised by the feedthrough or by a 1 meter of fiber we inserted. More sensible instrument and longer evacuation time is required to push forward the measurement to the ultrahigh vacuum of Aegis apparatus. We also tested about 1 meter of fiber inside the vacuum chamber in order to study the possible degassing with a mass spectrometer. We found (fig. 2.32) that a very small peak is present at 31 a.u. masses, we think that it is due to the CF^+ ion from the Tefzel coating [43] but we think that, due to low temperature of Aegis, this small degassing will be further suppressed.

We studied the exit divergence of a fiber section of about 80-60 cm (its

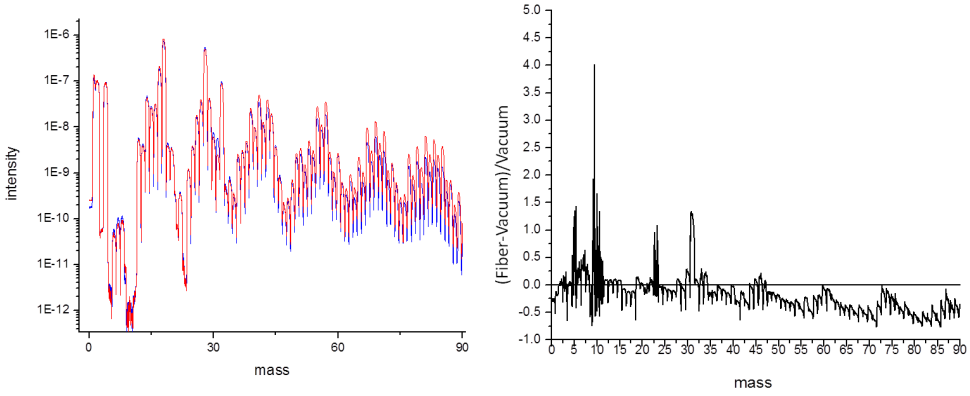

Figure 2.32: The image on the left shows the mass spectrometer output as a function of the atomic number. The red line was the vacuum chamber background and the blue line is the chamber + fiber signal. The difference of the two, shown on the right, presents a small peak at 31 atomic mass and some noise at 9-10 a.u. masses, not clearly defined as a possible degassing effect or a fluctuation in the measurements.

length was reduced by subsequently cuts) with a curvature radius of 22 mm. We first tested the dependence of the divergence from the cut of the end, measuring the exit divergence with two measurement of FWHM done with knife technique at different distances from the fiber end. The results (fig. 2.33) showed that even a cut that seemed good with white light transmission technique can be slightly different in the output divergence of the infrared pulse. Then we used one cut to perform studies on the dependence of the divergence from the alignment condition. We implemented two different pro-

cedures: the first, the simpler one, is to maximize the energy at the exit end of the fiber, the second is to maximize the energy that pass through an iris placed few mm after the fiber end and centered on the fiber output (fig. 2.33). We saw that, for the chosen cut that have a divergence of 160 mrad, the uncertain of the first approach is 40 mrad and 3 mrad for the second, thus an iris right after the fiber end may improve the alignment of the coupling system.

We measured the transmission on different types of fiber for ultraviolet

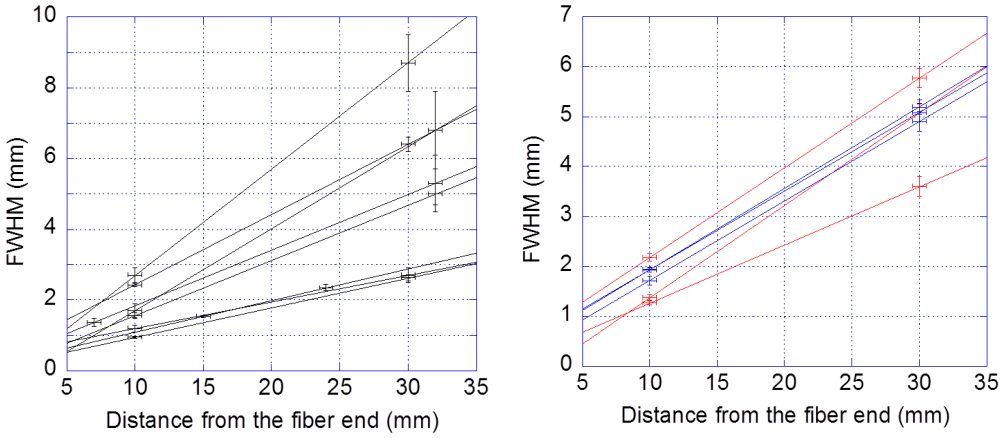

Figure 2.33: The graph on the left shows the dimension of the FWHM of the pulse after the fiber for different cuts. The graph on the right shows the FWHM dimension for the first (blue) and second (red) condition described in the section.

transmission.
The first fiber we studied, an IQinc. FG200UCC, has a core diameter of 200 μm, a core/cladding ratio of 1.2, a secondary cladding of TESQ and a Tefzel buffer, it has a numerical aperture of 0.22 and a bending radius of 18 mm.
The losses tabled by the manufacturer (fig. 2.30) are not negligible, about 1 dB/m for ours wavelength, but they halves the 205 nm energy in about 3 meter, while we planned to use a total of about 1.5-2 meter, thus expecting a total transmission for this fiber of about one third (= 0.7 (coupling) · 0.8 (junction) · 0.6 (intrinsic losses of silica)) or about 30 μJ for a 100 μJ of 205 nm energy per pulse input, many times the foreseen saturation energy. However, when we measured it with a imaging system like the one used for infrared carrying fiber, we see that the transmission throughout the fiber suddenly drop to very low value. At this low values, an half a meter fiber section transmit about 2-3% of the 100 μJ input pulse. Part of this low

transmission value is due to the worse alignment condition, that allow us to control only one transversal axis and the two angular direction, thus having an input coupling lower that what we obtained with infrared fiber, but the main losses are due to solarization. When all the lights are turned off in the laboratory, it is possible to see a very dim azure fluorescence of the fiber head, this color become reddish after about an hundred pulses (one minute at the 20 Hz repetition rate of the test pump). When the fiber is heated the azure fluorescence color is restored, until exposed to hundred ultraviolet pulses again. When we tried a longer, 3 meter, section, the output, still visible as a fluorescence on a common paper, is under the trigger of our energy meter (0.9 μJ).
We, thus, were be compelled to find another fiber for carry the ultraviolet pulses, looking for fiber that can transport our radiation without great solarization losses. We tested a Polymicro Technologies FDP200220240 model fiber, having a core diameter of 200 μm, a core/cladding ratio of 1.1 and a Polyimide (Kapton) buffer, it has a numerical aperture of 0.22 and a bending radius of 35 mm.
We measured two section lengths, one around 10 cm and another around 0.5 m, to evaluate the coupling losses and the losses due to the fiber material. When we performed this test, we used the Milan pump. We reconstructed the system done in sect. 2.4 with second and fourth harmonic generations, but this pulses have lower energy than what we used to test the 205 nm system in Florence, due to the lower output power of the fundamental pump. We can obtain about 8-10 μJ of 205 nm energy per pulse, thus the following tests are performed with this intensity of ultraviolet radiation. We performed some measurements, reported in fig. 2.34. Thus we extrapolated that the main losses were due to coupling: the pulse quality was lower than the infrared pulse and it was more difficult to align due to the presence of some tail from the 266 nm pulse, that is three order of magnitude more intense than 205 nm pulse. The amount of 266 nm radiation that we coupled in the fiber can be checked blocking the infrared signal an looking at the energy of the pulses measured. From a difference between the energy measured with and without the infrared pulse we can esteem how much 205 nm we have and how much we couple in the fiber, but it make the optimization more difficult and long. The value we presented are at neat of 266 nm pulses. Separating the losses between those that depend on the fiber length and those that are independent, we find that, fitting many measurements like what we presented before, a function of $C10^{-\alpha L/10}$, where $C = 0.30 \pm 0.05$ are due to coupling and reflection from surfaces, and $\alpha = 4 \pm 1 dB/m$ are due to intrinsic silica losses (about 1 dB/m, calculated from sections irradiated with a small number of pulses) and solarization effect at saturation (about 3 dB/m).

We tested the fiber in liquid nitrogen, as done for the fiber for infrared

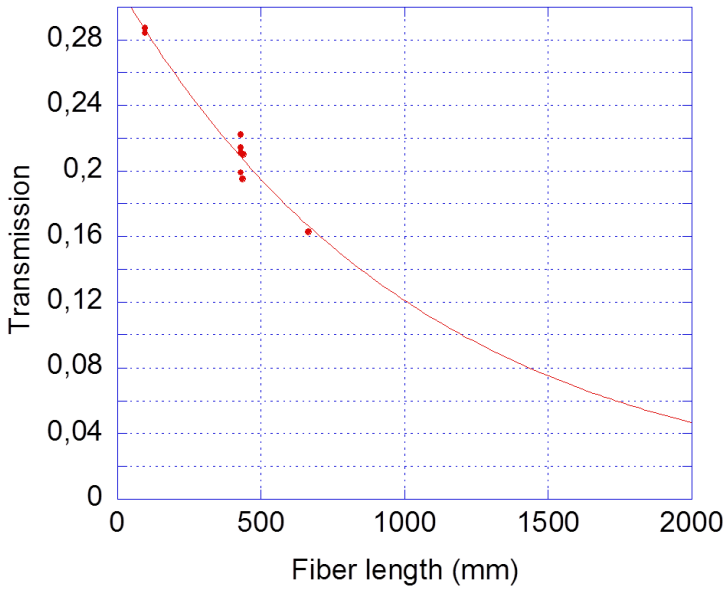

Figure 2.34: Total transmission measurements for Solarguide fiber of different sections, the value are reported for good alignment and at saturation. Before saturation the points at 430 mm are at about 26 % transmission with comparable error dispersion. The line is the fit function described in the text.

pulses, finding the same transmission we registered at room temperature. When we tried to bend the fiber with a radius less than what stated by the maker, 35 mm, we found that the transmission lowered, decreasing with the increasing of the bending radius. We measured the transmission as a function of the time, thus as a function of the number of the pulsed we sent into the fiber. For the firsts pulses (10 minutes at 2Hz rate) the total transmission of a 430 mm section is of about 26 %, the transmission value become stable, at about 22 %, for long time: after 20 minutes it had reach the saturation value, maintained for 3 hours. For comparison, we studied another fiber (Thorlabs UM22-200) with 200 μm of high OH core, numerical aperture 0.22 without anti-solarization treatments. The output of ultraviolet with a 105 mm section of this fiber for a 7.4 pm 1.7 μJ is 2.5 $\pm$ 0.8 μJ or 34 %. The output for a longer fiber section, 570 mm, showed a great dependence with exposure time: it start with a total transmission of 1.45$\pm$0.25 μJ on 7.2$\pm$1.5 μJ input (20 %), reducing it after 20 minutes (about 2500 total pulses at 2

Hz rate) to 1.22±0.19 μJ on 6.8±1.5 μJ input (18 %) and lowered under instrument threshold (posed at 0.6 μJ) on 6.8±1.7 μJ ($< 9\%$) after 40 minutes (about 5000 total pulses). Thus, the only fiber optics we can use in Aegis apparatus are those with specific treatments for reducing the solarization effect.

2.6 Conclusions

We have developed a laser system for positronium two step excitation to Rydberg levels. The first system for excitation from n=1 to 3, at 205 nm, should have an energy per pulse of $\sim 10\mu$J (for a 3 mm FWHM spot on positronium cloud) to saturate the transition for a large Doppler broadening and our system can generate 300 μJ of energy per pulse. The second transition (from n=3 to Rydberg levels) has a saturation energy of ~ 0.2 mJ and we obtained up to 3 mJ. The spectrum for the second transitions largely independent from the level we want to excite and is required to be larger than a nm, we produced 2 nm FWHM spectrum pulses. For both the transitions, thus, the energy and spectral feature we obtained are suitable for efficient positronium excitation and enough to compensate transport losses and unforeseen problem when the experiment will be performed at CERN. Both the system will be pumped by one laser source with harmonic generations, having the energy per pulse in fundamental, second and fourth harmonics needed by the systems. This pump allows to control each energy channel independently, thus further improving the generation of 205 nm radiation. We have many months of bureaucratic delay in obtaining this pump and at the moment of thesis writing it is going to be delivered.
We tested two different scheme for transport line. The first, based on mirrors and propagation into the vacuum, has low losses, but it has many disadvantages: the more important is that the possibility to adjust the position of the pulse inside the Aegis apparatus is limited and during the cooling down of the apparatus the mirrors can misalign due to different compression coefficients of the chamber components, a possible solution with piezoelectric goniometers is very expensive; other issues are that the system requires very high expertise to work with and the mirrors posed in ultrahigh vacuum and cold temperature aren't proofed to resist such environment. The second solution, based on silica multimode optical fiber, was tested with the two wavelengths and in a vacuum and cryogenic environment. The fiber for infrared transmission is suitable for transmission inside the Aegis apparatus, it has low losses only due to coupling of the radiation and can withstand the Aegis environment. The fiber for ultraviolet transmission can withstand the extreme

environment, but has an issues on energy transmission: due to solarization effect only a small number of fiber designed for ultraviolet transmission can efficiently carry radiation at 205 nm. We tested some fibers, finding one that can carry the radiation we needed with affordable losses, due to the fact that our production of ultraviolet radiation is large compared to the requirement on positronium excitation. The possible misalignment during cooling of the Aegis apparatus are low compared to the dimension of the pulses on positronium cloud. Another good point of this system is that the fibers and theirs feedthrough are cheap. We thus propose to use the fiber transport line for Aegis experiment.

Chapter 3

Theory of positronium excitation to Rydberg levels in magnetic field

While our goal is to obtain high amount of antihydrogen via a charge exchange process with positronium, there are few studies involving excited Ps in magnetic and/or electric fields, mainly for astrophysical or antimatter researches [29, 44, 45]. Positronium atoms are also a good test for many theories, mainly because:

- The Ps atom is very light (2 m_e, $\approx$ 1 MeV/c^2) compared to the lightest stable atom, hydrogen, (1 m_e + 1 m_P, $\approx$ 1 GeV/c^2) and effects related to the atom velocity, such as Doppler and motional Stark effects, are unusually high compared with.

- The Ps atom is composed by two elemental leptonic particles (an electron and a positron), bonded together by pure electromagnetic forces. The fine structure splitting of ground state is of about 203 GHz.

- The Ps atom spontaneously annihilate (in 125 ps for para-positronium, 142 ns for ortho-positronium in absence of external fields), while the hydrogen atom is stable

The potential that bind together the Ps atom is therefore a pure Coulombian potential, with eventual corrections due QED and relativistic effects. External fields can lightly mix the eigenstates of the previous effects, in case of low fields, and we can use the perturbative approach to calculate the degree of mixing of unperturbed engenstates, the new values for energy eigenvalues and matrix dipole elements between different states. The discussions and

results are presented in section 3.1. If the field are strong, as the 1T of magnetic field of Aegis, the requirement of small correction of the perturbative theory is no longer fulfilled. The chosen approach and results are discussed in section 3.2. In order to calculate the excitation efficiency for both low and high fields we have formulated a rate equation model under the assumption of a large laser spectrum, needed for the chosen excitation process; it is described in section 3.3. Section 3.4 summarizes the results from theory useful for develop a suitable laser system for positronium excitation and lists some other intriguing applications.

3.1 Positronium atom in weak magnetic fields

Moving Ps atoms in low fields are studied in [46, 47, 48, 49]. Those studies are essentially devoted to the investigation of the transition from the ground state to the first excited state (n=2), both theoretically and experimentally. The results are used in measurements of the fine structure splitting or for applications aiming to Ps laser cooling.
The Ps atom Hamiltonian H in a static field $\vec{B} = B_z\hat{z}$ can be described in a perturbative framework as:

$$\hat{H} = \hat{H}_C + \hat{H}_f + (\hat{H}_Z + \hat{H}_{dia} + \hat{H}_S) = \hat{H}_0 + \hat{H}_1 \tag{3.1}$$

where $\hat{H}_C$ is the Hamiltonian of a two-particle system with electric charge $+e$ and $-e$ at distance r interacting via the Coulomb potential $e^2/4\pi\varepsilon_0 r$; $\hat{H}_f$ represents the fine structure contribute (spin-orbit and spin-spin relativistic interaction); $\hat{H}_Z$ and $\hat{H}_{dia}$ represent the first order (Zeeman effect) and the second order (diamagnetic or quadratic Zeeman) interaction respectively with $\vec{B}$; $\hat{H}_S$ represents the contribution of the induced electric field (motional Stark effect) on the moving charges within the magnetic field. In this section the Stark effect is supposed enough weak to be considered as a small perturbation of the unperturbed Hamiltonian $\hat{H}_C$ and the diamagnetic effect is completely ignored because of its very small effect [32]. A more accurate treatment will be done in section 3.2.
Using the unperturbed atomic quantum numbers n, l, m and the total spin quantum numbers s, m_s, the energy level structure is given by [29]:

$$E_{n,l,m,s,m_s} = -\frac{\mu c^2 \alpha^2}{2n^2} + \Delta E_f(n,l,s) + \Delta E_Z(s,m_s) + \Delta E_S(n,l,m) \tag{3.2}$$

where μ is the reduced mass (equal to one half of electron mass) and α is the fine-structure constant. The first term (equal to -13.6 eV/$2n^2$) is a 4 n^2

degenerate manifold with respect to l, m, s, m_s substates and its energy levels are exactly equal to half the energy of the corresponding hydrogenic levels. We choose as the base of the perturbation the L-S coupling states, defined by the quantum numbers $|n, l, s, j, m>$, where n is the principal quantum number, l is the orbital momentum quantum number, s is the spin one, j is the total angular momentum quantum number and m is the quantum number of the projection of j on the quantization axis, chosen parallel to the direction of the external magnetic field. The states with $n = 3$ are listed in tables 3.1 - 3.2 and the states with $n = 1, 2$ can be founded in [46].

The unperturbed energy levels with QED correction up to $m\alpha^2$ [50], are defined as:

$$\begin{aligned} E(n,l,s,j) &= \tfrac{E_{ha}}{2n^2} + \tfrac{E_{ha}\alpha^2}{4n^3} + (1-\delta_{s,0})\,\delta_{l,0}\tfrac{E_{ha}\alpha^2}{4n^3}\tfrac{14}{3} + \\ &+ (1-\delta_{s,0})\,(1-\delta_{l,0})\,\tfrac{E_{ha}\alpha^2}{4n^3}\tfrac{1}{l(2l+1)(l+1)}\cdot \\ &\cdot\left(\delta_{j,l+1}\tfrac{l(3l+4)}{2l+3} - \delta_{j,l} - \delta_{j,l-1}\tfrac{(l+1)(3l-1)}{2l-1}\right) \end{aligned} \tag{3.3}$$

in which $E_{ha} = me^4/(4\pi\varepsilon_0\hbar)^2$ is the Hatree energy, 13.6 eV. The energy levels are graphically represented in fig. 3.1

$^1S_{0,0}$	$Y_{00}\chi_{0,0}$
$^1P_{1,1}$	$Y_{1,1}\chi_{0,0}$
$^1P_{1,0}$	$Y_{1,0}\chi_{0,0}$
$^1P_{1,-1}$	$Y_{1,-1}\chi_{0,0}$
$^1D_{2,2}$	$Y_{2,2}\chi_{0,0}$
$^1D_{2,1}$	$Y_{2,1}\chi_{0,0}$
$^1D_{2,0}$	$Y_{2,0}\chi_{0,0}$
$^1D_{2,-1}$	$Y_{2,-1}\chi_{0,0}$
$^1D_{2,-2}$	$Y_{2,-2}\chi_{0,0}$

Table 3.1: The first column lists the unperturbed singlet states. The second column lists the decomposition those states in spherical harmonic Y_{l,m_l} and spin function χ_{s,m_s}.

The eigenfunctions corrected to the first order of Ps atom are defined, as

$^3S_{1,1}$	$Y_{0,0}\chi_{1,1}$
$^3S_{1,0}$	$Y_{0,0}\chi_{1,0}$
$^3S_{1,-1}$	$Y_{0,0}\chi_{1,-1}$
$^3P_{0,0}$	$3^{-1/2}(Y_{1,1}\chi_{1,-1} - Y_{1,0}\chi_{1,0} + Y_{1,-1}\chi_{1,1})$
$^3P_{1,1}$	$2^{-1/2}(Y_{1,0}\chi_{1,1} - Y_{1,1}\chi_{1,0})$
$^3P_{1,0}$	$2^{-1/2}(Y_{1,-1}\chi_{1,1} - Y_{1,1}\chi_{1,-1})$
$^3P_{1,-1}$	$2^{-1/2}(Y_{1,-1}\chi_{1,0} - Y_{1,0}\chi_{1,-1})$
$^3P_{2,2}$	$Y_{1,1}\chi_{1,1}$
$^3P_{2,1}$	$2^{-1/2}(Y_{1,1}\chi_{1,0} + Y_{1,0}\chi_{1,1})$
$^3P_{2,0}$	$6^{-1/2}(Y_{1,1}\chi_{1,-1} + 4^{1/2}Y_{1,0}\chi_{1,0} + Y_{1,-1}\chi_{1,1})$
$^3P_{2,-1}$	$2^{-1/2}(Y_{1,-1}\chi_{1,0} + Y_{1,0}\chi_{1,-1})$
$^3P_{2,-2}$	$Y_{1,-1}\chi_{1,-1}$
$^3D_{1,1}$	$10^{-1/2}(Y_{2,0}\chi_{1,1} - 3^{1/2}Y_{2,1}\chi_{1,0} + 6^{1/2}Y_{2,2}\chi_{1,-1})$
$^3D_{1,0}$	$10^{-1/2}(3^{1/2}Y_{2,-1}\chi_{1,1} - 4^{1/2}Y_{2,0}\chi_{1,0} + 3^{1/2}Y_{2,1}\chi_{1,-1})$
$^3D_{1,-1}$	$10^{-1/2}(Y_{2,0}\chi_{1,-1} - 3^{1/2}Y_{2,-1}\chi_{1,0} + 6^{1/2}Y_{2,-2}\chi_{1,1})$
$^3D_{2,2}$	$3^{-1/2}(Y_{2,1}\chi_{1,1} - 2^{1/2}Y_{2,2}\chi_{1,0})$
$^3D_{2,1}$	$6^{-1/2}(-2^{1/2}Y_{2,2}\chi_{1,-1} - Y_{2,1}\chi_{1,0} + 3^{1/2}Y_{2,0}\chi_{1,1})$
$^3D_{2,0}$	$2^{-1/2}(Y_{2,-1}\chi_{1,1} - Y_{2,1}\chi_{1,-1})$
$^3D_{2,-1}$	$6^{-1/2}(2^{1/2}Y_{2,-2}\chi_{1,1} + Y_{2,-1}\chi_{1,0} - 3^{1/2}Y_{2,0}\chi_{1,-1})$
$^3D_{2,-2}$	$3^{-1/2}(2^{1/2}Y_{2,-2}\chi_{1,0} - Y_{2,-1}\chi_{1,-1})$
$^3D_{3,3}$	$Y_{2,2}\chi_{1,1}$
$^3D_{3,2}$	$3^{-1/2}(2^{1/2}Y_{2,1}\chi_{1,1} + Y_{2,2}\chi_{1,0})$
$^3D_{3,1}$	$15^{-1/2}(Y_{2,2}\chi_{1,-1} + 8^{1/2}Y_{2,1}\chi_{1,0} + 6^{1/2}Y_{2,0}\chi_{1,1})$
$^3D_{3,0}$	$5^{-1/2}(Y_{2,1}\chi_{1,-1} + 3^{1/2}Y_{2,0}\chi_{1,0} + Y_{2,-1}\chi_{1,1})$
$^3D_{3,-1}$	$15^{-1/2}(Y_{2,-2}\chi_{1,1} + 8^{1/2}Y_{2,-1}\chi_{1,0} + 6^{1/2}Y_{2,0}\chi_{1,-1})$
$^3D_{3,-2}$	$3^{-1/2}(2^{1/2}Y_{2,-1}\chi_{1,-1} + Y_{2,-2}\chi_{1,0})$
$^3D_{3,-3}$	$Y_{2,-2}\chi_{1,-1}$

Table 3.2: The first column lists the unperturbed triplet states. The second column lists the decomposition of those states in spherical harmonic $Y_{l,ml}$ and spin function $\chi_{s,sm}$.

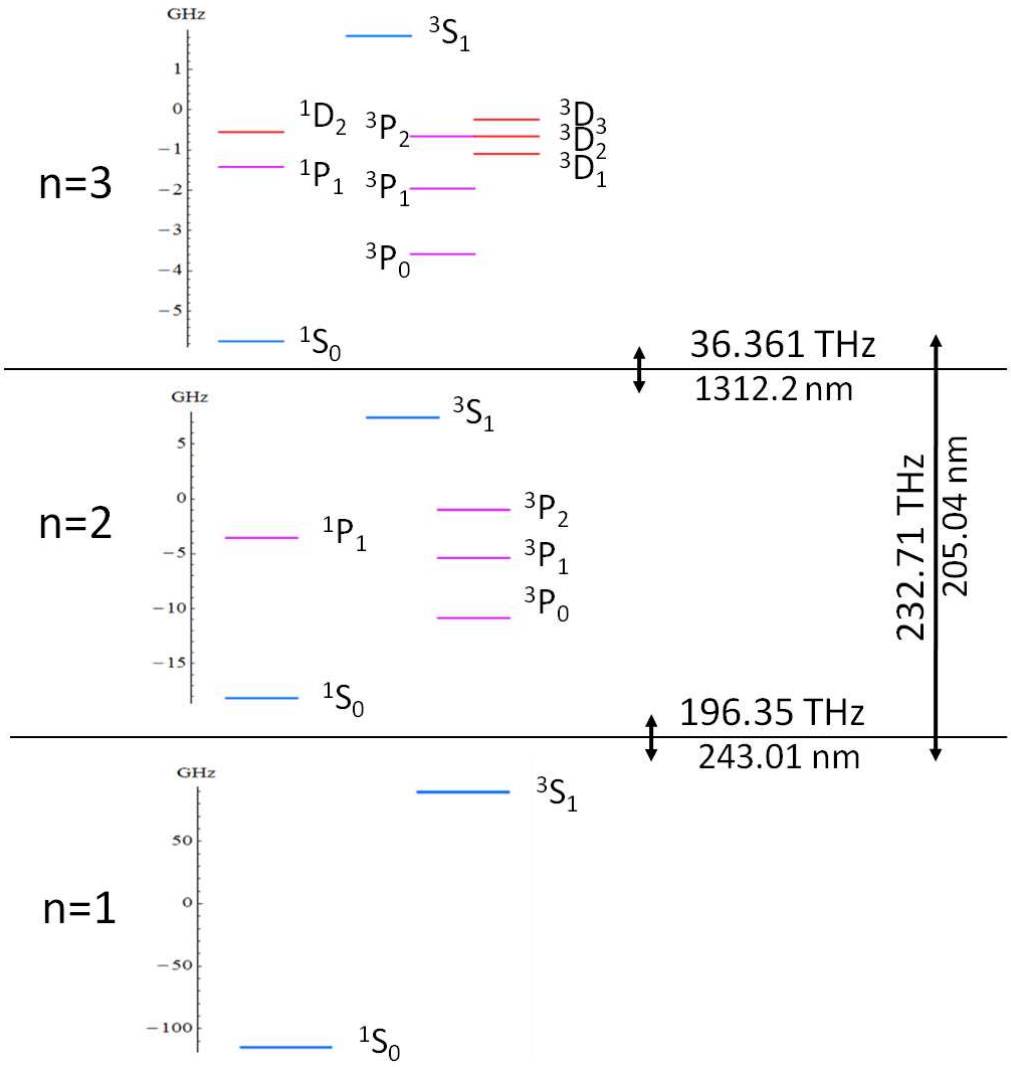

Figure 3.1: Fine structure splitting of the first 3 n–levels of Ps in zero external fields

usual in case of nondegenerate states [51], as:

$$|\tilde{\psi}>=|\psi>-\sum_{\psi'\neq\psi}\frac{|\psi'><\psi'|H_1|\psi>}{E_{\psi'}-E_{\psi}} \tag{3.4}$$

where E_ψ are the unperturbed energy
As you can see form fig 3.1, a special case is presented for $n = 3$. In fact there are two energy degenerate state families, namely 3^3P_2 and 3^3D_2. This requires the *degenerate perturbation theory* [51]: the state with different energy eigenvalues are calculated as before (excluding the degenerate states from the sums), while the degenerate states require a matrix diagonalization, similar to the full matrix diagonalization required by strong field.

$^1S_{0,0}$	$^1S_{0,0} - 2\ \varepsilon_z\ ^3S_{1,0} + 3\sqrt{3}\ \varepsilon_\perp\ ^1P_{1,-1} + 3\sqrt{6}\ \varepsilon_\parallel\ ^1P_{1,0} - 3\sqrt{3}\ \varepsilon_\perp\ ^1P_{1,1}$
$^1P_{1,1}$	$^1P_{1,1} + 3\sqrt{3}\ \varepsilon_\perp\ ^1S_{0,0} - \sqrt{2}\ \varepsilon_z\ ^3P_{1,1} + \frac{9}{2}\ \varepsilon_\perp\ ^1D_{2,2} - \frac{9}{2}\ \varepsilon_\parallel\ ^1D_{2,1} - \left(\frac{3}{2}\right)^{3/2}$ $\varepsilon_\perp\ ^1D_{2,0}$
$^1P_{1,0}$	$^1P_{1,0} - 3\sqrt{6}\ \varepsilon_\parallel\ ^1S_{0,0} - \frac{2}{\sqrt{3}}\ \varepsilon_z\ ^3P_{0,0} - \frac{9}{2\sqrt{2}}\ \varepsilon_\perp\ ^1D_{2,-1} - 3\sqrt{3}\ \varepsilon_\parallel\ ^1D_{2,0} + \frac{9}{2\sqrt{2}}$ $\varepsilon_\perp\ ^1D_{2,1}$
$^1P_{1,-1}$	$^1P_{1,-1} - 3\sqrt{3}\ \varepsilon_\perp\ ^1S_{0,0} + \sqrt{2}\ \varepsilon_z\ ^3P_{1,-1} - \frac{9}{2}\ \varepsilon_\perp\ ^1D_{2,-2} - \frac{9}{2}\ \varepsilon_\parallel\ ^1D_{2,-1} + \left(\frac{3}{2}\right)^{3/2}$ $\varepsilon_\perp\ ^1D_{2,0}$
$^1D_{2,2}$	$^1D_{2,2} - \frac{9}{2}\ \varepsilon_\perp\ ^1P_{1,1} - \frac{2}{\sqrt{3}}\ \varepsilon_z\ ^3D_{3,2}$
$^1D_{2,1}$	$^1D_{2,1} + \frac{9}{2}\ \varepsilon_\parallel\ ^1P_{1,1} - \frac{9}{2\sqrt{2}}\ \varepsilon_\perp\ ^1P_{1,0} - \sqrt{\frac{6}{5}}\ \varepsilon_z\ ^3D_{1,1} - 4\sqrt{\frac{2}{15}}\ \varepsilon_z\ ^3D_{3,1}$
$^1D_{2,0}$	$^1D_{2,0} - \left(\frac{3}{2}\right)^{\frac{3}{2}}\ \varepsilon_\perp\ ^1P_{1,-1} + 3\sqrt{3}\ \varepsilon_\parallel\ ^1P_{1,0} - \left(\frac{3}{2}\right)^{\frac{3}{2}}\ \varepsilon_\perp\ ^1P_{1,1} - 2\sqrt{\frac{2}{5}}\ \varepsilon_z\ ^3D_{1,0}$ $-2\sqrt{\frac{3}{5}}\ \varepsilon_z\ ^3D_{3,0}$
$^1D_{2,-1}$	$^1D_{2,-1} + \frac{9}{2}\ \varepsilon_\parallel\ ^1P_{1,-1} + \frac{9}{2\sqrt{2}}\ \varepsilon_\perp\ ^1P_{1,0} - \sqrt{\frac{6}{5}}\ \varepsilon_z\ ^3D_{1,-1} - 4\sqrt{\frac{2}{15}}\ \varepsilon_z\ ^3D_{3,-1}$
$^1D_{2,-2}$	$^1D_{2,-2} + \frac{9}{2}\ \varepsilon_\perp\ ^1P_{1,-1} - \frac{2}{\sqrt{3}}\ \varepsilon_z\ ^3D_{3,-2}$

Table 3.3: In the first column the unperturbed singlet states are listed. The second column lists the perturbed states for nondegenerate levels. The coefficients are: $\varepsilon_z = \mu_B\ B\ /\ \Delta E_{1,2}$, $\varepsilon_\perp = 2\ a_0\ e\ E_\perp\ /\ \Delta E_{1,2}$, $\varepsilon_\parallel = 2\ a_0\ e\ E_\parallel\ /\ \Delta E_{1,2}$.

In order to solve the problem in the subspace of energy degenerate 3^3P_2 and 3^3D_2 states, we use a linear combination of unperturbed degenerate states $|\psi_k>=\sum c_k|n,l,s,j,m>_{deg}$ with two characteristics:

${}^3S_{1,1}$	${}^3S_{1,1} - 3\ \varepsilon_\perp\ {}^3P_{0,0} - 3\sqrt{3}\ \varepsilon_\parallel\ {}^3P_{1,1} - 3\sqrt{\frac{3}{2}}\ \varepsilon_\perp\ {}^3P_{1,0}$
${}^3S_{1,0}$	${}^3S_{1,0} + 2\ \varepsilon_z\ {}^1S_{0,0} + 3\sqrt{2}\ \varepsilon_\parallel\ {}^3P_{0,0} - 3\sqrt{\frac{3}{2}}\ \varepsilon_\perp\ {}^3P_{1,-1} - 3\sqrt{\frac{3}{2}}\ \varepsilon_\perp\ {}^3P_{1,1}$
${}^3S_{1,-1}$	${}^3S_{1,-1} + 3\ \varepsilon_\perp\ {}^3P_{0,0} + 3\sqrt{3}\ \varepsilon_\parallel\ {}^3P_{1,-1} - 3\sqrt{\frac{3}{2}}\ \varepsilon_\perp\ {}^3P_{1,0}$
${}^3P_{0,0}$	${}^3P_{0,0} - 3\ \varepsilon_\perp\ {}^3S_{1,-1} - 3\sqrt{2}\ \varepsilon_\parallel\ {}^3S_{1,0} + 3\ \varepsilon_\perp\ {}^3S_{1,1} + \frac{2}{\sqrt{3}}\ \varepsilon_z\ {}^1P_{1,0} - \frac{3\sqrt{5}}{2}\ \varepsilon_\perp$ ${}^3D_{1,-1} \quad -3\sqrt{\frac{5}{2}}\ \varepsilon_\parallel\ {}^3D_{1,0} - \frac{3\sqrt{5}}{2}\ \varepsilon_\perp\ {}^3D_{1,1}$
${}^3P_{1,1}$	${}^3P_{1,1} + 3\sqrt{3}\ \varepsilon_\parallel\ {}^3S_{1,1} + 3\sqrt{\frac{3}{2}}\ \varepsilon_\perp\ {}^3S_{1,0} + \sqrt{2}\ \varepsilon_z\ {}^1P_{1,1} - 3\frac{\sqrt{15/2}}{4}\ \varepsilon_\perp\ {}^3D_{1,0}$ $-\frac{3\sqrt{15}}{4}\ \varepsilon_\parallel\ {}^3D_{1,1}$
${}^3P_{1,0}$	${}^3P_{1,0} + 3\sqrt{\frac{3}{2}}\ \varepsilon_\perp\ {}^3S_{1,-1} + 3\sqrt{\frac{3}{2}}\ \varepsilon_\perp\ {}^3S_{1,1} - 3\frac{\sqrt{15/2}}{4}\ \varepsilon_\perp\ {}^3D_{1,1} - 3\frac{\sqrt{15/2}}{4}\ \varepsilon_\perp$ ${}^3D_{1,-1}$
${}^3P_{1,-1}$	${}^3P_{1,-1} - 3\sqrt{3}\ \varepsilon_\parallel\ {}^3S_{1,-1} + 3\sqrt{\frac{3}{2}}\ \varepsilon_\perp\ {}^3S_{1,0} - \sqrt{2}\ \varepsilon_z\ {}^1P_{1,-1} - 3\frac{\sqrt{15/2}}{4}\ \varepsilon_\perp\ {}^3D_{1,0}$ $+\frac{3\sqrt{15}}{4}\ \varepsilon_\parallel\ {}^3D_{1,-1}$
${}^3D_{1,1}$	${}^3D_{1,1} - \frac{3\sqrt{5}}{2}\ \varepsilon_\perp\ {}^3P_{0,0} + \frac{3\sqrt{15}}{4}\ \varepsilon_\parallel\ {}^3P_{1,1} + \frac{3\sqrt{15}}{4\sqrt{2}}\ \varepsilon_\perp\ {}^3P_{1,0} + \sqrt{\frac{6}{5}}\ \varepsilon_z\ {}^1D_{2,1}$
${}^3D_{1,0}$	${}^3D_{1,0} + 3\sqrt{\frac{5}{2}}\ \varepsilon_\parallel\ {}^3P_{0,0} + \frac{3\sqrt{15}}{4\sqrt{2}}\ \varepsilon_\perp\ {}^3P_{1,-1} + \frac{3\sqrt{15}}{4\sqrt{2}}\ \varepsilon_\perp\ {}^3P_{1,1} + 2\sqrt{\frac{2}{5}}\ \varepsilon_z\ {}^1D_{2,0}$
${}^3D_{1,-1}$	${}^3D_{1,-1} + \frac{3\sqrt{5}}{2}\ \varepsilon_\perp\ {}^3P_{0,0} - \frac{3\sqrt{15}}{4}\ \varepsilon_\parallel\ {}^3P_{1,-1} + \frac{3\sqrt{15}}{4\sqrt{2}}\ \varepsilon_\perp\ {}^3P_{1,0} + \sqrt{\frac{6}{5}}\ \varepsilon_z\ {}^1D_{2,-1}$
${}^3D_{3,3}$	${}^3D_{3,3}$
${}^3D_{3,2}$	${}^3D_{3,2} + \frac{2}{\sqrt{3}}\ \varepsilon_z\ {}^1D_{2,2}$
${}^3D_{3,1}$	${}^3D_{3,0} + 4\sqrt{\frac{2}{15}}\ \varepsilon_z\ {}^1D_{2,1}$
${}^3D_{3,0}$	${}^3D_{3,0} + 2\sqrt{\frac{3}{5}}\ \varepsilon_z\ {}^1D_{2,0}$
${}^3D_{3,-1}$	${}^3D_{3,-1} + 4\sqrt{\frac{2}{15}}\ \varepsilon_z\ {}^1D_{2,-1}$
${}^3D_{3,-2}$	${}^3D_{3,-2} + \frac{2}{\sqrt{3}}\ \varepsilon_z\ {}^1D_{2,-2}$
${}^3D_{3,-3}$	${}^3D_{3,-3}$

Table 3.4: In the first column the unperturbed triplet states are listed. The second column lists the perturbed states for nondegenerate levels. The coefficients are: $\varepsilon_z = \mu_B\ B\ /\ \Delta E_{1,2}$, $\varepsilon_\perp = 2\ a_0\ e\ E_\perp\ /\ \Delta E_{1,2}$, $\varepsilon_\parallel = 2\ a_0\ e\ E_\parallel\ /\ \Delta E_{1,2}$.

- the new states are an orthonormal base in this subspace
- the new states are eigenstates of both the unperturbed Hamiltonian and the perturbation Hamiltonian $H_0 + H_1|\psi_k >= E + E'|\psi_k >$

The coefficients of the new states c_k can be derived diagonalizing the matrix of the values of the perturbation Hamiltonian on the degenerate states, whose element is $_{deg} < n, l, s, j, m|\ H_1\ |n_1, l_1, s_1, j_1, m_1 >_{deg}$. In our case the elements coupled by the perturbation are those with $|\Delta l| = 1$ and $|\Delta m| = 0$ for electric field parallel to the magnetic field or $|\Delta m| = 1$ for electric field perpendicular to the magnetic field, including the motional induced electric field.

The perturbed states, for the case of nondegenerate states, are reported in table 3.4, while the linear combinations of degenerate states depend upon the relative strength of the electric field parallel or perpendicular to the magnetic field. In the particular case of absence of parallel field the values are reported in table 3.5

3.2 Positronium atoms moving in high magnetic field

In strong magnetic field the perturbation theory fail to predict the correct energies and coefficients for the highly mixed wave functions due to the strength of the interaction. The high velocity that positronium usually has in the laboratory reference, due to its small mass, can also originate an induced electric field strong enough to go beyond perturbation theory, so a non perturbative theory of crossed electric and magnetic fields on positronium is required.

3.2.1 Zeeman effects and fine structure contributes

The expression for the fine-structure sublevel energy splitting ΔE_f (eq. 3.3) can be found, in example, in ref [50]. This energy contribution is about α^2/n times less than the unperturbed energy and turns out to be small with respect to 1 Tesla magnetic contributions from $n \geq 3$. Its value for $n = 1, 2$ is well known both theoretically [52, 53] and experimentally [52, 53]. In order to calculate the magnitude of linear Zeeman splitting, we define as usual the magnetic dipole moment to angular momentum ($\vec{L}$) and spin ($\vec{S}$) for electron and positron as $\vec{\mu}_{L,e^+,e^-} = \pm(e/2m_e)\vec{L}_{e^+,e^-}$ and $\vec{\mu}_{S,e^+,e^-} = \pm(e/m_e)\vec{S}_{e^+,e^-}$, where m_e is the electron mass and the gyromagnetic factors are assumed

	$^3P_{2,-2}$	$^3P_{2,-1}$	$^3P_{2,0}$	$^3P_{2,1}$	$^3P_{2,2}$	$^3D_{2,-2}$	$^3D_{2,-1}$	$^3D_{2,0}$	$^3D_{2,1}$	$^3D_{2,2}$
ψ_1	$\frac{1}{4}$		$\sqrt{\frac{3}{8}}$		$\frac{1}{4}$		$-\frac{1}{2}$		$-\frac{1}{2}$	
ψ_2		$-\frac{1}{2}$		$-\frac{1}{2}$		$\frac{1}{4}$		$\sqrt{\frac{3}{8}}$		$\frac{1}{4}$
ψ_3	$\frac{1}{4}$		$\sqrt{\frac{3}{8}}$		$\frac{1}{4}$		$\frac{1}{2}$		$\frac{1}{2}$	
ψ_4		$\frac{1}{2}$		$\frac{1}{2}$		$\frac{1}{4}$		$\sqrt{\frac{3}{8}}$		$\frac{1}{4}$
ψ_5	$\frac{1}{2}$				$-\frac{1}{2}$		$-\frac{1}{2}$		$\frac{1}{2}$	
ψ_6		$-\frac{1}{2}$		$\frac{1}{2}$		$\frac{1}{2}$				$-\frac{1}{2}$
ψ_7	$-\frac{1}{2}$				$\frac{1}{2}$		$-\frac{1}{2}$		$\frac{1}{2}$	
ψ_8		$-\frac{1}{2}$		$\frac{1}{2}$		$-\frac{1}{2}$				$\frac{1}{2}$
ψ_9	$\sqrt{\frac{3}{8}}$		$-\frac{1}{2}$		$\sqrt{\frac{3}{8}}$					
ψ_{10}						$\sqrt{\frac{3}{8}}$		$-\frac{1}{2}$		$\sqrt{\frac{3}{8}}$

Table 3.5: Decomposition of degenerate sublevels, as described in section 3.1, in the important case of an electric field perpendicular to the quantization axis. This condition is realized when we consider a moving Ps in a static magnetic field, directed along the quantization axis, due to electromagnetic induced field on the moving charged particles. The matrix elements are the coefficients c_i for each new wavefunction ψ_k in the L-S base of the energy degenerate subspace.

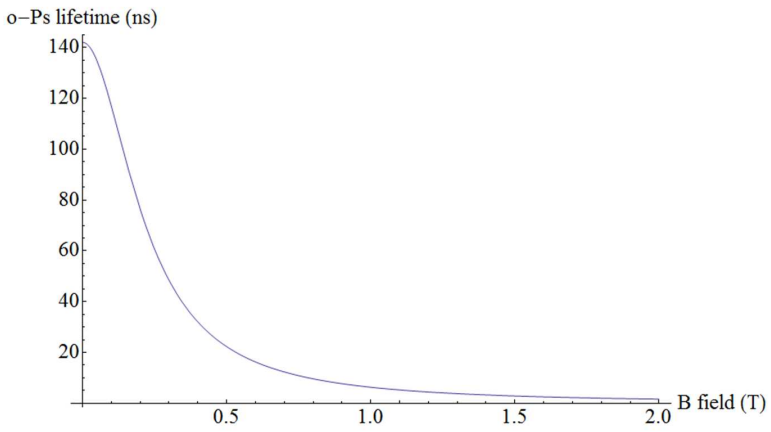

Figure 3.2: Half life of $m_s = 0$ ortho-positronium in magnetic field

to be exactly 2. The explicit expression of the linear Zeeman Hamiltonian comes out to be:

$$\hat{H}_Z = -(\vec{\mu}_{L,e^+} + \vec{\mu}_{L,e^-} + \vec{\mu}_{S,e^+} + \vec{\mu}_{S,e^-}) \cdot \vec{B} = 2\mu_B B(S^z_{e^-} - S^z_{e^+})/\hbar \quad (3.5)$$

where $\mu_B = e\hbar/2m_e$ is the Bohr magneton. Because $\vec{L}_{e^+} = \vec{L}_{e^-}$, in the center of mass system, there isn't energy contribution from magnetic interaction with orbital motion.
The matrix element $\langle \chi_{s',m'_s} | S^z_{e^-} - S^z_{e^+} | \chi_{s,m_s} \rangle$, where$\chi_{s,m_s}$ are the spin wavefunctions, is nonzero only when $m'_s = m_s = 0$ and $s \neq s'$ because the $z-$component spin $\hat{H}_Z$ is not diagonal in the singlet and triplet basis of Ps states [18]. Hence, the magnetic perturbation mixes ortho and paraPs states with $m_s = 0$ and its maximum value can be evaluated as $\Delta E_Z = 4\mu_B B$. For 1T of magnetic field this value is 2.4×10^{-4} eV (58 GHz). The matrix element is evaluated using the Wigner 3J and 6J symbols, resulting in [46]:

$$\begin{aligned} \langle \psi_{n',l',s',j',m'} | H_z | \psi_{n,l,s,j,m} \rangle = \; & \delta_{n,n'}\delta_{l,l'}\delta_{m,m'}(-1)^{l+m}[(-1)^{s+s'} - 1] \cdot \\ & \cdot \begin{pmatrix} j' & 1 & j \\ -m & 0 & m \end{pmatrix} \begin{Bmatrix} s' & l' & j' \\ j & 1 & s \end{Bmatrix} \cdot \\ & \cdot \sqrt{3(2j'+1)(2j+1)}\mu_B B \end{aligned} \quad (3.6)$$

This level mixing leads to the well known enhancement of the average annihilation rate of the Ps thermal ground state $n = 1$, called magnetic quenching [52, 18]. The Ps surviving long enough to be excited will be the orthopositronium with $m_s \pm 1$. Figure 3.2 shows the o-Ps $m_s = 0$ lifetime in function of the external magnetic field, calculated as in [18].

The Hamiltonian for quadratic Zeeman effect is $\hat{H}_{dia} = (e^2/8\mu)(\vec{r} \times \vec{B})^2$ and has nonzero matrix elements if $\Delta l = 0, \pm 2$ for every Δn; its effect is the mixing of n, l levels for very intense magnetic field (greater than 100 T). For less intense fields its contribute to the energy levels turns out to be $\Delta E_{dia} = \langle \psi_{n,l,s,j,m} | \hat{H}_{dia} | \psi_{n',l',s',j',m'} \rangle = (e^2 B^2 a_{Ps}^2/8\mu) \cdot f(n,l,m)$, where a_{Ps} is the Ps Bohr radius ($a_{Ps} = 2a_0$). The factor $f(n,l,m)$ is a sum of a n-dependent positive contribute and a l-m splitting term, both proportional to n^4 [54]. Those contributions are important only for high n levels, greater than $n = 40$, but in this region there is also an high enhancement in ionization probability due to the motional Stark effect, as described in the following section. Therefore we don't consider this interaction term in the following calculations.

3.2.2 Motional Stark effect

The motional Stark effect arises because of induced electric field on moving charges in magnetic field. Because of the very light mass of the Ps atom, this effect becomes the dominant broadening for Rydberg levels. Using an approximate approach in order to find the energy contribution of this effect, it is useful to consider the Ps in the reference frame where it is at rest. If the Ps center of mass is moving with velocity $\vec{v}_{CM}$ in a static $\vec{B}$ field, we can transform the fields in the frame of the center of mass reference:

$$\vec{B} = \vec{B} \tag{3.7}$$

$$\vec{E} = \vec{v}_{CM} \times \vec{B} = \vec{E}_{\perp} \tag{3.8}$$

This induced electric field generates a Stark splitting of the Ps sublevels. The relative Hamiltonian is [49, 46]:

$$\hat{H}_{MS} = -e\vec{r} \cdot \vec{E}_{\perp} = -e\vec{r} \cdot (\vec{v}_{CM} \times \vec{B}) \tag{3.9}$$

This formula can also be derived, with some assumptions, from a more formal analysis of the problem of two electric charged particles moving in arbitrary magnetic field [55]. The matrix element for Stark effect is [46]:

$$\begin{aligned} \langle \psi_{n',l',s',j',m'} | H_M S | \psi_{n,l,s,j,m} \rangle = \delta_{s,s'} (-1)^{s+m'+1} \, e \, (n',l'|r|n,l) \cdot \\ \cdot \begin{Bmatrix} s' & l' & j' \\ 1 & j & l \end{Bmatrix} \sqrt{\max(l,l') \cdot (2J'+1)(2j+1)/2} \cdot \\ \cdot \sum_q \tau_q \begin{pmatrix} j' & 1 & j \\ -m & q & m \end{pmatrix} \end{aligned} \tag{3.10}$$

where $(n', l'|r|n, l)$ is the radial matrix element and τ is a vector with spherical components $\tau_{\pm 1} = \pm\epsilon_\perp$, $\tau_0 = -\sqrt{2}\epsilon_\parallel$ and ϵ is the electric field, parallel or perpendicular to the magnetic field. The motional induced field, for example, is always perpendicular to magnetic field, while external electric field can be added with electrodes or charged surfaces. The radial matrix elements are calculated following the standard hydrogen-like Coulomb potential [51] and result [56]:

$$(n, l'|r|n, l) = \frac{(-1)^{l+l'}}{2n}(2a_0)(n/2)\sqrt{\frac{(n-l'-1)!(n+l')!}{(n-l-1)!(n+l)!}} \cdot \cdot \sum_{j=0}^{n-l'-1} \frac{(-1)^j(n+1-l-j)!(n+2+l-j)!}{j!(n-l'-1-j)!(n+l'-j)!(2-j)!} \tag{3.11}$$

where $2a_0$ is the Bohr radius of the positronium.
The maximum energy splitting ΔE_{MS} between the n^2 sublevels of a opened n-fan can be estimated from the Stark effect theory, obtaining:

$$\Delta E_{MS} = 3ea_{Ps}n(n-1)|\vec{E}_\perp| = 3ea_{Ps}n(n-1)Bv_\perp \tag{3.12}$$

where $v_\perp$ can be taken as $\sqrt{k_B T/m_e}$, the most probable transverse component of the thermal velocity of the Ps center-of-mass. This splitting effect becomes relevant on Ps atoms even for small n values and largely predominant on Rydberg levels in the working condition of the Aegis experiment. Values of the motional Stark splitting are 12.6 GHz for n=3, 800 GHz for n=20, 1800 GHz for n=30 for 1 T magnetic field and thermal velocity corresponding to 100 K. It is useful to consider that , for the excitation to the Rydberg levels, the energy splitting between adjacent unperturbed n levels (with an energy of -13.6 eV $/2n^2$) is:

$$\Delta E_n \approx \frac{13.6eV}{n^3} \tag{3.13}$$

thus the splitting between two adjacent levels become smaller than the maximum motional Stark splitting from $n = 17$. The consequence is an interleaving of levels that, considering a cloud of positronium atoms with thermal distribution of velocity, the laser pulses see Rydberg states as a band rather than separate discrete levels. Some details about this effect are discussed further in the thesis.
Another consideration linked to the motional Stark splitting of the energy levels is the possible ionization of the Ps atoms. The transition from the bound state to the ionized one starts to occur from the bottom sublevel of

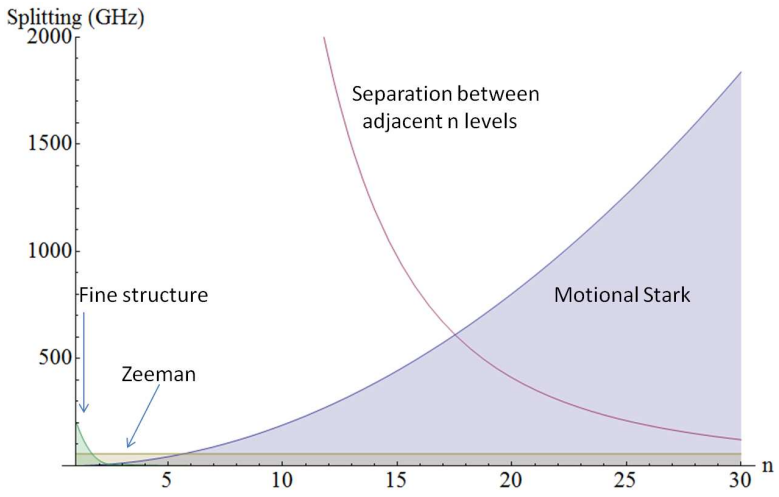

Figure 3.3: Maximum energy splitting (in GHz) due to fine structure, Zeeman effect and motional Stark effect for 1 T magnetic field and 100 K thermal Ps velocity

the n-fan (the *red states*, [57]). This effect limits the excitation efficiency for high Rydberg levels, determining an upper level to consider for ours experiment. The minimum Stark electric field that induce a ionization probability can be estimated to be [57]:

$$|\vec{E}_{min}| = \frac{e}{144\pi\varepsilon_0 a_0^2}\frac{1}{n^4} \tag{3.14}$$

Thus, for the reference conditions of the Aegis experiment (B=1 T, T=100K) the ionization stats affecting some sublevels from $n = 27$.
Figure 3.3 reassumes the maximum splitting contribution to positronium levels due to fine structure, Zeeman and motional Stark effects up to level 30.

3.2.3 Eigenfunctions and Eigenvalues in strong field for n = 2 and 3

In order to study theoretically the positronium excitation, we need to calculate the dipole elements between positronium levels. The perturbation theory can no longer be used with strong interaction, so we need to calculate the eigenfunctions numerically, by full diagonalization of the interaction matrix. We can start from the matrix of the energy values of the unperturbed positronium: the base chosen is the L-S coupled states, so the diagonal elements are the energy values in absence of external fields. The off diagonal

elements are calculated with the Zeeman and Stark Hamiltonians because the interaction elements aren't diagonal in this base. An example of this matrix for n=2 can be found in table 3.6 for 1T of magnetic field and a Motional Stark induced by a $5km/s$ velocity, approximately the most probable in the Aegis Ps transverse velocity distribution. The eigenvalues of the interaction matrix are the new energy values in presence of electric or magnetic fields, while the eigenvectors give the coefficients of the decomposition of the new eigenfuncions over the L-S coupling base. Using those decompositions we can calculate the perturbed states using the well known dipole matrix elements for transition between L-S states.

We wrote a Mathematica program in order to numerically diagonalize the interaction matrix. With a standard pc the matrix can be evaluated in short times (less than half an hour) up to level with $n = 5$ and in a couple of minutes for levels $n = 1 - 3$. We can extract from this code how the eigenvalues are modified by electric and magnetic fields, as reported in fig. 3.5. Reference [49] reports the eigenvalues evaluated for n=2 level for different positronium velocity and magnetic field using calculation techniques similar to what we used. The results from our full diagonalizing program is the same found in ref. [49] (fig. 3.4).

From fig. 3.5 it is possible to see the Paschen-Bach effect of magnetic field for n=2 level. In n=1 level the 1T magnetic field is low enough to be considered a small perturbation, while in n=3 level the motional Stark effect became of the same magnitude of the magnetic splitting, showing an high degree of sublevel mixing.

It is worth note that the levels cross together exactly in presence of pure Coulombian potential. In presence of the perturbation effects there are an anticrossing effect between some levels [49]. The strength of the anticrossing depend on the relative intensity of magnetic and electric field.

3.3 Excitation model from n = 1 to n = 2 or 3

Due to the very light mass of Ps, the level transitions are broader than in the usual atomic spectroscopy due to Doppler effect, so the laser excitation must be accordingly broad or it needs special techniques of "Doppler free" excitation [47]. In Aegis, due to the requirement of efficient excitation of the whole positronium cloud, we have chosen a laser system finalized to a broad excitation. The broad laser linewidths come along with a coherence time

	2,0,0,0,0	2,0,1,1,-1	2,0,1,1,0	2,0,1,1,1	2,1,0,1,-1	2,1,0,1,0	2,1,0,1,1	2,1,1,0,0
2,0,0,0,0	-18.1	0	-28.0	0	0.271	0	-0.271	0
2,0,1,1,-1	0	7.41	0	0	0	0	0	-0.157
2,0,1,1,0	-28.0	0	7.41	0	0	0	0	0
2,0,1,1,1	0	0	0	7.41	0	0	0	0.157
2,1,0,1,-1	0.271	0	0	0	-3.54	0	0	0
2,1,0,1,0	0	0	0	0	0	-3.54	0	16.2
2,1,0,1,1	-0.271	0	0	0	0	0	-3.54	0
2,1,1,0,0	0	-0.157	0	0.157	0	16.2	0	-10.8
2,1,1,1,-1	0	0	0.192	0	-19.8	0	0	0
2,1,1,1,0	0	0.192	0	0.192	0	0	0	0
2,1,1,1,1	0	0	0.192	0	0	0	19.8	0
2,1,1,2,-2	0	0.271	0	0	0	0	0	0
2,1,1,2,-1	0	0	0.192	0	-19.8	0	0	0
2,1,1,2,0	0	-0.111	0	0.111	0	-22.9	0	0
2,1,1,2,1	0	0	-0.192	0	0	0	-19.8	0
2,1,1,2,2	0	0	0	-0.271	0	0	0	0

	2,1,1,1,-1	2,1,1,1,0	2,1,1,1,1	2,1,1,2,-2	2,1,1,2,-1	2,1,1,2,0	2,1,1,2,1	2,1,1,2,2
2,0,0,0,0	0	0	0	0	0	0	0	0
2,0,1,1,-1	0	0.192	0	0.271	0	-0.111	0	0
2,0,1,1,0	0.192	0	0.192	0	0.192	0	-0.192	0
2,0,1,1,1	0	0.192	0	0	0	0.111	0	-0.271
2,1,0,1,-1	-19.8	0	0	0	-19.8	0	0	0
2,1,0,1,0	0	0	0	0	0	-22.9	0	0
2,1,0,1,1	0	0	19.8	0	0	0	-19.8	0
2,1,1,0,0	0	0	0	0	0	0	0	0
2,1,1,1,-1	-5.36	0	0	0	0	0	0	0
2,1,1,1,0	0	-5.36	0	0	0	0	0	0
2,1,1,1,1	0	0	-5.36	0	0	0	0	0
2,1,1,2,-2	0	0	0	-0.981	0	0	0	0
2,1,1,2,-1	0	0	0	0	-0.981	0	0	0
2,1,1,2,0	0	0	0	0	0	-0.981	0	0
2,1,1,2,1	0	0	0	0	0	0	-0.981	0
2,1,1,2,2	0	0	0	0	0	0	0	-0.981

Table 3.6: In the first row and column are listed the unperturbed states. These states are decomposed by their quantum number, following the scheme (n,l,s,j,m). The nonzero values are calculated in GHz from the reference $13.6eV/2n^2$ of the Coulomb potential: the diagonal values account for the S-L coupling, while off diagonal contain Zeeman and Motional Stark contribution for 1T of magnetic field and a transverse velocity of $5km/s$

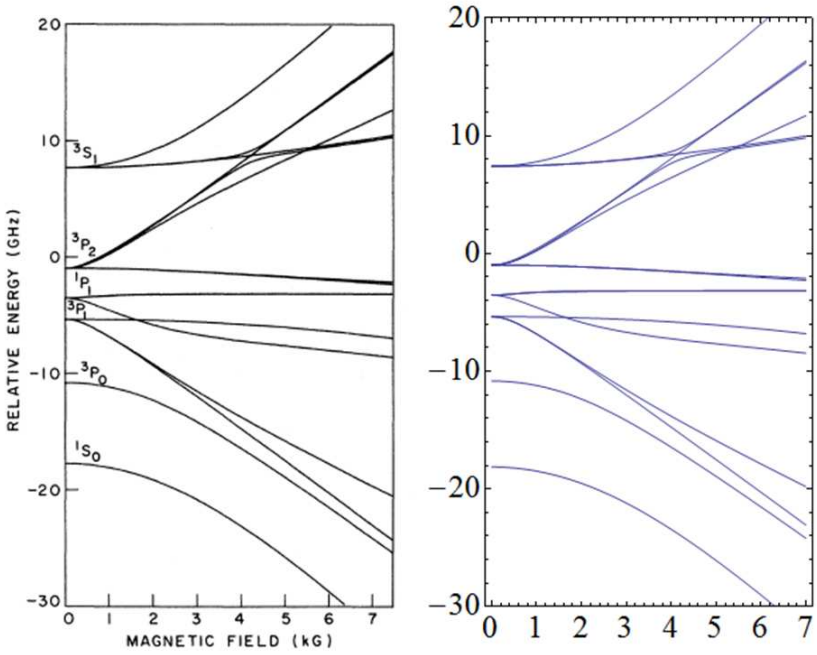

Figure 3.4: Splitting of sublevels of n=2 in magnetic field and for the Ps velocity of 10^4 from our calculation (right) and form ref. [49] (left).

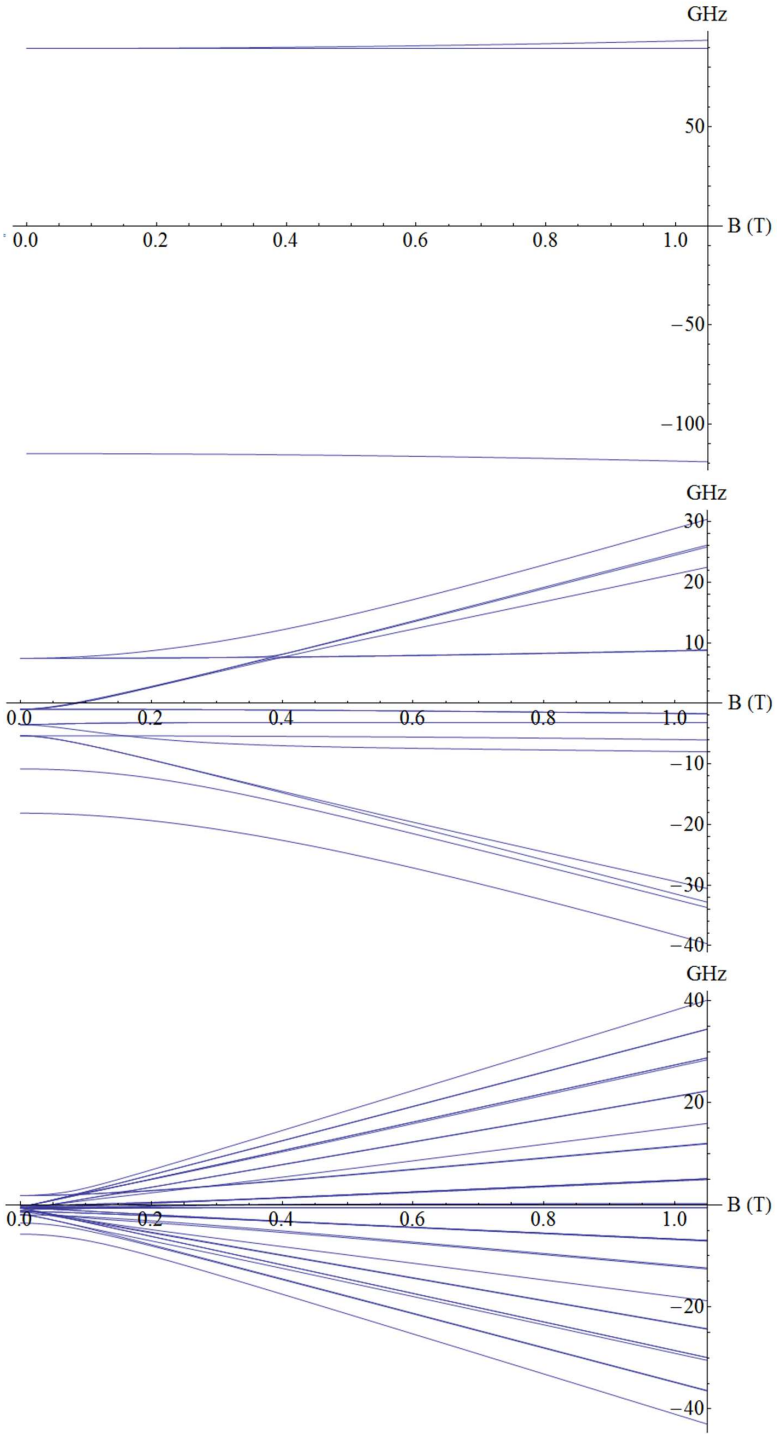

Figure 3.5: Splitting of sublevels of n=1,2,3 in magnetic field and for the reference Ps velocity of 100 K

$\Delta t_{coh} = \lambda^2/c\Delta\lambda_L$, where λ is the central wavelength of the proper transition and $\Delta\lambda_L$ is the FWHM spectrum of the laser pulses, chosen to match the positronium broadenings. This parameter turns out to be up to three orders of magnitude shorter than the average 5 ns duration of the laser pulses (sec. 2), hence we are operating with a completely incoherent excitation for both transitions.

The wide spectrum, needed due to cover the Doppler effect, is wide enough to allow us to use a rate equation model instead of optical Bloch equations model required by a coherent excitation. A good article on rate equations model is [58], that I summarize in the following passages for a simple two level scheme. Then I'll generalize it for many levels excitation.

This model is based upon classical fluctuating electromagnetic field like:

$$\vec{E_{field}}(\vec{x},t) = \frac{1}{2}\vec{\epsilon}\vec{E}(\vec{x},t)e^{i(\vec{k}\cdot\vec{x}-\omega t+\phi(t))} + c.c. \tag{3.15}$$

where the field propagates with wave vector $\vec{k}$, angular frequency $\omega = ck$ and phase $\phi(t)$. $\vec{\epsilon}$ is a unit vector representing the field polarization. The field complex amplitude is assumed slowly varying in space and time with respect of frequency and wave vector (the usual *Slowly Varying Envelope Approximation* in temporal shape).

For the atomic Ps I consider that the center of mass moves classically, so the effect of the dipole interaction of the atom with the laser field is the excitation of classically moving atom whose internal dynamics can be described by the density matrix $\rho(t)$, which parametrically depends on classical coordinates of Ps center of mass. The Optical Bloch Equations, that are the Liouville equations for the quantum density matrix ρ, can be write as

$$i\hbar\frac{\partial\rho}{\partial t} = \left[\hat{H}+\hat{V},\rho\right] + i\hbar\hat{R}\rho \tag{3.16}$$

Where $\hat{H}$ is the Ps Hamiltonian, $\hat{V}$ is the electric dipole operator for the interaction of the Ps with the laser field and $\hat{R}$ is the operator for the losses of the system for spontaneous optical decays or annihilations. I consider the model of Ps atom described before, where the external magnetic field and induced electric field mix together the unperturbed spin-orbit wave functions. This results in a loss of spectroscopy notation because all the sublevels of a state are a superposition of many unperturbed sublevels. Hence, we indicate the sublevels only with subscript e_i for the excited and g_i for the ground states. Using rotating wave approximation [58] the optical Bloch equations for the slowly varying matrix elements of the density matrix operator for ground g_n and excited e_m levels transition can be written as

$$\frac{\partial\rho_{g_i,g_i}}{\partial t} = \quad \frac{iE(\vec{x},t)}{2\hbar}\sum_{e_k}\left(d^*_{g_i,e_k}\rho_{e_k,g_i} - d_{e_k,g_i}\rho_{g_i,e_k}\right) - i\frac{\varepsilon_{g_i}}{\hbar}\rho_{g_i,g_i} \tag{3.17}$$

$$
\begin{aligned}
& + \textstyle\sum_{e_j} \Gamma_{g_i}^{e_j} \rho_{e_j,e_j} - \sigma_{g_i} \rho_{g_i,g_i} \\
\frac{\partial \rho_{e_i,g_j}}{\partial t} = & \ \tfrac{i d_{e_i,g_j} E(\vec{x},t)}{2\hbar} \left(\rho_{g_j,g_j} - \rho_{e_i,e_i} \right) - i(\omega - \omega_{e_i,g_j} + \tfrac{\partial \phi(t)}{\partial t}) \rho_{g_i,e_j} \\
& - \tfrac{\Gamma_{g_j}^{e_i} + \sigma_{g_j} + \sigma_{e_i}}{2} \rho_{e_i,g_j} \\
\frac{\partial \rho_{e_i,e_i}}{\partial t} = & \ \tfrac{iE(\vec{x},t)}{2\hbar} \textstyle\sum_{g_k} \left(d_{e_i,g_k} \rho_{g_k,e_i} - d_{g_k,e_i}^* \rho_{e_i,g_k} \right) - i \tfrac{\varepsilon_{e_i}}{\hbar} \rho_{e_i,e_i} \\
& - \textstyle\sum_{g_k} \Gamma_{g_k}^{e_i} \rho_{e_i,e_i} - \sigma_{e_i} \rho_{e_i,e_i}
\end{aligned}
$$

where $d_{e,g}$ are the dipole elements between the e and g states, Γ are the spontaneous emission rates, σ are the annihilation rates, ε are the eigenvalues of the Hamiltonian,$\phi(t)$ are the phase fluctuations of the laser pulse, ω is the angular frequency of the laser and $\omega_{e,g}$ is the angular frequency of the positronium transition. We have ignored the losses for photoionization, due to the fact that this value is very low when considering the energy required to saturate the transition [28]. Making a statistical average on the fluctuating phase $\phi(t)$ and solving the equations for the coherences ρ_{e_i,g_j} with initial condition $\rho_{e_i,g_j}(t_0) = 0$, lead to:

$$
\begin{aligned}
\frac{\partial \langle \rho_{g_i,g_i} \rangle}{\partial t} = & \ \tfrac{iE(\vec{x},t)}{2\hbar} \textstyle\sum_{e_k} \left(d_{g_i,e_k}^* \langle \rho_{e_k,g_i} \rangle - d_{e_k,g_i} \langle \rho_{g_i,e_k} \rangle \right) - i \tfrac{\varepsilon_{g_i}}{\hbar} \langle \rho_{g_i,g_i} \rangle \qquad (3.18) \\
& + \textstyle\sum_{e_j} \Gamma_{g_i}^{e_j} \langle \rho_{e_j,e_j} \rangle - \sigma_{g_i} \langle \rho_{g_i,g_i} \rangle \\
\langle \rho_{e_i,g_j} \rangle = & \ \tfrac{i d_{e_i,g_j} E(\vec{x},t)}{2\hbar} d_{e_i,g_j} \textstyle\int_{t_0}^{t} e^{i[(\omega - \omega_{e_i,g_j}) - (\Gamma_{g_j}^{e_i} + \sigma_{e_i} + \sigma_{g_j})/2](t-t')} \langle \rho_{g_j,g_j} e^{i\phi(t) - i\phi(t')} \rangle dt' \\
& - \tfrac{i d_{e_i,g_j} E(\vec{x},t)}{2\hbar} d_{e_i,g_j} \textstyle\int_{t_0}^{t} e^{i[(\omega - \omega_{e_i,g_j}) - (\Gamma_{g_j}^{e_i} + \sigma_{e_i} + \sigma_{g_j})/2](t-t')} \langle \rho_{e_i,e_i} e^{i\phi(t) - i\phi(t')} \rangle dt' \\
\frac{\partial \langle \rho_{e_i,e_i} \rangle}{\partial t} = & \ \tfrac{iE(\vec{x},t)}{2\hbar} \textstyle\sum_{g_k} \left(d_{e_i,g_k} \langle \rho_{g_k,e_i} \rangle - d_{g_k,e_i}^* \langle \rho_{e_i,g_k} \rangle \right) - i \tfrac{\varepsilon_{e_i}}{\hbar} \langle \rho_{e_i,e_i} \rangle \\
& - \textstyle\sum_{g_k} \Gamma_{g_k}^{e_i} \rho_{e_i,e_i} - \sigma_{e_i} \langle \rho_{e_i,e_i} \rangle
\end{aligned}
$$

The next step to solve the equations is to evaluate the $\langle \rho_{a_i,a_i} e^{i\phi(t) - i\phi(t')} \rangle$ (where a stays for ground or excited states). We used the decorrelation approximation, as in [59], that neglect the fluctuations of $\rho_{a,a}$ around its mean value $\langle \rho_{a,a} \rangle$, thus separating the atomic and laser field variables in previously equation.

$$
\langle \rho_{a_i,a_i} e^{i\phi(t) - i\phi(t')} \rangle \approx \langle \rho_{a_i,a_i} \rangle \langle e^{i\phi(t) - i\phi(t')} \rangle \qquad (3.19)
$$

The decorrelation is mathematically valid only for Wiener-Levy type phase fluctuations, but for general stochastic fields can be used as a first approximation. Either a phase jump fluctuation or a phase diffusion model lead to similar results [58]: $\langle e^{i\phi(t) - i\phi(t')} \rangle = \exp[-(\Delta\omega/2)(t - t')]$, where $\Delta\omega$ is the FWHM spectrum of the laser pulse. Another approximation that can be

done in order to simplify the equation is the so called *broad-line approximation* or BLA. This approximation requires that the laser spectrum $\Delta\omega$ is wider than the natural linewidth of the atomic transitions (mainly due to the spontaneous emission rate Γ_g^e) and the characteristic rate of the density matrix evolution. Using this approximation the population of the optical coherencies $\rho_{e,g}$ become a steady state population and the Bloch equations became simpler rate equations:

$$\begin{aligned}
\rho_{e_i,g_j} &= \frac{iE(t)d_{e_i,g_j}}{2\hbar}\frac{\rho_{g_j,g_j}-\rho_{e_i,e_i}}{\left(\Gamma_{g_j}^{e_i}+\sigma_{e_i}+\sigma_{g_j}+\Delta\omega\right)/2-i(\omega-\omega_{e_i,g_j})} \qquad (3.20)\\
\frac{\partial\rho_{g_i,g_i}}{\partial t} &= \frac{|E(t)|^2}{2\hbar^2}\sum_{e_j}|d_{g_i,e_j}|^2\left(\rho_{e_j,e_j}-\rho_{g_i,g_i}\right)\frac{\left(\Gamma_{g_i}^{e_j}+\sigma_{g_i}+\sigma_{e_j}+\Delta\omega\right)/2}{\left(\Gamma_{g_i}^{e_j}+\sigma_{g_i}+\sigma_{e_j}+\Delta\omega\right)^2/4+(\omega-\omega_{e_j,g_i})^2}\\
&\quad+\sum_{e_j}\Gamma_{g_i}^{e_j}\rho_{e_j,e_j}-\sigma_{g_i}\rho_{g_i,g_i}\\
\frac{\partial\rho_{e_j,e_j}}{\partial t} &= -\frac{|E(t)|^2}{2\hbar^2}\sum_{g_i}|d_{g_i,e_j}|^2\left(\rho_{e_j,e_j}-\rho_{g_i,g_i}\right)\frac{\left(\Gamma_{g_i}^{e_j}+\sigma_{g_i}+\sigma_{e_j}+\Delta\omega\right)/2}{\left(\Gamma_{g_i}^{e_j}+\sigma_{g_i}+\sigma_{e_j}+\Delta\omega\right)^2/4+(\omega-\omega_{e_j,g_i})^2}\\
&\quad-\left(\sum_{g_i}\Gamma_{g_i}^{e_j}+\sigma_{e_j}\right)\rho_{e_j,e_j}
\end{aligned}$$

We implemented this model with a Mathematica 8 code. We calculate the dipole elements using the eigenstates linear combination of the L-S states calculated via the numerical diagonalization of the interaction matrix in presence of strong magnetic and electric fields. The dipole matrix elements $\langle\psi_1|e\,\hat{r}|\psi_2\rangle$ are evaluated using the coefficient founded in numerical diagonalization c_n obtaining $\langle\psi_1|e\,\hat{r}|\psi_2\rangle=\sum_{a,b}\langle c_a\psi_a(n,l,s,j,m)|e\,\hat{r}|c_b\psi_b(n',l',s',j',m')\rangle=\sum c_a\,c_b\langle\psi_a(n,l,s,j,m)|e\,\hat{r}|\psi_b(n',l',s',j',m')\rangle$, where the last element in the sum is the dipole element between unperturbed L-S states, that we calculated as [60]. Knowing the dipole elements, it is possible to calculate the spontaneous and stimulated rate for the transition.
We calculate the spontaneous emission rates Γ_g^e of the rate equations mode as:

$$\Gamma_g^e=8\pi^2 d_{e,g}^2\frac{|\omega_{e,g}|^3}{3\hbar\epsilon_0 c^3} \qquad (3.21)$$

The annihilation rates are calculated only for $l=0$ states, the faster to decay. We used the values in absence of fields, 142 ns for ortho-positronium and 125 ps for para-positronium ground states and the same values multiplied by n^3 for upper $l=0$ states [61]. The states with $l>0$ have a lifetime of several order of magnitude longer, in the range of tenths of ms or even more, thus they are near stable in our temporal scale. We assigned a rate to the diagonalized states based on the eigenvector corresponding to unperturbed l states multiplied by the annihilation rate of that state.

The calculation of stimulated transition rates is separated into two parts: one, time dependant, contains the intensity of the laser field and its temporal shape, the other contains the constant coefficients obtained by the rate equations model described before. We used a Gaussian shape both for temporal and spectral intensity, defining ours intensity as $I(t) = I_0 e^{-2(t-t_0)^2/(\Delta t/1.177)^2}$, where t_0 is the center of the pulse duration and Δt is the FWHM duration of the pulse. The shape can easily be modified to represent a more realistic temporal shape without changing the complex rate equation solver. The constant coefficient that multiply the laser intensity is derived by the rate equations 3.21:

$$\frac{\pi d_{e,g}^2}{2\hbar^2} \frac{(\Delta\omega + 2\pi\sigma_i)/2}{((\Delta\omega + 2\pi\sigma_i)/2)^2 + (\omega_{e,g} - \omega)^2} \tag{3.22}$$

where $d_{e,g}$ is the dipole element calculated before, $\Delta\omega$ is the FWHM laser spectrum in angular frequency unit, σ_i is the annihilation rate for the ith state and it is multiplied by 2π to obtain it in angular frequency units, ω is the laser angular frequency and $\omega_{e,g}$ is the positronium transition angular frequency corrected for external fields.
Then we solved numerically the differential set of rate equations 3.21 for the $4n^2$ sublevels of each level involved. The parameters that we can choose in the code regarding Ps atoms are theirs velocity transverse to magnetic field, the external magnetic field and electric fields parallel and perpendicular to magnetic field; the laser pulse parameters are its FWHM spectrum, FWHM duration and dimension, its polarization and its peak intensity while the shape is fixed to be gaussian in time, spectrum and space.

3.3.1 Dynamics of the excitation to n=2

The first thing we did was to compare the results with literature. In [46] Dermer et al. have developed a rate equations model for n =1 to 2 transition in presence of a magnetic field and an electric field parallel to the magnetic field. To reproduce their results, we have written the equations for that transition using perturbation theory for electric dipole elements calculation, as indicated in equation 3.4, in order to better understand the dependence of the system by its features. Figure 3.6 shows the excitation dynamics of all sublevels of n=2 with the same configuration of fig.4 of [46]. The results are comparable both in excited population fractions and in rate of spontaneous decays. In the same figure is shown the same dynamics calculated with full matrix diagonalization: the difference between the two graph are very small so the field is low enough to perform a perturbative approximation. The

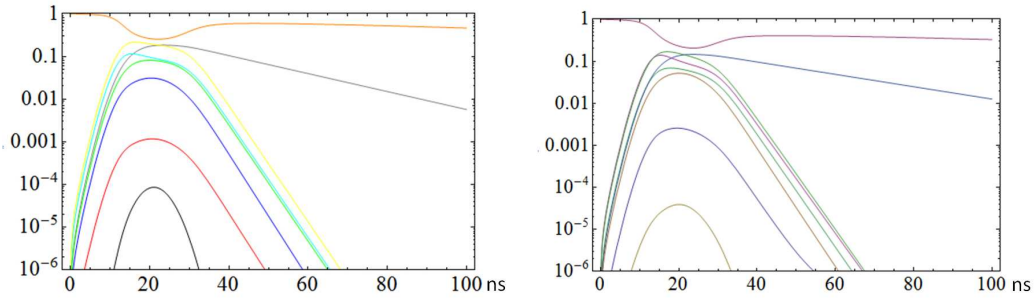

Figure 3.6: Population of sublevels in the same condition as [46], the graph on the left is done using perturbation model, the other is done with full matrix diagonalization

differences are mainly in a small variation of the transition rates that mix, at low degree, the faster and slower decaying states. This difference become evident in the case of nonperturbative field, i.e. with magnetic field higher than about 300 Gauss, or for lower field when considering transitions to higher levels, for example to n=3.

3.3.2 Dynamics of the excitation to level n=3

The code can be easily improved to describe the dynamics of n =1 to 3 transition, adding the $n = 3$ sublevels, changing the stimulated rates accounting for new dipole elements $d_{1,3}$, calculating spontaneous transition rates from $n = 3$ to 2 and changing the laser angular frequency to match the new positronium transition angular frequency. The rate equations now account for a three levels atom, where $n = 2$ sublevels are populated only by spontaneous transitions from $n = 3$ and they decay for annihilation or spontaneous emission to $n = 1$.
For $n = 3$ the perturbation theory shows some limits: magnetic fields of few hundred Gauss are big enough to go beyond perturbation theory limits and the $n = 3$ state has two degenerate substates, namely $^3P_2$ and $^3D_2$, that require matrix diagonalization even at zero order perturbation stage. Hence we have done the same calculation with the full diagonalization of the interaction matrix and checked the results within the limits of perturbative theory for debugging. Using this last code we can explore the whole range of parameters, such as external fields, laser pulses characteristics and Ps velocity in order to improve the heuristic calculation done in [28]. The goal of the transition simulation performed with this program is to find the best

parameters for maximizing the excitation to $n = 3$ for Aegis Ps. An example of population versus time plot for Aegis experiment is reported in fig. 3.7.

3.3.3 Studies on excitation efficiency

A first study was conducted to find the dependency of the excitation results versus the Ps velocity transverse to magnetic field using different laser pulses energies. We varied the Ps velocity from 0 to 10^6 m/s in constant magnetic field of 1T, effectively varying the motional Stark effect seen by Ps atom. In ours calculation we considered the positronium moving with fixed velocity rather than averaging on a thermal Doppler distribution to adapt the results with real velocity distribution of the positronium considered, that may be not fully thermalized. The maximum of the excitation percentage is reported in figure 3.8, calculated as the maximum of the sum of the population on the desired excited level ($n = 3$) divided by the sum of the population on all levels, for a linear laser polarization along magnetic field.

For very slow velocity the motional Stark effect is negligible within the sublevel dynamics, thus the dynamic is the same of zero fields, showing a saturation at 50% for sublevels with high unperturbed dipole elements, while some sublevel with low transition rates are excited for very high laser intensity due to Zeeman mixing. Increasing the positronium velocity, the motional Stark mixes the levels, having more sublevels with high enough stimulated transition rate to be excited, increasing the population fraction on n=3. A maximum of excitation efficiency is visible for positronium velocities around $10^4 m/s$. For Ps velocity higher than $3 \times 10^5 m/s$ the motional Stark effect become the dominant broadening and become bigger than the laser spectrum, so some losses arise from the most influenced sublevels that go beyond laser spectral width.
We also studied the energy required for the excitation as a function of the laser FWHM spectrum, shown in figure 3.9. Centering the laser wavelength on the most easily excitable transition, as done in all the simulation, we can see that with smaller spectrum width less energy is required to saturate the transition, while the maximum of the excitation fraction is the same. The rate equation model used account only for a spectrum larger than the inverse of the coherence length, in this condition the only limitation on reducing the spectrum width is to match the positronium resonance, thus to match the Doppler effect. For Aegis the Doppler broadening seen by positronium atoms having a direction towards the antiproton cloud is about 32 GHz, so a laser

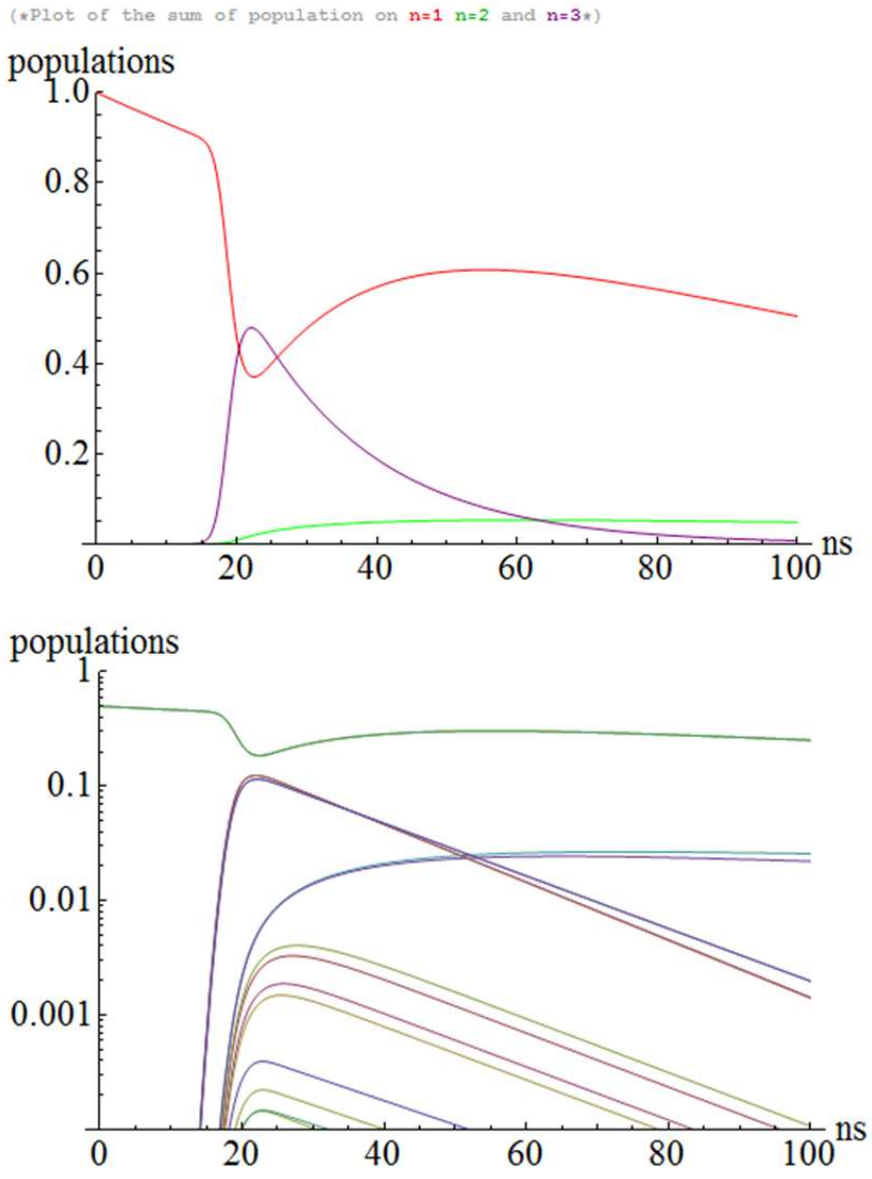

Figure 3.7: The calculation is done using 5 μJ of laser energy, 117 GHz of spectrum, 4 ns FWHM Gaussian time duration centered in 20 ns with 1T magnetic field and 5 10^4 m/s Ps velocity. The first graph is the sum of all sublevels of each n, the second is the population of each single sublevel

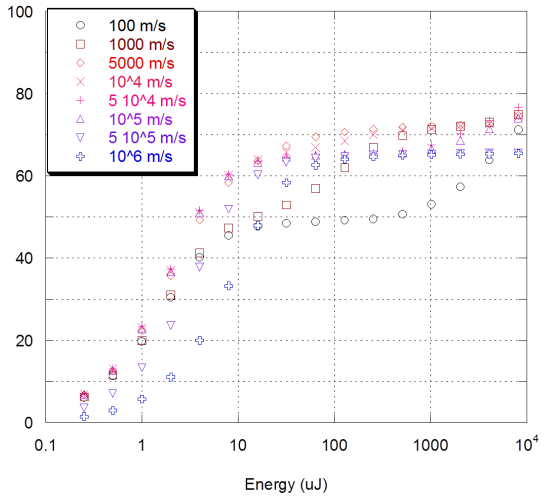

Figure 3.8: Maximum of excitation for different Ps velocities in 1T magnetic field and 117 GHz of spectrum for the transition to n=3 levels.

spectrum below this value will excite efficiently only a part of the available Ps atoms. The laser spectrum width, thus, must be tailored on the expected Doppler broadening of the positronium cloud. An intriguing observation that can emerge from that calculations can be derived from a comparison with a $n = 1$ to 2 excitation. The results of excitation in function of Ps transverse velocity in the same condition of fig. 3.8 are reported in fig 3.10 for transition to level $n = 2$. The dependence of the excitation efficiency from Ps velocity is very small compared to 1 to 3 case because the $n = 2$ state is less sensible to motional Stark effect. In [46] Dermer et al. calculated a λ^{-3} dependence of the saturation fluency from simple consideration on spontaneous and stimulated emission of a lossless two level system. As shown in fig. 3.11, exciting to level 2 instead of 3 require about $(243/205)^3 = 1.67$ less energy than level 3 for a large range of laser pulse energies. This apparently not favorable choice of excitation to n=3 was rewarded by the transition to Rydberg levels, that requires $(1654/731)^3 = 11.6$ times less energy than excitation from $n = 2$, hence having on the whole lesser laser energy in the reaction chamber.

3.3.4 Discussion on 3-n transition: studies on high-n levels

The effect due to the motional Stark electric field becomes the dominant characteristic of the transition. Because of it, the degenerate high-n levels become fans or manifolds of their n^2 sublevels with a mixing of their m and

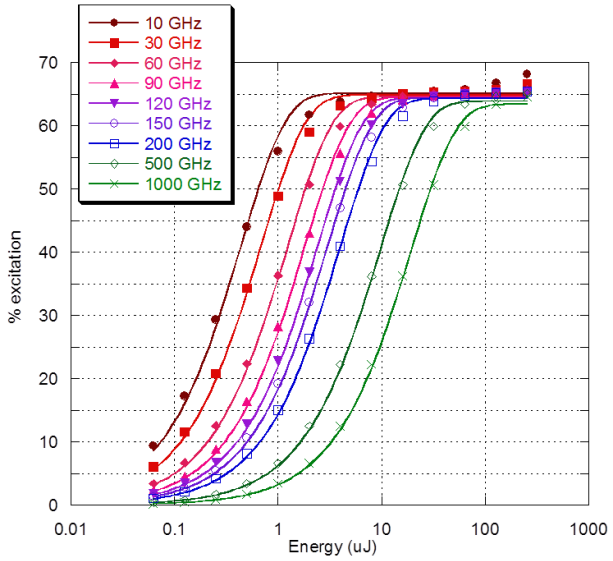

Figure 3.9: Maximum of excitation for different laser spectrum, in 1T magnetic field and 5 10^4 m/s Ps velocity for transition to n=3 levels. The interpolation function is a fit with an exponential saturation proportional to $(1 - e^{-E/E_{sat}})$, where E is the laser energy per pulse and E_{sat} a saturation level

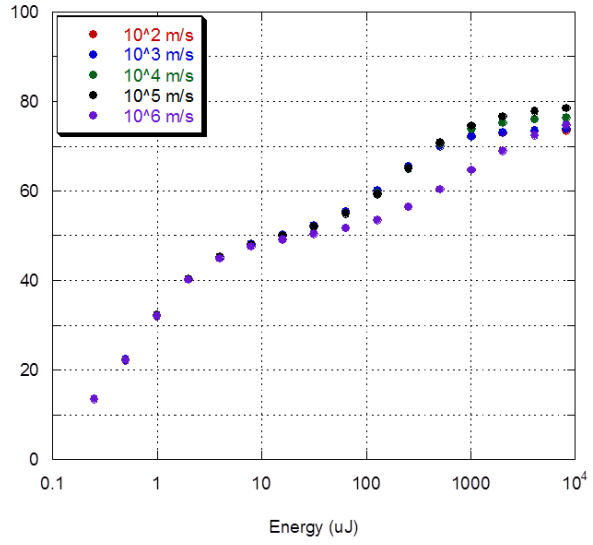

Figure 3.10: Maximum of excitation for different Ps velocities in 1T magnetic field and 117 GHz of spectrum for excitation to n=2 levels.

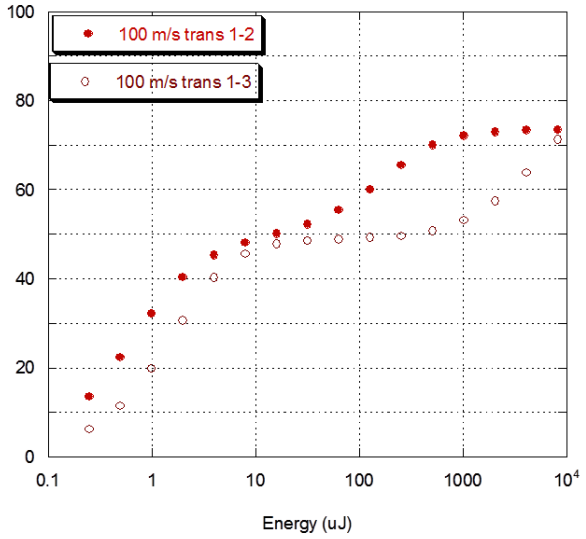

Figure 3.11: Comparison between excitation to n=2 and 3 with same laser spectrum (117 GHz), magnetic field (1T) and Ps velocity (100 m/s, so the motional Stark effect is very low even for n=3)

l substates, while the mixing between n levels in positronium atoms does not occur to a good extent [57]. Owing to the m and l sublevel mixing, these unperturbed quantum numbers are no longer good quantum numbers labeling the states, at variance with the principal quantum number n which retains its role [49]. While a Stark effect parallel to the quantization axis can be solved analytically via a variable separation in elliptical coordinate [51], in our case the motional Stark effect is perpendicular to quantization axis, chosen parallel to the magnetic field direction, thus we can't do a variable separation as above and a numerical solution is required.
As the principal quantum number n increase, the separation between adjacent n levels decreases, approximately as n^{-3}. For high enough n the motional Stark broadening dominates over the separation of different n levels, thus having an interleaving effect. For a given high n level, there is an interleaving of many unperturbed level structures, we can first assume an uniform distribution of the $4n^2$ sublevels within the motional Stark energy width ΔE_{MS} as done in [28]. The number of unperturbed n levels interleaved with the reference level energy width is:

$$N_n \approx \frac{\Delta E_{MS}}{\Delta E_n} \approx 4n^5 \frac{6ea_0}{13.6eV} |\vec{E}_\perp| \tag{3.23}$$

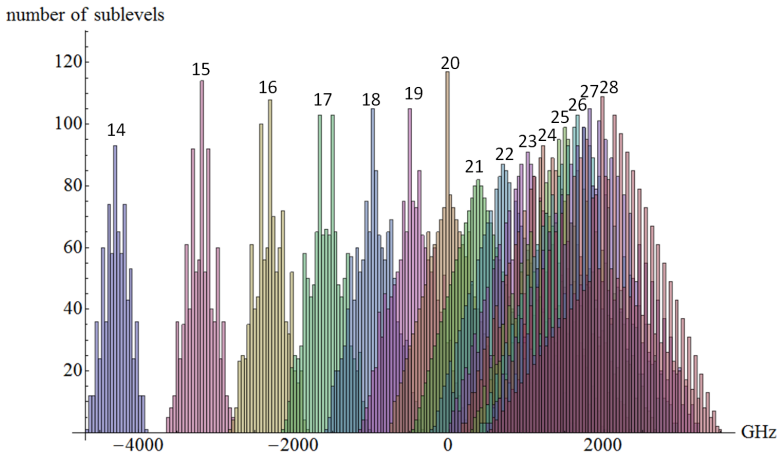

Figure 3.12: This is an histogram of the number of sublevel per 40 GHz bin for positronium levels from 14 to 28. The histogram is center on the frequency of the 3 to 20 transition

This leads to a sublevel density for angular frequency of:

$$\rho(\omega) = \frac{n^2 N_n \hbar}{\Delta E_{MS}} = 4n^5 \frac{\hbar}{13.6eV} \tag{3.24}$$

independent, in its validity range, from the strength of the motional Stark field and so from the Ps velocity.
We calculated the eigenvalues of the first 28 levels of positronium using the full diagonalized program described in sect. 3.3 considering fine structure, external magnetic and electric fields; higher n will require very long calculation to diagonalize a square matrix of $4n^2$ row, for example $n = 28$ matrix has 9.8 million elements. Choosing one condition for positronium, i.e. 1T magnetic field and 5 10^4 m/s of transverse velocity, we recorded the number of eigenvalues and therefore the number of sublevels collected in an energy bin of an histogram (fig 3.12). As predicted in [28] the eigenvalues corresponding to different n fan are separated up to $n = 15$. This lower value compared to 17 from fig. (3.3) is due to the presence of many broadening effects (mainly the 56GHz Zeeman splitting) rather than motional Stark only. Integrating the function (3.24) in order to compare the number of sublevels calculated previously with the analytical function, we found quite a good agreement up to $n = 21$. As the n level increase, the width of sublevels distribution increase, approximately as n^2, while the frequency of the distribution center (corresponding to the unperturbed energy level) increase slowly, as n^{-3}, thus for very high n levels the motional Stark broadening cover the unperturbed energy of lower n level. Such very high n levels, however, have a small dipole

element with the n=3 level (it scales as n^{-2}), so we can ignore those levels from the study of an excitation aimed to levels 20 - 30. Very high n levels, also, have an high ionization probability (eq. 3.12), thus the small probability of exciting a very high n level can be seen as a loss for ionization rather than an increase in excited population.
The plots in fig. 3.13 show this behavior as a function of the frequency or the position of the n^{th} level, calculated with the change of variable:

$$\begin{aligned} h\nu &= \frac{13.6eV}{2n_{ref}^2} - \frac{13.6eV}{2n^2} \\ n &= n_{ref}\sqrt{\frac{13.6eV}{13.6eV - 2n_{ref}^2 h\nu}} \end{aligned} \tag{3.25}$$

where n_{ref} is a reference n level ($n_{ref} = 20$ for the figures of this section). This second plot stresses the fact that rising in frequency the n levels are more and more thigh together and the broadening, due to Stark effect for example, interleaves many n levels. The good agreement between the sublevel density calculated with fine structure, Zeeman and motional Stark and that calculated in [28] allows to conclude that the previously results are good as long as the laser spectrum is wide enough to smooth the small spikes of graph 3.13 and to consider the more simply analytical function rather than the exact sublevel function density which needs a very long calculation.
The rate equations model implemented for ground to $n = 3$ transition can't be done used for the second transition, due to the high sublevel number (some hundreds) that can interact altogether. A rough calculation for transition to level 20 involve 4 ground sublevels, 36 $n = 3$ sublevels and more than 300 Rydberg sublevels; the interactions are about $4 \times 36 = 144$ for the first transition and $36 \times 300 \approx 11000$ for the transition to the Rydberg states. In the spirit of optical excitation of a continuous level band, we choose a laser pulse spectrum lesser than the width of motional Stark effect . Generalizing the theory of incoherent excitation, we can write the excitation probability for unit time $W_{3\to n}(t)$ as:

$$W_{3\to n}(t) = \int_{\Delta E_L} \frac{I(\nu,t)}{h\nu}\sigma_{3n}(\nu)d\nu \tag{3.26}$$

$$\sigma_{3n}(\nu) = h\nu\rho(\nu)B_{MS}(\nu)/c \tag{3.27}$$

where ΔE_L is the laser pulse spectrum width, $I(\nu, t)$ is the laser intensity spectrum, $\sigma_{3n}(\nu)$ is the photon absorption cross-section, $\rho(\nu)$ is the positronium sublevel density and $B_{MS}(\nu)$ is the absorption coefficient for a single sublevel of the totally mixed Rydberg level structure. In order to evaluate this last term, we make the assumption that, for the high Zeeman and motional Stark effect involved, we can write the wave function of a Rydberg sublevel

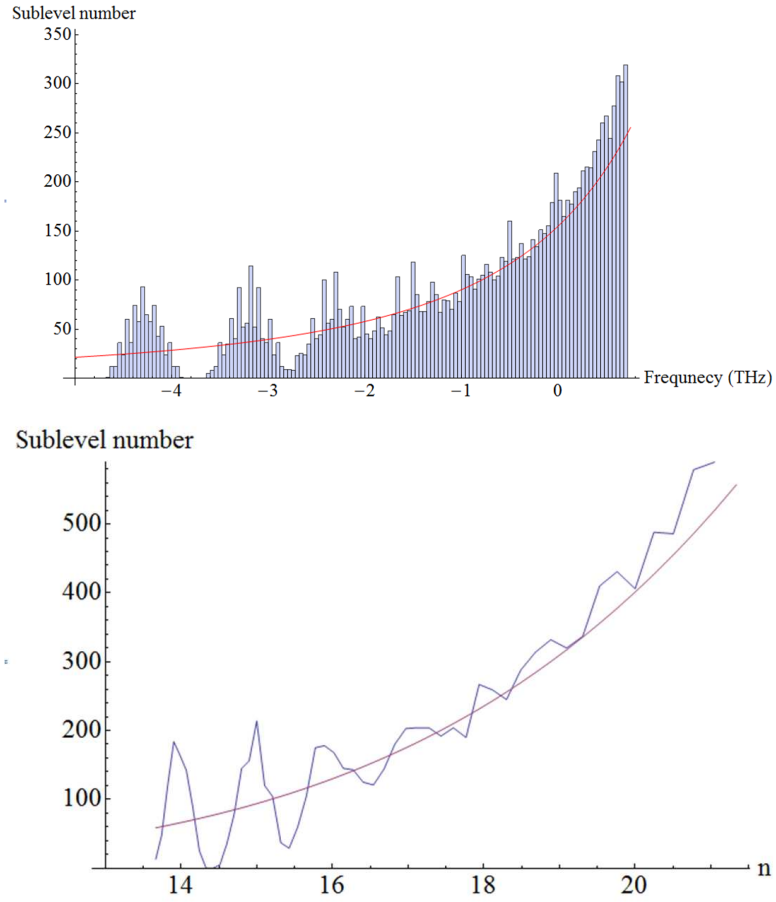

Figure 3.13: Those histograms are the sum of sublevels from the first 28 n levels as a function of frequency (binned at 40 GHz) and of the correspondence of unperturbed n levels position. The red line correspond to the foreseen sublevel number from eq. 3.24 integrated over the bin length.

as a superposition of the unperturbed function $\psi_n = \sum_{l,s,j,m} c_{l,s,j,m}\psi_{n,l,s,j,m}$ with a full mixing configuration, where the coefficients $c_{l,s,j,m}$ have all the same value $1/2n$ (normalizing the sum of $|c_{l,s,j,m}|^2$ to 1). Considering the dipole selection rule between $n = 3$ sublevels and Rydberg levels, the B_{MS} coefficient become:

$$B_{MS}(\nu) \approx \frac{1}{4n^2}|\langle\psi_{n,l,s,j,m}|e\,\vec{r}\cdot\vec{\varepsilon}|\psi_{3,l',s',j',m'}\rangle|^2 = \frac{1}{4n^2}B_{3n}(\nu) \tag{3.28}$$

Since the dipole element of Rydberg wave functions scale as $n^{-3/2}$, the Einstein absorption coefficient $B_{3n} = |d_{3,n}|^2\pi/\epsilon_0\hbar^2$ scale as n^{-3} and the B_{MS} coefficient scale as n^{-5}. Thus the excitation probability $W_{3\to n}(t)$ is at first order independent on n and positronium velocity. Following the procedure outlined in [28] we can obtain a saturation fluency, defined as in the reference, for the Rydberg band saturation:

$$F_{sat}(3 \to n) = \frac{c \cdot 13.6eV}{4hn^3 B_{3n}(\nu)} \tag{3.29}$$

when the full mixing approximation hold it turns out to be approximately a constant around a value of 0.25 mJ/cm^2. We remark that this fluency value is heuristically calculated in a condition of complete mixing of the wavefuntions. The magnetic field is high, i.e. a Paschen-Back effect is affecting positronium atoms with a freezing effect on Δs laser induced mixing and an enhanced annihilation rate for the $m_s = 0$ spin wavefunction projection leaving only $m_s = \pm 1$ spin wavefuntion to be considered in the transition, thus we think that at least only half the state can be involved in optical transition, halving the sublevel density and, conseguently, doubling the saturation fluency.

In order to have a better estimate of the degree of wavefunction mixing, we calculated the coefficients of the eigenfuntions for the magnetic and induced electric fields of the Aegis environment (1 Tesla with a transverse velocity of about 10^4 m/s) for a reference level ($n = 20$). The very high number of subleves, 1600, thus the coefficient, 1600^2=2.56 millions, are computed via matrix diagonalization. For a complete mix of the wavefunctions we expect that all the coefficients have an absolute value of $1/2n = 0.025$. If the mix is not complete, we expect that some coefficients should be higher, while some others lower than this value. Looking at the calculated coefficients for $n = 20$, about a quarter (636819) of them are higher than 0.01 and a few (33) are higher than 0.3.

A further calculation was done: we selected the higher absolute value of coefficients for each sublevel decomposition and evaluate the number of sublevels for different values of maximum coefficient (fig. 3.14). A complete mixing

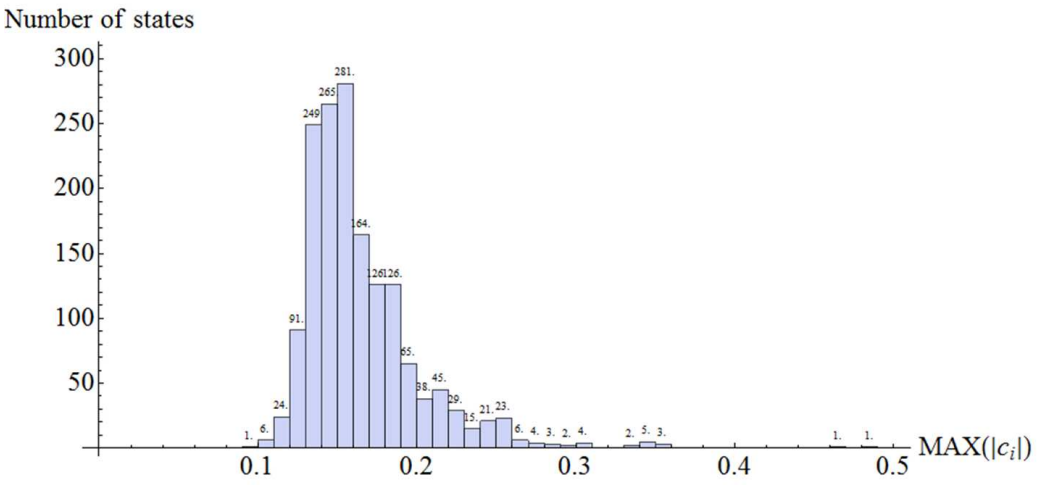

Figure 3.14: This histogram reports the maximum absolute value of $c_{j,l,m}$ for each $\psi_{20,i}$ wave functions. A full mix of states will lead to a coefficient of 0.025 while unperturbed wave functions have a maximum of this value equal to 1 (i.e. only one coefficient different from 0)

will produce an histogram centered on 0.025 value (the minimum allowed for the coefficient maximum), while a configuration of zero fields (unperturbed levels) has only one populated bit at value of 1. The calculated values are between 0.48 and 0.10, with a mean value of 0.16. An indication on the degree of wavefunction mixing can be extrapolated. Being the wavefuntion coefficients normalized ($\sum |c_i|^2 = 1$), if we consider that all the coefficient of the diagonalization are equal (to the founded maximum $|c_{max}|$), then the decomposition of the wavefunction will be composed of at least $1/|c_{max}|^2$ elements and more probably by a larger number. From ours calculation of sublevels of n=20, the minimum projection coefficients high enough are from 4 to 100 for each sublevel, with an average of 44. This value put a limit on how few elements the wavefunctions are composed by.

3.4 Conclusions

In this chapter we have analyzed the positronium excitation in different conditions. In this section is summarized the results useful for Aegis apparatus, for other experiments that can be done with Aegis positron source and a brief consideration on other applications.
For Aegis apparatus, where the positronium is generated in 1T magnetic field with a velocity of about 5 10^4 m/s, in order to excite the positronium

to $n = 3$ with a wavelenght of 205.03 nm the calculated energy for a gaussian pulse of 4 ns FWHM duration, 3 mm FWHM dimension and 117 Ghz FWHM spectrum is of 10 μJ per pulse, as shown in fig. 3.8. The resulting efficiency, considering only 1 to 3 transition, is about 60%, as coming out from the numerical simulation preformed in sec. 3.3.3. The spectrum requirement is of at least 32 GHz of FWHM in order to cover the transverse Doppler shift of positronium crossing the antiproton cloud using a near orthogonal laser irradiation. More spectrum allows to excite positronium with higher velocity and with velocities towards the laser pulse propagation direction.
The excitation to $n = 3$ can be detected inside Aegis as a small increase in positronium lifetime due to the excitation time and subsequently spontaneous emission, this can lead to an increase of lifetime of about 15 ns. Another way consists in the detection of 205 or 243 nm delayed emission due to spontaneous decay. When the laser will excite the positronium, the population on higher levels have a lesser annihilation rate, thus on a small temporal window around the laser excitation time the annihilation detector should see less counts if the detector is fast enough. The method used in [62], thus, won't be useful for the Aegis apparatus.
For the subsequent transition, for which we consider a 200 GHz FWHM laser spectrum, the excitation energy calculated with temporal and geometrical characteristics as in the first transition is of about 0.1 mJ. More energy can excite a bit more sublevels, but with an increase in final n spread and possible heating issues inside the cryogenic environment; a bit less energy can be enough to excite some of the sublevels (those with low wave function mixing) but with an overall smaller efficiency on Rydberg exited population. The best wavelength to use is about 1678 nm (corresponding to $n = 20$ unperturbed energy level), but can be finely tuned in the range of 1666-1693 nm($n = 17-24$) with a spectrum largely independent on excitation efficiency if wider than 60 GHz, in order to overcome the spikes present in fig 3.13.
The excitation of Rydberg states can be detected inside Aegis as a increase in positronium lifetime due to the hundred microseconds optical spontaneous emission lifetime of Rydberg levels. This time is long enough to allow the positronium to reach the antiproton cloud and hit the subsequent electrodes, giving a delayed spike in gamma detectors. This method of observation allows to measure the amount of excited positronium, but prevent to measure the exact distribution of excited sublevels.
To test the laser system as well as the approximation done in the theoretical treatment, a dedicated experiment in a more controllable environment can be envisaged. Using a smaller chamber dedicated to positronium experiment and the positron accumulator of Aegis, more accurate measure of positronium excitation can be done. With lower magnetic field, the excitation to

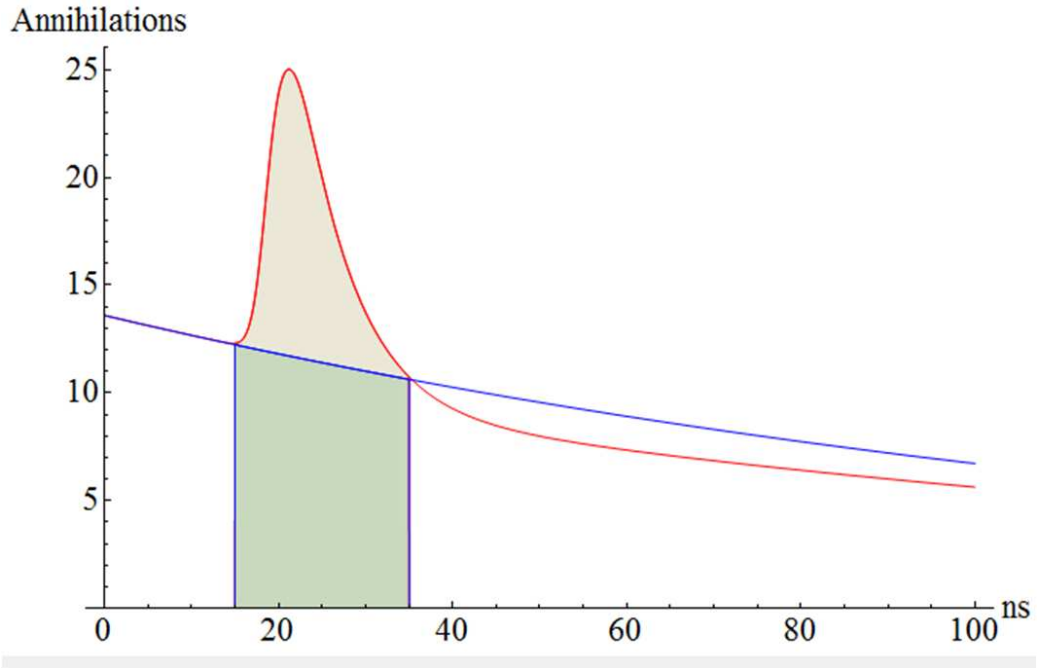

Figure 3.15: This graph represents the rate of gamma emission for annihilation per thousand positronium hit by laser pulse. The blue line is the annihilation with laser off. Red line are the annihilations with laser on (10 μJ in 200 Gauss magnetic field).

$n = 3$ can be seen as an excess annihilation due to Zeeman mixing, as done in [62]. Using a Cerenkov radiator crystal, as PbF_2, we can measure an excess annihilation that I can predict knowing the excited population with time (fig 3.7). A typical result of the numerical simulation is reported in figure 3.15.
More studies on low levels that can be done on positronium are about the fine structure (fig 3.1) of the low n levels. The laser system we have realized is not well suited for such measurements, because they require high precision in wavelength determination and our system was realized having in mind to maximize the excited population, that have a broad spectral distribution due to Doppler effect, rather than to selectively excite only one of the positronium sublevels at time. However, using microwaves in the range of few GHz (see fig. 3.1) after the broad excitation it is possible to selectively transfer population on the sublevels not involved in the transition with high enough precision on wavelength, being the Doppler effect on longer wavelengths reduced and choosing a microwave source with small spectral width.
Only one experiment on positronium Rydberg levels is reported in litera-

ture [47], where the levels are seen up to $n = 15$ as a small decrease in the excess annihilations due to $n = 2$ excitation. Rydberg levels can also be easily detected turning on an electric field, using electrodes or girds near the positronium excitation region, after the laser excitation to selectively ionize positronium, and collecting the charged particles with channeltron or MCP. Using this additional electric field it is possible to discriminate what levels of positronium are excited, how they are distributed with principal quantum number and the whole excitation efficiency. This technique can discriminate the Rydberg levels better than of the reduced annihilations counts used in [47]. This information will be valuable to study the maximization of the positronium excited to Rydberg levels, how many excited positronium atoms may reach antiprotons and what could be the principal quantum number distribution of the antihydrogen created with charge exchange reaction.
In AEGIS experiment only the Rydberg positronium atoms that are in the small solid angle that starts from the positron target and reaches the antiproton cloud can exchange charge with antiprotons resulting in antihydrogen formation. Laser cooling of the positronium in AEGIS can greatly enhance the production of antihydrogen via an increasing of the atoms that have the right direction to cross the antiproton cloud. But, apart for AEGIS application, there is a wide interest in the scientific community about laser cooling of positronium. For instance, with cooled positronium the measurements of fundamental constants reviewed in [44] will increase in accuracy because the reduction of Doppler effect will narrow the resonance bands. High density cold positronium will open the possibility to produce a positronium Bose-Einstein Condensate (BEC). A few amazing applications of a positronium BEC are gamma ray laser [63] and studies on antimatter gravity [64] in addition to high sensitivity spectroscopy on positronium. Laser cooling is a technique developed at the end of the 80s based on the interaction of light with atoms that can cool trapped gases to extremely low temperature. C. Cohen-Tannoudji (Nobel laureate in 1997 with S. Chu and W. Phillips [65]) pioneered the method. Photons are absorbed by the atoms, that gains the photon momentum directed in the direction of laser pulse propagation, and re-emit it later by isotropical spontaneous emission. In order to effectively cool the atom in every direction a configuration of orthogonal beams are required. The main limit of this cooling technique for positronium is known as *recoil limit*: the atoms velocity can't be reduced less than the velocity gained by a motionless positronium after a single photon emission [66]. Moreover, a great difference in positronium laser cooling compared to the usual atomic cooling is the time available for the cooling: ortho-positronium in ground state, in absence of external fields, decay in gamma photons with an half life of 142 ns, so the laser cooling process have to be well faster than in

stable atoms. Although simulations have indicated that positronium laser cooling is feasible, it is not yet demonstrated experimentally [67]. The only experimental attempt we are aware of was performed in 2002 in Japan [66]. Unfortunately, the project was terminated without success, mainly due to low intensities of positron/laser beams and difficulty in laser tuning. An important issue in laser cooling of positronium is the fact that it has been shown that Zeeman mixing of singlet and triplet 2P states of positronium atoms, followed by decay back to the ground state, can turn a long-lived triplet atom into a short-lived singlet state, which would seem to preclude laser cooling of Ps in low magnetic field. In presence of magnetic field strong enough to ensure the Paschen-Back regime this effect will be reduced [68]. Using the programs developed in my thesis it is possible to calculate, in a future development, the transition from ground to n =2 or 3 and account for the transition probability in presence of strong fields, thus allowing to calculate how many energy is required and how many transition can be done, in regime of incoherent excitation, for positronium cooling.

Appendix A

Appendix: Alignments

In this section we summarize the step needed to align some of the critical components of the system we have developed.

A.1 Laser cavity alignment

The procedure we used to align the laser cavity is the following, referring to fig.2.7.

1. Find the optical axis on which you want to build the laser using a He-Ne laser beam, while the optical cavity is empty in except of mirrors M1 and M2. We use two irises, one right outside M1 and one inside cavity, before M2.

2. Insert the Brewster plate assembly, with the mounting edges parallel to the optical axis.

3. Insert the rod assembly, having the attention that the He-Ne beam will be centered on both faces of the Nd:YAG rod. We used thin, semitransparent optical paper to better find the position of the He-Ne spot on rod surfaces.

4. Adjust Gaussian mirror M2, having the He-Ne beam spot inside the Gaussian reflecting coating of the mirror M2. In order to help finding the best position we used a small mirror under M2 to see if it is well centered on He-Ne beam.

5. Finely tune M2 in order to have He-Ne reflected in the centre of Nd:YAG rod and pass throughout the iris on M1. Usually we see two reflections from M2, due to the fact that the mirror is tuned to 1064 nm and the

633 nm He-Ne is reflected from both the mirror faces. We found that the top reflection must be centered in the Nd:YAG rod in order to align the laser.

6. Tune M1 in order to reflect He-Ne back to the Nd:YAG rod. When it is well aligned, the He-Ne reflection from Nd:YAG rod surface become brighter and some interference fringes appear.

7. Turn on the laser lamp and finely tune M1 in order to minimize the lasing threshold. For the laser we found that this minimum is around 700 on a scale of 1000 of the flash lamp intensity.

8. Insert the quarter wave plate assembly and align it in order to prevent lasing when the flash lamp is at full power.

9. Insert the pockel cell assembly and tune it in order to minimize the threshold.

A.2 OPG alignment

We used two translational stages, one in the vertical direction and one in the horizontal plane perpendicular to the pulses propagation, and two rotational stages, one on the base of the mounting, rotating in the horizontal plane, and one on the crystal mount, rotating in the vertical plane. The alignment procedure for the OPG crystals is the following:

1. Center the laser pulse on the CCD camera, using adequate filtering to not saturate the image

2. Insert the crystal assemble in the desired position and check that the pulse enter and exit from the crystal using viewing card. The crystal must be heated before it is exposed to pulsed beam to increase its damage threshold. Then check with CCD camera that the beam is at the center of the crystal, finding its edge translating the crystal with the micrometers.

3. In order to correct the angular direction of the crystal compared to the pulse propagation direction, find the reflection, usual of small intensity, from the input surfaces, usually two spots vertically aligned. Superimpose it with the coming beam on the horizontal direction. To correct the vertical angular orientation superimpose the higher spot

with the coming beam. This is due to the fact that the crystal has a small wedge, of about 0.1-0.2° and two different spots, one from the first surface and one from the second one will form.

4. Check on the camera to be in the middle of the crystal after angular orientation, else repeat the alignment procedure. Usually only for very large angular misalignment is required a strong translation correction, most of the time the translation correction is very small.

A.3 OPA alignment

For OPA crystals we used simpler alignment supports, that have an angular regulation on the plane parallel and perpendicular to the optical axis. The translation adjustments are done with manual correction of the mounts. The alignment procedure for the OPA crystals is the following:

1. Check the dimension and the divergence of the pump and the signal where you are planning to put the OPA crystals using low pump power and knife method for signal dimension.

2. Looking at the CCD camera, finely superimpose the pump and signal images in the crystal place as well as far from it in order to make the two pulses collinear.

3. Insert the first crystal assemble and look for the reflected spot of the pump. Orientate the crystal in order to superimpose the reflection with the incoming pump.

4. Look at the CCD camera, finely tuning the position of the crystal in order to center it on the pulses. Check for long enough distance that the pump and the signal are collinear.

5. Take out the CCD camera and rise the pump power. Using a dichroic mirror separate the pump form the signal and measure this one with the energy meter or with a photodiode. Check for the maximum value of signal energy changing the angle of crystal to phase match it

6. After tuned pump to low power, insert the second crystal immediately after the first, checking with CCD camera for the correct alignment of the crystal on pump and signal pulses.

7. Take out the CCD camera and rise the pump power. Align the second crystal in order to maximize the energy of the signal.

Bibliography

[1] G. Baur et al. Phys. Lett. B, 368 (1996) 251

[2] G. Blanford et al. Phys. Rev. Lett., 80 (1998) 3037

[3] http://athena.web.cern.ch/athena/

[4] http://hussle.harvard.edu/∼atrap/

[5] http://aegis.web.cern.ch/aegis/

[6] http://alpha-new.web.cern.ch/

[7] H. V. Knudsen et al; Nucl. Instrum. Methods Phys. Res. Sect. B, 266 (2008) 530

[8] http://asacusa.web.cern.ch/ASACUSA/

[9] R. J. Hughes, Nucl. Phys. A, 558 (1993) 605

[10] S. Schlamminger et al., Phys. Rev. Lett., 100 (2008) 041101

[11] J. G. Williams et al. Phys. Rev. Lett., 93 (2004) 261101

[12] M. Nieto and T. Goldman, Phys. Rep. 205, 5 (1992) 221

[13] J. Sherk, Phys. Lett. B, 88 (1979) 265

[14] M. Amoretti et al., ATHENA Collaboration, Nature, 419 (2002) 456

[15] G. Gabrielse et al., ATRAP Collaboration, Phys. Rev. Lett., 89 (2002) 213401

[16] A. Kellerbauer et al., Nucl. Instrum. Methods Phys. Res. Sect. B, 266 (2008) 351

[17] G. Testera et al., AEgIS collaboration, Proc. of Cold Antimatter Plasmas and Application to Fundamental Physics Conference (Okinawa) vol. 1037 (AIP Conference Proceedings, 2008) p 5.

[18] O. Halpern, Phys. Rev., 94 (1954) 904

[19] A. Bisi, A. Fiorentini, E. Gatti and L. Zappa, Phys. Rev., 128 (1962) 2195

[20] R. S. Brusa and A. Dupasquier, in "Physics with many positrons", R. S. Brusa, A. Dupasquier and A. P. Mills, Jr. eds. (IOS, Amsterdam 2010).

[21] R. Ferragut et al., Can. J. Phys., 89 (2011) 17

[22] R. Ferragut et al., J. Phys: Conf. Ser., 225 (2010) 012007

[23] S. Mariazzi, P. Bettotti and R. S. Brusa, Phys. Rev. Lett., 104 (2010) 243401

[24] O. Sneh, M. A. Cameron and S. M. George, Surf. Sci., 364 (1996) 61

[25] D. Cassidy et al., J. Phys. B, 32 (1999) 1923

[26] E. Vliegen and F. Merkt, J. Phys. B 39 (2006) L241 ; E. Vliegen et al., Phys. Rev. A, 76 (2007) 023405

[27] M. K. Oberthaler et al., Phys. Rev. A, 54 (1996) 3165

[28] F. Castelli et al., Phys. Rev. A, 78 (2008) 052512

[29] "Physics with many positrons", R. S. Brusa, A. Dupasquier and A. P. Mills, Jr. eds. (IOS, Amsterdam 2010).

[30] S. Cialdi et al., Nucl. Instr. Methods Phys. Res. B, 269 (2011) 1527

[31] S. Mariazzi, A. Salemi, and R. S. Brusa, Phys. Rev. B, 78 (2008) 085428; S. Mariazzi, P. Bettotti and R.Brusa, Phys. Rev. Lett., 104 (2010) 243401; S. Mariazzi, P. Bettotti, S. Larcheri, L. Toniutti and R. S. Brusa, Phys. Rev. B, 81 (2010) 235418

[32] F. Castelli and M. G. Giammarchi, in "Physics with many positrons", R. S. Brusa, A. Dupasquier and A. P. Mills, Jr. eds. (IOS, Amsterdam 2010).

[33] R. W. Boyd, Nonlinear Optics, 3^{rd} ed., Academic Press, (2008)

[34] A. Yariv and P. Yeh, Optical waves in crystals, John Wiley and Sons; K. K. Sharma, Optics, Principles and Applications, Academic Press, (2006)

[35] M. M. Fejer, G. A. Magel, D. H. Jundt and R. L. Byer, IEEE J. Quantum Elect., 28 (1992) 2631

[36] A. V. Smith, http://www.as-photonics.com/snlo

[37] T. F. Jhonston Jr., App. Opt., 37 (1998) 4840

[38] O. Svelto, Principles of Lasers, Springer, Fourth edition (1998)

[39] C. H. Storry et al., Phys. Rev. Lett., 93 (2004) 263401

[40] A. Borsutzky, R. Brunger and R. Wallenstein, Appl. Phys. B, 52 (1991) 380

[41] M. Becucci et al., J. Mol. Struct., 993 (2011) 495

[42] E. R. I. Abraham and E. A. Cornell, App. Opt., 37 (1998) 1762

[43] J. Feng et al., Polymer Comm., 41 (2000) 2695

[44] S. G. Karshenboim, Phys. Rep., vol. 422 (2005) 1

[45] J. Ackermann et al., Phys. Rev. Lett., 78 (1997) 199

[46] D. Dermer and J. C. Weisheit, Phys. Rev. A, 40 (1989) 5526

[47] K. P. Ziock et al., Phys. Rev. Lett., 64 (1990) 2366

[48] D. B. Cassidy et al., J. Phys.: Conf. Ser., 194 (2009) 012037

[49] S.M. Curry, Phys. Rev. A, 7 (1973) 447

[50] A. Pineda and J. Soto, Phys. Rev. D, 59 (1998) 016005

[51] L.D. Landau and E. M. Lifsits, "Quantum Mechanics Non-relativistic Theory"

[52] A. Rich, Rev. Mod. Phys., 53 (1981) 127

[53] A. P. Mills et al., Phys. Rev. Lett., 34 (1975) 1541; S. Chu, A. P. Mills and J. L. Hall, Phys. Rev. Lett., 52 (1984) 1689; K. P. Ziock et al., J. Phys. B, 23 (1990) 329

[54] G. Feinberg, A. Rich and J. Sucher, Phys. Rev. A, 41 (1990) 3478; H. Garstang, Rep. Prog. Phys., 40 (1977) 8

[55] W. E. Lamb, Phys. Rev., 85 (1952) 259; M. L. Lewis and V. W. Huges, Phys. Rev. A, 8 (1973) 625

[56] M. Enciso-Aguilar et al., El. J. Theor. Phys.,3 (2006) 117

[57] T. F. Gallager, "Rydberg Atoms", Cambridge University Press (2005)

[58] K. Blushs and M. Auzinsh, Phys. Rev. A, 69 (2004) 063806

[59] J. H. Eberly, Phys. Rev. Lett., 37 (1976) 1387 ; A. T. Georges and P. Lambropoulos, Phys. Rev. A, 20 (1979) 991

[60] W. Gordon, Ann. Phys., 394 (1929) 1031 ; L. C. Green, P. P. Rush, and C. D. Chandler, Astrophys. J., Suppl., 3 (1957) 37

[61] M. Charlton and J. W. Humberston, "Positron Physics", Cambridge University Press (2001)

[62] K. P. Ziock et al., J. Phys. B: At. Mol. Opt. Phys., 23 (1990) 329

[63] T. J. Phillip, Hyperfine Interact., 100 (1996) 163

[64] A. P. Mills Jr. et al., Mater. Sci. Forum, 445-446 (2004) 424

[65] S. Chu et al., Phys. Rev. Lett., 55 (1985) 48

[66] T. Kumita et al. , Nucl. Instr. Meth. Phys. Res. B, 192 (2002) 171

[67] A. P. Mills, Jr. in "Physics with many positrons", R. S. Brusa, A. Dupasquier and A. P. Mills, Jr. eds. (IOS, Amsterdam 2010).

[68] D. B. Cassidy et al., Phys. Rev. Lett., 106 (2011) 173401